Aus dem Institut für Strahlenmedizin des Helmholtz-Zentrums München

Vorstand: Prof. Dr. Stephanie E. Combs

Secondary neutrons at laser-driven ion sources

Dissertation
zum Erwerb des Doktorgrades der Naturwissenschaften
an der Medizinischen Fakultät der
Ludwig-Maximilians-Universität zu München

vorgelegt von

Marco Tisi

aus

Calcinate (BG), Italien

Jahr

2022

Mit Genehmigung der Medizinischen Fakultät

der Universität München

Betreuer:	Prof. Dr. Werner Rühm
Zweitgutachterin:	Prof. Dr. Paola Coan
Dekan:	Prof. Dr. med. Thomas Gudermann
Tag der mündlichen Prüfung:	25. April 2023

Table of Content

Zusammenfassung

Lasergestützte Ionenquellen nutzen die Wechselwirkung eines hochintensiven Laserpulses mit Materie, um Ionen auf mehrere Dutzend MeV zu beschleunigen, und zwar innerhalb weniger Mikrometer und innerhalb Zeiten im Femto- bis Nanosekundenbereich. Diese Art der Beschleunigung hat, vor allem wegen ihrer räumlichen Kompaktheit, das Potenzial, herkömmliche Teilchenbeschleuniger zu ersetzen und in Zukunft ein breites Spektrum von neuen Anwendungen zu eröffnen, einschließlich Anwendungen im medizinischen Bereich (z. B. bei der Krebstherapie mit Hadronen). Aufgrund der Physik der Laser-Target-Wechselwirkung sind lasergestützte Ionenquellen derzeit durch große Emissionswinkel gekennzeichnet. Infolgedessen geht ein großer Teil der beschleunigten Teilchen entweder an den Wänden der verwendeten Vakuumkammer oder an den Strahlführungselementen verloren, was zur Erzeugung unerwünschter Sekundärstrahlung (hauptsächlich bestehend aus Photonen und Neutronen) führt. Dies ist vor allem dann von Bedeutung, wenn es um den Einsatz von lasergestützten Beschleunigern in der Krebstherapie geht.

Im Rahmen dieser Doktorarbeit wurde mit Hilfe von Geant4-Monte-Carlo-Simulationen und Messungen die Produktion von Sekundärneutronen in der Nähe von lasergestützten Ionenquellen untersucht. Zunächst wurde eine systematische Geant4-Monte-Carlo-Studie der zu erwartenden Neutronenfelder an der lasergestützten Ionenquelle LION (Centre for Advanced Laser Applications - CALA, Garching bei München) durchgeführt. Dazu wurden aus der Literatur entnommene primäre Protonenspektren mit unterschiedlichen Cutoff-Energien (~12, ~56, ~86 MeV), die für drei verschiedene Inbetriebnahme-Schritte von LION repräsentativ sind, zur Simulation von Neutronenenergiespektren und Neutronendosen in der Nähe der LION-Vakuumkammer verwendet. Die Simulationen ergaben gemischte, gepulste Neutronen- und Photonenfelder mit einer maximalen Neutronendosis pro Puls in der Größenordnung von mehreren hundert µSv/Puls in der Nähe der Vakuumkammer, wenn die intensivste primäre Protonenquelle verwendet wurde.

Auf der Grundlage der Ergebnisse dieser Monte-Carlo-Simulationen wurde die Durchführbarkeit von Messungen an LION mit verschiedenen Neutronendetektoren (aktiven und passiven REM-Counter, die speziell zum Nachweis von Neutronen mit hohen Energien geeignet sind; einem tragbaren LUPIN-II-Zähler, der für gepulste Neutronenfelder entwickelt wurde; und einem Bonner-Kugelspektrometer auf Goldfolienbasis) für jedes betrachtete Bestrahlungsszenario überprüft. Dabei zeigte sich, dass bei lasergestützten Protonenquellen geringer Intensität die gepulste Natur der

Quelle die Durchführung von Messungen mit konventionellen REM-Counter nicht behindert (vorausgesetzt, es steht eine geeignete Anzahl von Pulsen zur Verfügung). Im Gegensatz dazu stellte sich heraus, dass für Protonenquellen mittlerer und hoher Intensität derzeit nur passive Techniken und Detektoren, die für gepulste Neutronenfelder entwickelt wurden (wie der LUPIN-II-Zähler), geeignet sind. Die Machbarkeitsstudie zeigte auch, dass Messungen an LION mit den untersuchten Neutronendetektoren nicht möglich waren, da sich LION zum Zeitpunkt dieser Arbeit noch in einem relativ frühen Stadium der Inbetriebnahme befand.

Daher wurden im Rahmen dieser Doktorarbeit Experimente an der lasergestützten Ionenquelle DRACO (Dresden Laser Acceleration Source, Helmholtz-Zentrum Dresden-Rossendorf) in Dresden durchgeführt, wo an zwei Bestrahlungstagen mehr als dreihundert Laserpulse bei Protonen-Cutoff-Energien von bis zu 60 MeV zur Verfügung standen. Online-Einzelpulsmessungen der Dosis sekundärer Neutronen wurden erfolgreich mit dem LUPIN-II-Zähler durchgeführt, wobei sich Neutronendosen pro Puls von bis zu 300 nSv/Puls in einem Abstand von etwa zwei Metern vom Laser-Target ergaben. Die LUPIN-II-Ergebnisse wurden mit den Messwerten eines CR39-basierten REM-Counters, dem „Passive LINUS“, verglichen, indem die Gesamtzahl der Laserpulse für jeden Messtag integriert wurde, und es wurde eine zufriedenstellende Übereinstimmung festgestellt: Die LUPIN-II-Messungen ergaben am ersten bzw. zweiten Tag kumulierte Neutronendosen von 9,2 µSv (± 17 %) bzw. 11,8 µSv (± 17 %), während die Messungen mit dem „Passive LINUS“ am ersten bzw. zweiten Tag 4,8 µSv (± 62 %) bzw. 9,7 µSv (± 21 %) ergaben. Obwohl die letztgenannten Messungen aufgrund der niedrigen kumulierten Neutronendosis mit relativ großen Unsicherheiten behaftet waren, bestätigten sie, dass die LUPIN-II-Messwerte frei von Photonenkontaminationen und elektromagnetischen Störungen waren, die für die Umgebung von lasergestützten Ionenquellen typisch sind. Die Ergebnisse der Messkampagne bei DRACO wurden schließlich mit Geant4 Monte-Carlo-Simulationen verglichen, die eine zufriedenstellende Übereinstimmung mit den experimentellen Ergebnissen zeigten.

Diese Arbeit zeigt vor allem, dass der LUPIN-II-Detektor geeignet ist, Messungen der Neutronen-Umgebungsdosis in den für lasergestützten Ionenquellen typischen und messtechnisch herausfordernden Strahlenfeldern durchzuführen. Dieser Detektor könnte daher für zukünftige Forschungen auf dem Gebiet der Sekundärstrahlung, die an lasergestützten Ionenbeschleunigern erzeugt wird, eingesetzt werden, wobei der Schwerpunkt in dieser Arbeit auf der Abschätzung der Neutronendosis bei

Bestrahlungen mit klinisch ähnlichen Strahlbedingungen lag (die derzeit an lasergestützten Ionenquellen noch nicht verfügbar sind).

Darüber hinaus deuten die erzielten Ergebnisse darauf hin, dass die Messung der Neutronendosis für einzelne Pulse als ergänzendes Instrument für Online-Schätzungen der Anzahl der pro Puls erzeugten Ionen eingesetzt werden könnten.

Abstract

Laser-driven ion sources exploit the interaction of a high intensity laser pulse with a target material to accelerate ions up to several dozens of MeV, within micrometer distances and times in the femto- to nano-second range. This acceleration technique, mainly owing to its compactness, has the potential for replacing conventional particle accelerators and for becoming the future modality of particle acceleration for a vast range of uses including applications in the medical field (such as cancer therapy with hadrons). Due to the physics of the laser-target interaction, these particle sources are currently characterized by wide emission angles. Consequently, a large fraction of accelerated particles is either lost on the vacuum chamber walls or on the beamline elements, resulting in the production of unwanted secondary radiation (mainly composed by photons and neutrons). This is a relevant issue especially when considering the use of laser-driven accelerators in cancer therapy.

The present study investigates, by means of Geant4 Monte Carlo simulations and measurements, the production of secondary neutrons in the proximity of laser-driven ion sources. A systematic Geant4 Monte Carlo study of the expected neutron fields at the laser-driven ion source LION (Centre for Advanced Laser Applications – CALA, Garching near Munich, Germany) is initially presented. For this work, primary proton spectra taken from the literature, with different cutoff energies (~12, ~56, ~86 MeV) and representative of three different commissioning steps of LION, are used to simulate neutron energy spectra and neutron doses in specific volumes located in the proximity of the LION vacuum chamber. The simulated radiation environment is characterized by mixed (neutron and photon) pulsed fields, with maximum neutron dose per bunch in the order of hundreds of μSv/bunch close to the vacuum chamber, when using the most intense primary proton source.

Based on the results of these Monte Carlo simulations, the feasibility of using different neutron detectors (such as conventional active and passive extended-range REM counters, the LUPIN-II, and a gold-foil-based Bonner Sphere Spectrometer) to perform measurements at LION was then verified for each considered irradiation scenario. This showed that for low-intensity sources the pulsed nature of the source should not prevent from doing measurements with conventional REM counters (provided that a suitable number of bunches is available). In contrast, for intermediate- and high-intensity proton sources it turned out that only passive techniques and detectors developed for pulsed neutron fields (such as the LUPIN-II) are currently suitable.

The feasibility study also demonstrated that measurements at LION with the selected neutron detectors are not promising, given the rather early stage of LION's commissioning at the time of this thesis.

Experiments were therefore conducted at the DRACO laser-driven ion source (Helmholtz Zentrum Dresden-Rossendorf) located in Dresden, Germany, where more than three-hundred laser shots and proton cutoff energies up to 60 MeV were available, over two irradiation days. Online single-bunch measurements of the secondary neutron dose were successfully performed by the LUPIN-II (a portable neutron REM counter developed for pulsed neutron fields) that measured neutron doses per bunch up to about 300 nSv/bunch at a distance of about two meters from the laser-target. The LUPIN-II results were compared with the readings of a CR39-based REM counter, the Passive LINUS, by integrating over the total number of laser shots, for each measurement day, and reasonable agreement was found. Cumulated neutron doses of 9.2 μSv (± 17%) and 11.8 μSv (± 17%) were measured by the LUPIN-II on the first and second day respectively, while the Passive LINUS measured 4.8 μSv (± 62%) and 9.7 μSv (± 21%) on the first and second day, respectively. Although this measurement was affected by large uncertainties due to the low cumulated neutron dose, it confirmed that the LUPIN-II readings were free from photon contamination and electromagnetic disturbance, typical of the environment at laser-driven sources. The experimental campaign at DRACO was also benchmarked with Geant4 Monte Carlo simulations that showed a satisfactory agreement with the experimental results.

This thesis mainly shows that the LUPIN-II detector is suitable to perform single-bunch measurements of the neutron ambient dose in the challenging environment typical of laser-driven ion sources. This detector could, therefore, be used for future research in the field of the secondary radiation produced at laser-driven ion accelerators, with focus on estimating the neutron dose during irradiations with clinical-like beam conditions (currently not available at laser-driven ion sources). In addition, experimental studies on the relationship between neutron dose per bunch and total number of accelerated ions per bunch could also be performed by using the LUPIN-II, in order to assess the feasibility of employing single-bunch neutron dose measurements as complementary tool for online estimates of the number of ions produced per bunch.

List of Figures

List of Tables

Abbreviations

BSS, Bonner Sphere Spectrometer

DRACO, Dresden laser acceleration source

ERBSS, Extended Range Bonner Sphere Spectrometer

ETTF, Electron Thomson Test Facility

H*(10), Ambient Dose Equivalent

HMGU, Helmholtz-Zentrum München Deutsches Forschungszentrum für Gesundheit und Umwelt

IRM, Institute of Radiation Medicine

LION, Laser-driven ION source

LMU, Ludwig-Maximilians-Universität München

MDA, Minimum Detectable Activity

MED, Medical and Environmental Dosimetry

PNF, Pulsed Neutron Fields

PSI, Paul Scherrer Institute

QP, Quadrupole magnet

TPS, Thomson Parabola Spectrometer

1. Introduction

In the last two decades, the large improvements in laser peak power, laser temporal contrast and energy density, together with an extensive research of suitable target shapes and materials, enabled the possibility to accelerate protons and light ions up to several tens of MeV [1], by exploiting the direct interaction between a high-power laser pulse and the target material.

Even though laser-driven acceleration of charged particles is still in an early phase of its development, it is however gradually becoming a valuable candidate for future ion acceleration techniques [2]. Thanks to the small dimensions at which the acceleration process takes place (in the sub-millimeter range), laser-driven ion sources are suited for novel investigations in research and have great potential for pushing the frontiers for future generations of particle accelerators for a broad range of applications [3].

Radiation therapy with charged particles, for instance, would greatly benefit from compact laser-driven based accelerators, both from a practical point of view (hospitals would not require the installation of a massive cyclotron in dedicated rooms) and from an economical point of view. Once a fully grown laser-driven acceleration technology will be available, it is reasonable to assume that, with drastically smaller accelerator sizes, also lower costs will come, and this would help spreading the technology of tumor treatment through charged particles, nowadays still hampered by the high costs connected to the installation of cyclotrons or, even worse, synchrotrons [4,5].

As stated by *Daido, Nishiuchi and Pirozhkov* in an extensive review on the state the art of laser-driven ion sources and their applications [6], hadrontherapy with laser-driven beams remains a challenging application. This is true mainly because crucial improvements in maximum particle energy, as well as beam quality, still need to be made before this acceleration technique could be applied for actual tumor treatments [6]. As an example, in proton therapy, protons with energy up to 250 MeV are required to reach deep-seated tumors. At the moment, the maximum energy of protons accelerated by using laser-target interaction reported in the literature is still below 100 MeV [7]. Conventional cyclotrons used for proton therapy deliver protons with well-defined charge per bunch and arbitrary small spot size (down to millimeter precision in pencil beam scanning facilities). Such beam quality can hardly be matched at the moment by laser-driven facilities, where the emitted protons show a high divergence (up to tens of degrees) and bunch-to-bunch charge instability [8]. In addition to this, due to the large laser systems needed

to reach TW and PW power, a translation from research-oriented laser-driven accelerator facilities to hospital-based compact dedicated accelerators is still pending.

Although medical applications are still not feasible, several *in vitro* radiobiological experiments performed by using laser-driven proton accelerators already appeared in the literature. In a comparison between laser-driven protons and conventionally accelerated protons in an *in vitro* experiment, *Zeil et al.* showed that laser-driven accelerators can already offer the required performance level for radiobiological studies [9]. In other studies, *Yogo et al.* and *Doria et al.* measured the relative biological effectiveness (RBE[1]) of laser-driven protons, finding values in the range of 1.2 – 1.4, close to the RBE of protons conventionally accelerated for clinical applications [10,11]. *In vivo* experiments using laser-driven proton accelerators have not been performed yet, this is mainly due to the too low proton energies achievable, that hinder the possibility of irradiating 3D tumors. Recently, *Rösch et al.* published an *in vivo* feasibility study on zebra fish [12] and *Brack et al.* experimentally demonstrated the possibility of irradiating a mouse tumor model, which requires a homogeneous dose distribution with ±5% deviation over a cylindrical volume of 5 mm in diameter and length [13]. A review of the state of the art of laser-driven radiobiological experiments was recently published by *Chaudhary et al.* [14]. The success in the application of laser-driven proton sources to radiobiological experiments shows that, albeit challenging, the way towards medical applications of laser-driven particle accelerators has already been paved.

In view of the further development of laser-driven particle sources towards their application in the medical field, a clear assessment of the secondary particle production must be carried out too. Especially because, given its relatively small size, the particle accelerator could be standing in close proximity to the patient, who then would be not only irradiated by the particles used for the treatment, but also by the shower of secondary particles (for instance neutrons, X-rays and gamma rays) that are produced in the beam guiding system used to deliver the particles for treatment. Among all secondary particles produced, neutrons deserve a special attention, mainly because of their high relative biological effectiveness [15], that make them particularly harmful. In addition to this, neutrons are also highly penetrating and therefore hard to shield, compared to other particles such as X- and soft γ-rays.

[1] RBE is defined as a ratio of the dose of the reference radiation to that of the radiation of interest needed to achieve the same biological result (e.g., cell death) [111].

Studies of the secondary neutron fields have been, and nowadays still are, conducted on *conventional* proton therapy facilities, in order to assess the secondary neutron dose to which patients are exposed to whenever they undertake a tumor treatment. Such studies proved that the overall dose due to secondary particles deposited a few tens of centimeters from the isocenter is in the order of 0.1 mSv per treatment Gy [16], a value that does not question the safety of modern proton therapy, nor raises concerns for the well-being of the patient. To monitor the neutron ambient dose, H*(10) (for details on the terminology of dosimetric quantities refer to Appendix A), inside the treatment room of such proton therapy facilities, routinely employed radiation protection neutron REM counters are being successfully used as documented by [17–20]. This is most likely not going to be feasible for laser-driven particle sources because, unlike conventional cyclotrons where the proton beam is composed by low-charge milliseconds-long bunches at a repetition frequency in the order of kHz, laser-driven particles are produced in bunches with a large charge per bunch, short temporal duration and at a low repetition frequency (from single shot operation to a maximum of 10 Hz). It is then obvious that the produced secondary radiation, instead of being composed by a low fluence per bunch with high repetition frequency (and therefore *almost* continuous) will come in very short and intense bunches, potentially able to saturate the response of active radiation detection devices, such as conventional REM counters. Dose underestimation of conventional neutron REM counters was already observed in the treatment room of a radiation therapy facility driven by a Mevion Hyperscan S250i synchro-cyclotron where treatment protons are delivered at only 750 Hz and at a bunch length of 10 μs [21].

As mentioned, a clear assessment of the secondary radiation produced by laser driven particle sources is then a mandatory step for radiation protection purposes, to be evaluated also in comparison with already available proton therapy technologies. In addition, given the development status of laser-driven particle sources, detection of secondary neutrons could in principle be also employed as a non-invasive complementary beam diagnostic tool to improve, together with other diagnostic techniques, the knowledge on the laser-driven particles produced.

The aim pursued in this work is therefore to evaluate the expected secondary neutron fields present in the proximity of laser-driven particle sources, by estimating the neutron dose per bunch together with discussing the currently available viable options for neutron detection in such challenging environments.

This work starts with a general introduction on laser-driven acceleration focusing on the most used scheme for ion acceleration, TNSA (Target Normal Sheath Acceleration), together with showing the current knowledge on secondary neutron production at laser-driven particle accelerator facilities (Chapter 2). In Chapter 3, neutron detection techniques, with special attention to the topic of neutron detection in pulsed neutron fields, is shown. Chapter 4 describes the general features of Geant4, the Monte Carlo simulation tool used to perform preliminary simulations and feasibility studies. Afterwards, in Chapter 5, the preparatory studies performed in the initial part of this thesis will be presented including initial test irradiations, Monte Carlo simulations, and a feasibility study for neutron detection at the laser-driven ion source, LION (Garching near Munich). After this, experimental results acquired at the DRACO laser-driven ion accelerator (Dresden) are presented and compared with the simulations (Chapter 6). Discussion, Conclusions and Outlook follow in Chapter 7 and Chapter 8, respectively.

2. Laser-driven acceleration

When talking about laser-driven acceleration one refers to a mechanism where a laser pulse delivers enough energy per unit time and surface to a target material, that it is capable of creating a plasma in which the electric fields established inside are strong enough to accelerate particles (namely, electrons and ions).

Since the invention of the first laser systems back in the 1960ies, laser scientists have overcome several challenges in trying to achieve, above all, increasing power densities. Many technical inventions, such as Q-switching [22] and mode locking [23] allowed laser technology to progress to the status it has today. One of the most important among these steps is perhaps the invention of the CPA (Chirped Pulse Amplification) by D. Strickland and G. Mourou in 1985 (which led them to winning the Nobel Prize in Physics in 2018 [24]). This technique is based on the fact that a very short pulse is composed of many wavelengths which can be spatially dispersed by using diffractive elements. If this low energetic short pulse is made go through a diffractive grating, different wavelengths will travel optical paths of different length resulting in a stretching of the pulse. Once the pulse has been stretched, its peak power is highly reduced, which allows large amplification without the risk of damage in the laser system. At this stage, the highly energetic and stretched pulse is made go through another diffractive grating that acts in the opposite way and recompresses the pulse right before being focused onto the target.

Thanks to the abovementioned technical discoveries, nowadays lasers can produce laser pulses of dozens-hundreds of J, with pulse duration that range from picoseconds to femtoseconds, delivering a peak power of the order of TW to PW, at a repetition frequency up to the Hz range. When such power is focused onto a target material whose size is in the micrometer range, intensities up to 10^{20}-10^{22} W/cm^2 can be reached, inducing the production of plasma and, consequently, particle acceleration.

2.1 Ion acceleration

For laser intensities higher than 10^{18} W/cm^2, the most used and well-known acceleration modality currently employed to accelerate ions by laser-target interaction is the so-called TNSA (Target Normal Sheath Acceleration) [25,26]. According to this mechanism, when the rising edge of the incoming laser pulse impinges on the target material (which is commonly a solid material of nm to μm thickness), it locally ionizes the target creating a plasma. Since the laser energy transfer is more efficient with electrons than with ions, most of the laser energy is absorbed by a cloud of electrons that is pushed from the front

to the rear face of the target (Figure 1a). The electrons gain enough energy so that their mean free path is larger than the usual thickness of the target and, hence, this enables them to leave the target material in the direction normal to its rear surface [11,27]. By doing so, they leave behind the positively-charged ions of the target that, at these time scales, can be considered as motionless, and a large electric field sets in between the leaving negative electrons and the standing positive ions (Figure 1b). The magnitude of the electric field, in the order of MV/μm (compared to conventional RF accelerators where the field intensity is of the order of MV/m) [6], is able to strip the ions off the rear surface of the target and accelerate them up to several dozens of MeV over sub-millimeter distances. Protons, compared to other ions, gain the highest kinetic energies due to their higher charge-to-mass ratio. Given that this process mainly involves the (rear) surface of the target, the particles that will be mostly accelerated are those constituting the surface contaminants, such as water, always present even in vacuum conditions.

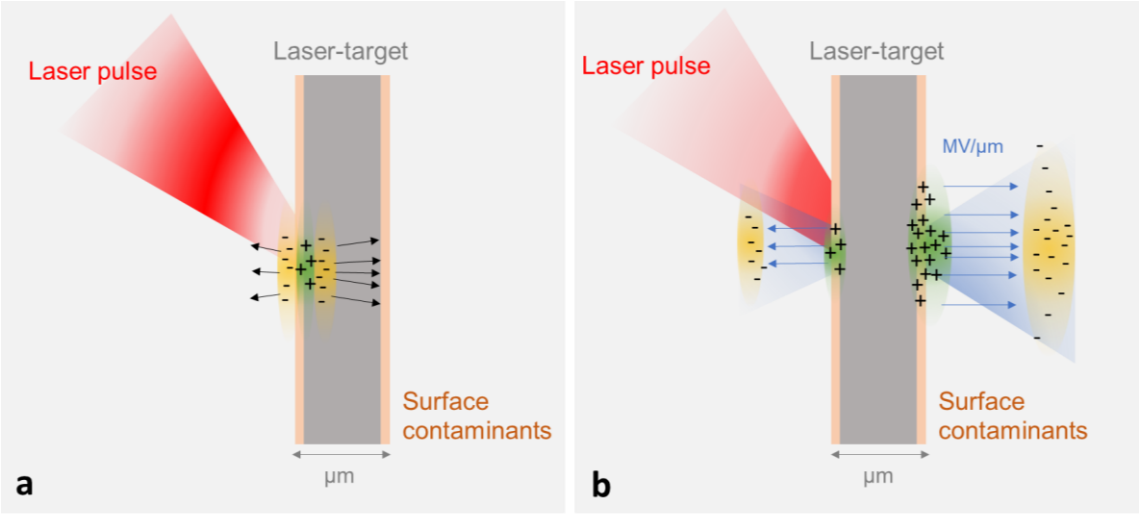

Figure 1: Schematic representation of Target Normal Sheath Acceleration (TNSA) mechanism. **a**) A laser pulse front impinges on the front surface of the target and produces a plasma. Electrons are driven towards the target rear surface ionizing the contaminants of the rear surface. **b**) Electrons leave the rear surface, and an electric field builds up accelerating the positively-charged ions of the rear surface.

It is evident from this simple description that not only one desired species of particles is produced, but protons, heavier ions and electrons are simultaneously accelerated. In addition to this, because the acceleration is driven by the expanding cloud of electrons leaving the rear surface of the target, the divergence of such a proton source is rather high (half angles of tens of degrees) [6]. The typical spectrum of protons accelerated through TNSA goes from 0 MeV to a so-called cut-off energy in the range of tens of MeV

(cut-off energies of up to almost 100 MeV were reported in [7,28]) decreasing exponentially in intensity with increasing energy. Figure 2, taken from the webpage of the Ludwig-Maximilians-Universität München (LMU) dedicated to the applications of laser driven particle acceleration [29], reports several proton spectra experimentally measured and published over the last 20 years. As visible, the vast majority of spectra display the above-mentioned exponential behavior. The cutoff energy of protons is a parameter often used to quantify the performance of a laser-driven acceleration system, and higher cutoff energies are expected when higher laser intensity is delivered on target, although several other parameters, such as target thickness, pre-pulse energy and pre-pulse duration, play a role in the determination of the maximum achievable proton energy [30].

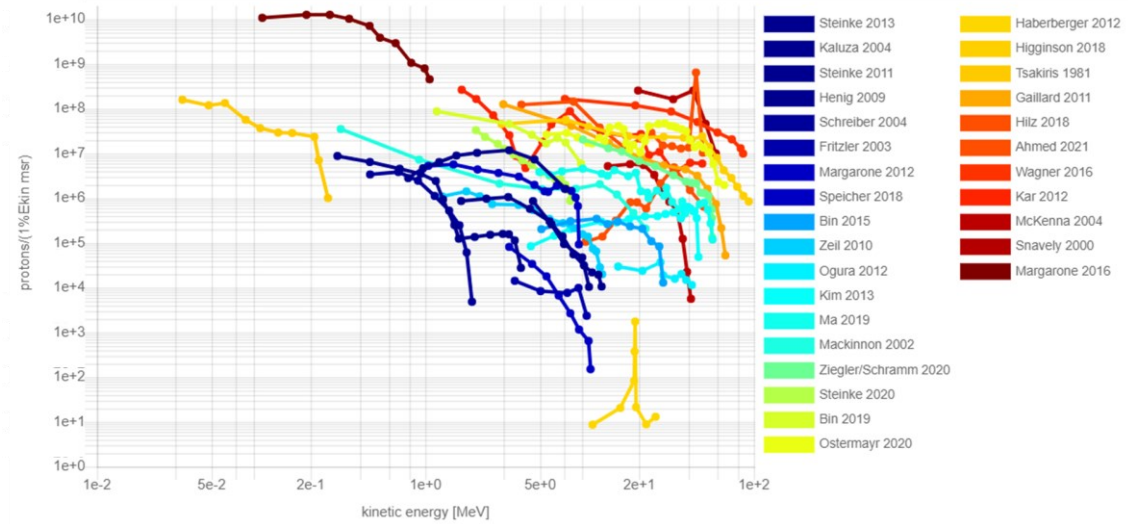

Figure 2: Experimental proton spectra published in the literature and simultaneously plotted in terms of $protons/1\%E_{kin}/msr$. Figure taken from [29].

Thanks to the availability of ultrahigh power lasers with intensities up to 10^{22} W/cm^2, laser-driven ion research is trying to optimize ion acceleration inducing different acceleration mechanisms beyond TNSA, in order to reach higher proton energies. One of these, the so-called RPA (Radiation Pressure Acceleration), by exploiting radiation pressure on electrons, foresees the production of protons with less energy spread together with higher proton energies [31]. Other mechanisms are being also investigated such as, Coulomb Explosion, Shock Wave Acceleration, Relativistic Transparency or Break-Out-Afterburner (BOA) [32].

2.2 Secondary neutrons at laser-driven ion facilities

From a practical point of view, a laser-driven ion source (or accelerator) usually consists of an interaction chamber (kept under vacuum conditions) where the laser pulse is focused onto a target material (often at solid state) and where laser-target interaction takes place. Inside the vacuum chamber, together with the target, its target holder and the mirrors needed to focus the laser pulse, several laser and proton diagnostic tools, focusing magnets and cameras (with the respective supporting structures) are hosted. Figure 3 shows the inside of the vacuum chamber of the DRACO laser-driven proton source and gives an idea of the amount of equipment that is usually installed in the vacuum chamber. It has to be mentioned that the placement of part of these components not only varies from accelerator to accelerator (commercial standardized laser-driven ion sources still do not exist) but also according to the specific needs of a given experiment.

Due to the large divergence at which laser-driven ions are emitted, it is reasonable to expect that an important fraction of the emitted particles, instead of being focused and transported through the beamline, interacts with the surrounding components, even with the vacuum chamber itself. For proton energies higher than a few MeV, the cross section for neutron production of most elements becomes non-negligible, and production of secondary neutron radiation becomes therefore probable. As an example, if one takes aluminum (one of the elements most widely used for the construction of vacuum chamber walls), already at proton energies of about 6 MeV a reaction channel leading to neutron production opens (^{27}Al(p,n)^{27}Si). Secondary neutron radiation will be produced in bunches of the same repetition frequency of the source and with very short bunch length, details on this follow in Chapter 3.1. In addition, considering that also electrons are accelerated via TNSA, it is reasonable to expect that, together with the pulsed neutron field (PNF) mainly generated by protons, also gamma and bremsstrahlung photons will be present giving rise to a mixed pulsed neutron and photon field.

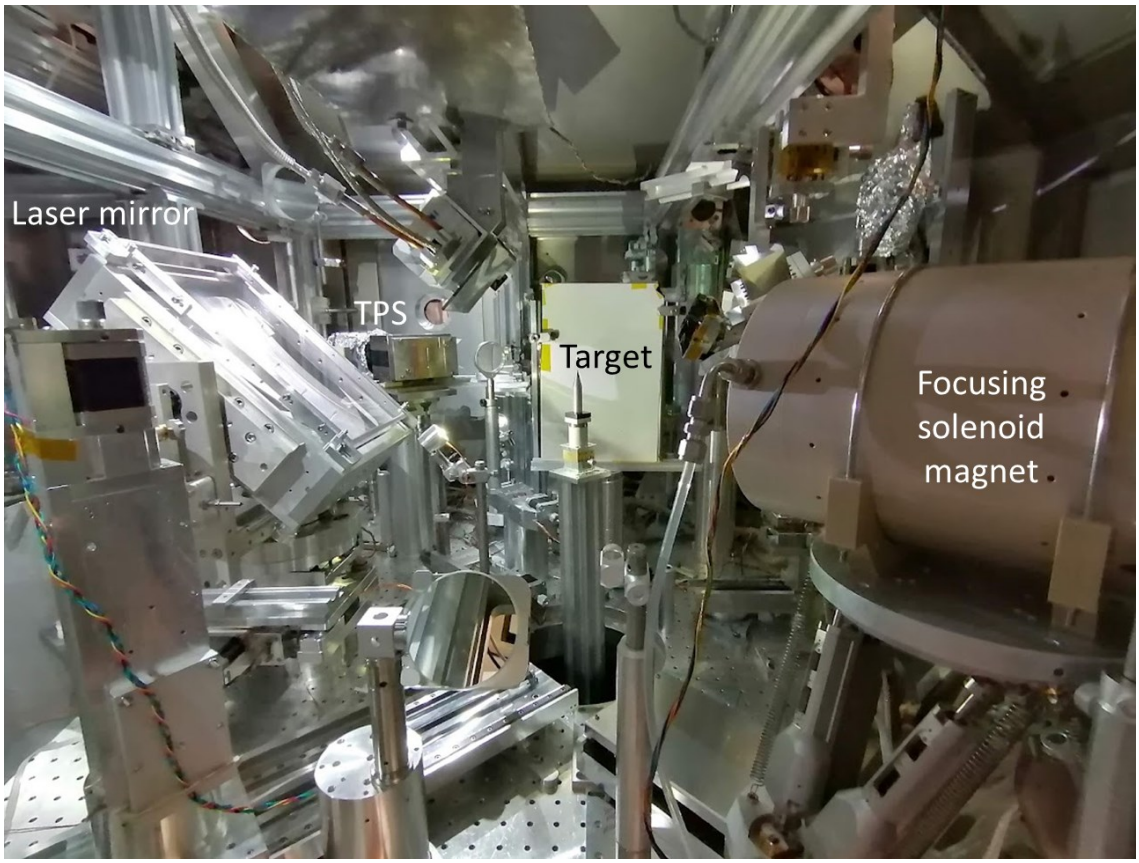

Figure 3: Inside of the DRACO vacuum chamber, Dresden, Helmholtz-Zentrum Dresden-Rossendorf. Clearly recognizable are the target holder, a laser mirror, the TPS (Thomson Parabola Spectrometer) for backward-emitted ions and a solenoid magnet.

Radiation protection-oriented studies on the production of secondary radiation in the proximity of laser-driven particle sources published so far are rather inhomogeneous, with results hardly transferable to other facilities. This is mainly due to the differences in design of the accelerators and laser parameters used (i.e., laser peak power, laser energy on target, and laser intensity), and due to the fact that usually only partial information on the produced laser-driven particles (such as charge per bunch, cutoff energy, energy spectrum, divergence) is simultaneously provided. Nevertheless, these works reveal a general trend: the higher the intensity of the laser the higher the production of secondary radiation, as underlined by a review report published by the University of Lund in 2019 [33].

So far, most of the studies described in the literature on the topic of secondary radiation production (i.e., gamma rays and neutrons) in the proximity of laser-driven particle sources include radiation environments at laser-driven *electron* accelerators rather than

those at laser-driven *ion* sources and, in general, one can find more computational studies using different Monte Carlo codes (such as, FLUKA, MCNPX, Geant4, or PHITS), rather than experimental studies.

Computational works range from studies dealing with the secondary radiation expected at experimental facilities currently in operation [34,35] to studies dealing with the shielding dimensioning for future laser-driven particle accelerators, as is the case of the bulk shielding calculations showed by *Olšovcová et al*. [36]. As an example, in 2017 *Florescu et al.* [37] published a FLUKA Monte Carlo study of the expected secondary radiation due to electrons and protons at the CETAL-PW laser-particle accelerator (Bucharest, Romania). In the experimental cave close to the vacuum chamber, total (photon and neutron) doses in the order of mSv/bunch were calculated when using protons as primary particles. Even though it must be mentioned that the source term used was rather intense including mono-energetic 100 MeV protons with 10^{14} primaries/bunch, this shows that the expected radiation environment inside the experimental cave is characterized by pulsed secondary radiation.

Computational studies more oriented towards medical applications also appeared in the literature. An example is the publication of *Fan et al.* [38] (2007) where the feasibility of using laser-driven protons to perform tumor treatment was investigated by designing a compact energy selection system. *Fan et al.* mainly focused on the design of a shielding structure required for a 300 MeV cutoff energy proton source to be used as beam delivery for a proton therapy facility. The authors underlined the challenges posed by the presence of highly penetrating neutron radiation and concluded that at least 10-12 cm of polyethylene plus 4 cm of lead are required to effectively shield both neutron and gamma radiation and reach the radiation levels required for medical applications. In contrast, in 2014, *Faby and Wilkens* [39], extending the work of *Fan et al.*, calculated the dose due to secondary radiation delivered to a hypothetical patient undergoing tumor treatment, by using a more realistic source that also includes the angular distribution of the primary particles. *Faby and Wilkens* found out that a higher number of primary particles was needed to deliver the same dose to the tumor if a more realistic source term was used. Therefore, the authors concluded that, for the current conditions, the stray radiation coming from the energy selection system *"would pose a serious secondary dose contamination to the patient"* [39], and for applications in tumor therapy of laser-driven proton accelerators, a better source quality would be required.

Regarding experimental activities, only a few studies, mainly performed by using passive detectors (such as thermoluminescence dosimeters (TLDs) for photons or bubble detectors for neutrons) appeared in literature so far [34,40]. One of these studies, most relevant for the present thesis because it was performed on a laser-driven *proton* source, was published by *Sakaki et al.* in 2010 [34]. These authors described a combined PHITS Monte Carlo simulation and experimental study of the secondary doses produced at KPSI's (Kansai Photon Science Institute's) laser-driven proton source (laser energy ~1.8 J and peak intensity ~10^{19} W/cm^2 at 1 Hz repetition frequency). The experiments were carried out with proton cutoff energies of about 7 MeV (although the authors underline a 20-30% shot-to-shot variation in the total number of particles per bunch). Given the pulsed nature of the source, the authors employed passive glass dosimeters and measured total doses (with no distinction between photons and neutrons) in the order of a few μSv/bunch on the external surface of the facility's vacuum chamber (~50 cm from the source). Rather good agreement with Monte Carlo simulations was also observed, in which, together with protons, also electrons and X-ray source terms have been considered.

To identify active neutron detection techniques applied to measurements of secondary radiation fields at laser-driven particle sources one needs to look at the work of *Liang et al.* published in 2016 [41], which summarizes the experiments conducted over a few years at SLAC National Accelerator Laboratory's Matter in Extreme Conditions (MEC). Here, a 25 TW laser system delivering 1 J energy laser pulses at 1 Hz was used to conduct laser-driven *electron* acceleration experiments. Although the focus of the work was on photon dose measurements with passive and active devices, also an active neutron REM-counter type instrument was used. No neutron dose underestimation was reported, probably due to the low intensity of the source, yielding to maximum electron energy of about 2.5 MeV. Neutron dose rates of about 30-40 nSv/h were measured at 1 Hz repetition frequency, resulting in a dose per bunch of about 0.01 nSv/bunch, a value that is well within the working regime of any neutron REM counter.

Literature describing experimental studies that show the application of active neutron detection techniques to measure the stray radiation produced at laser-driven ion sources is scarce. Special mention need, anyway, the several dedicated studies on laser-driven *neutron* sources that were carried out in the last two decades. A large fraction of these experiments makes use of a laser-driven ion (proton and deuteron) source coupled with a specific converter material (such as Be and Li). In these experiments, the neutron output was maximized with the so-called pitcher-catcher geometry [42], with the final goal

to create compact laser-driven neutron sources. These laboratories usually allow to perform neutron time of flight measurements (nTOF) with fast scintillators [43], a technique that often requires several meters of dedicated space free from obstacles to perform an efficient discrimination of the different neutron energies. Such space is hardly available for laser-driven proton facilities where the main goal is the production, transport and delivery of accelerated protons, and where neutrons constitute an unwanted secondary radiation rather than the scientific goal of the experiment. Other detectors commonly employed are passive detectors (such as, bubble detectors [44] and track-etched detectors [45] or activation detectors [46]). Studies on laser-driven neutron sources often report their results as total neutron yield (neutrons/bunch or neutron/proton), which is not a quantity directly usable for radiation protection applications. So far, maximum neutron yields reported in the literature at laser-driven ion (proton and deuteron) sources are of the order of 10^{10} n/bunch [47,48]. Therefore, although designed for the highest neutron output and not intended for radiation protection purposes, studies on laser-driven neutron sources could be considered as an extreme case of secondary neutron production at laser-driven ion sources, giving insight into the maximum achievable neutron yield per bunch, in a sort of worst-case scenario.

3. Detection of Pulsed Neutron Fields

3.1 Definition of Pulsed Neutron Field (PNF)

The most peculiar feature of the secondary radiation fields expected at laser-driven proton sources is their pulsed temporal profile. In a very broad and general sense, a pulsed neutron field (but more generally *any* pulsed radiation field) could be defined as a field whose intensity is characterized by sudden changes in magnitude over time, in contrast to a steady field that could be defined as a field whose intensity, although free to change over time, is not characterized by sudden variations. In a very schematic way, a pulsed neutron field can be viewed as a repetition of pulses of rectangular shape characterized by:

- Bunch[2] duration, T_{bunch}.
- Repetition frequency of the pulsed source, f. The period of the source, i.e., the temporal distance from one bunch to the other, can be calculated as $T = f^{-1}$.
- Dose per bunch, D_{bunch}.
- Dose rate in the bunch, DR_{bunch}, calculated as the average dose rate in the bunch $DR_{bunch} = D_{bunch}/T_{bunch}$.
- Mean dose rate, DR_{avg}, calculated as the average of the dose over one period $DR_{avg} = D_{bunch}/T$.

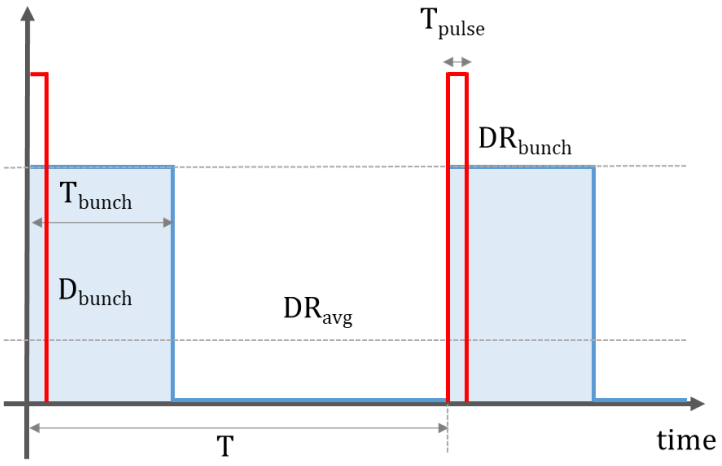

Figure 4: Schematic representation of a pulsed radiation field.

[2] *Bunch* is used instead of *pulse* to avoid any misunderstandings: the term *pulse* is referred to the laser while *bunch*, is referred to primary and secondary particles.

At laser-driven ion sources, although the laser-pulse duration, T_{pulse}, is of the order of tens of fs, the duration of the bunch of secondary particles is orders of magnitude larger. As described, secondary neutrons are mostly emitted by the interaction of primary particles with surrounding materials. Primary particles are emitted with large energy spread, from 0 MeV to dozens of MeV. If one assumes that the first interaction object is a component hosted inside the vacuum chamber (as could be a focusing magnet or a diagnostic instrument, see Figure 3) at about 10 cm distance from the primary particle source, the time required for a 1 MeV proton to reach it is ~7 ns, while for a 50 MeV proton it is about ~1 ns. This means that, already only due to the time-of-flight of primary particles, the initial bunch of ions emitted within tens of fs is stretched up to the ns range. In addition to this, secondary neutrons will also have to travel from their production site to the detector position, whose distance could be normally in the ~1 m range. By doing a similar calculation for neutrons as done before for protons one can calculate that the bunch of neutrons is stretched up to dozens of ns, even hundreds, if one considers also epithermal neutrons, and therefore the actual T_{bunch} in this case is to be assumed in the range of dozens-hundreds of ns.

On the other hand, the repetition frequency of the secondary pulsed field will totally reflect the repetition frequency of the laser-target interaction, and therefore, it will range from a shot-on-demand basis to a maximum of 1-10 Hz, corresponding to periods T from 0.1 s to minutes (even hours for the largest laser systems). For this reason, the dose rate in the bunch, DR_{bunch}, differs by several orders of magnitude from the dose rate averaged over one period DR_{avg}. This in turns means that even if a detector is in principle able to measure in a constant field with a mean dose of $\approx DR_{avg}$, it might not be able to do so in a pulsed neutron environment characterized by the same DR_{avg}, due to saturation effects in the measurements during the bunch of radiation, whose dose rate is instead DR_{bunch}.

3.2 Basics of neutron detection

Before describing the different detection techniques used to carry out this work into detail, it is worth reminding that neutrons do not possess electrical charge and, therefore, detection techniques usually employed to detect directly ionizing radiation (e.g., e^-, X or γ-rays and ions) are not directly suitable for the detection of neutrons. The detection of neutrons, thus, generally relies on the exploitation of a nuclear reaction that produces charged particles. It is then these reaction products that can be detected and interpreted

as neutron-related signal, by knowing the open reaction channels and the detector design [49]. In the following, the most employed nuclear reactions used for neutron detection are briefly discussed.

Several parameters are of importance when searching for a suitable material for neutron detection. First, the cross section, σ_n, for the specific neutron-induced reaction should be as high as possible in the energy region of interest. This will ensure a high neutron detection efficiency that can translate into small detector sizes. Second, the isotopic abundance of such nuclide is important because it will directly affect the market price of a given amount of material. In case an active discrimination over photons is needed, also the Q-value of the neutron-induced reaction has to be taken into account: the higher its Q-value is, the easier is the discrimination over photons [49].

Concerning the detection of thermal neutrons and following the abovementioned guidelines, two of the most nowadays used nuclei are ^{3}He and ^{10}B.

Helium-3

^{3}He shows a rather high neutron reaction cross section at thermal energies of about 5330 b. It has only one reaction channel possible, described by the following reaction:

$$ {}^{3}_{2}He + n \rightarrow {}^{3}_{1}H + p + 0.764\text{MeV} \quad (1) $$

The liberated energy or Q-value (0.764 MeV) is shared by the kinetic energies of the two reaction products (a tritium ion and a proton) by applying the conservation laws of energy and momentum:

$$ E_p = 0.573\text{MeV} \quad \text{and} \quad E_{{}^{3}_{1}H} = 0.191\text{MeV} \quad (2) $$

Although ^{3}He is not a natural isotope of Helium, large quantities of ^{3}He were accumulated as by-product of the tritium-based nuclear weapon industry. However, recently ^{3}He has become more and more expensive, as a result of the nuclear disarmament programs.

Boron-10

Since decades ^{10}B offers a rather good alternative to ^{3}He, thanks to its higher reaction Q-value, and rather high reaction cross section at thermal energies (3,840 b), although lower than the one of ^{3}He. Another positive aspect of ^{10}B is that it is a stable isotope of Boron, with isotopic abundance of almost 20%. Neutron-induced reactions with ^{10}B include the emission of a ^{7}Li and an α-particle, with two possible reaction outcomes, one with ^{7}Li in its ground state (6% probability) and one with ^{7}Li in an excited state (94% probability). The reaction is described as follows:

$$ {}^{10}_{5}B + n \rightarrow \begin{cases} {}^{7}_{3}Li + \alpha + 2.79\ MeV\ (6\%) \\ {}^{7}_{3}Li^{*} + \alpha + \gamma(0.48\ MeV) + 2.31\ MeV\ (94\%) \end{cases} \quad (3) $$

Other nuclei

Other widely used isotopes for thermal neutron detection are ^{6}Li, specially as converter for scintillators [50] or track-etched detectors, and ^{235}U or ^{239}Pu, mainly as detecting medium in fission chambers. In particular, fission reactions possess the positive feature of having much higher Q-values compared to any other neutron-induced reaction (about 200 MeV). The practical drawback that sometimes discourages their employment is that U and Pu always require special handling, being radioactive and fissile materials [49].

Activation reactions

Other widely used thermal neutron reactions, especially for applications at very high neutron fluxes, are neutron capture reactions. Here, the neutron interaction leaves the nucleus in an excited state from which it de-excites, after a given time (for measurement purposes in the range from hours to days) and following a specific reaction decay pattern. As a result of the de-excitation, characteristic gamma rays are often emitted. This whole process is commonly referred to as *neutron activation* because the detecting medium is made artificially radioactive after being exposed to neutron radiation. By measuring the neutron-induced activity of a sample and by knowing the response function of the specific detector geometry, it is possible to infer the neutron flux responsible for its activation, in terms of field magnitude and, for some cases, also neutron energy. Examples of thermal neutron activation isotopes are ^{197}Au, ^{115}In, and ^{63}Cu. For the detection of fast neutrons other isotopes are used, such as ^{64}Zn [3], ^{24}Mg [4], or ^{19}F [5]. These latter show different neutron energy thresholds, below which the interaction probability is negligible, while above an interaction channel opens, and activation becomes more probable. By measuring the same field with different detector isotopes, information on the energy of the interacting neutrons (i.e., their energy spectrum) can be reconstructed [49].

3.3 Detection techniques used in the present work

In the following both *active* and *passive* neutron detection techniques used in the present work are discussed in terms of strengths and weaknesses peculiar of each technique.

[3] ^{64}Zn(n,p)^{64}Cu, threshold energy = 2 MeV
[4] ^{24}Mg(n,p)^{24}Na, threshold energy = 6 MeV
[5] ^{19}F(n,2n)^{18}F, threshold energy = 11.6 MeV

Despite different neutron detection techniques exist, it was decided in this thesis to focus on neutron moderator-type detectors. These detectors make use of materials rich in low Z isotopes (e.g., polyethylene or paraffin wax) to slow down the incoming neutrons to thermal energies and then use a thermal neutron detector (either active or passive) to measure them. Use of moderators benefits from the fact that reaction cross sections for thermal neutrons are higher for a large variety of isotopes compared to those for high energy neutrons, increasing the probability of neutron detection. Additionally, the way neutrons are moderated from their initial energy to thermal energy is through elastic nuclear scattering with the nuclei of the moderator, a process that takes some time (hundreds of μs [51]) if compared with the initial neutron bunch length (tens to hundreds of ns). Therefore, even if a neutron bunch has a temporal spread of only a few dozens of ns (as it was roughly calculated for laser-driven ion sources in 3.1), when the neutron bunch enters the moderator, scattering events, together with a reduction in the energy of the impinging neutrons, would also stretch the neutron bunch in time. This results in a lower number of neutrons per unit time interacting with the detecting medium, relaxing the requirements on the speed of the acquisition electronics, in the case of active detection.

3.3.1 Active techniques

As mentioned, the result of a neutron-induced reaction is in many cases the production of energetic ions as reaction products. The privileged way to actively measure these reaction products is by exploiting the fact that charged particles crossing a medium (e.g., a volume filled with gas) ionize its molecules and hence produce a large quantity of free electrons and ions. By applying a potential difference to the volume where the interaction takes place (which is called *active volume*), electrons and ions of the ionized gas will travel towards cathode and anode, respectively. The measurement of this produced charge, either in the form of a voltage drop or a current, is then an indirect way of detecting neutrons. More specifically, three different acquisition modes exist to process the produced charge in the active volume: *current* acquisition mode, *mean square voltage* acquisition mode (MSV) and *pulse* mode. The current acquisition mode is preferred when high interaction rates and low photon-to-neutron signals are expected, as is typical for in-core neutron detectors. The MSV mode is based on a particular handling of the fluctuating fraction of the current signal. It is mostly employed when radiation species producing different amounts of charge are to be measured. Finally, the pulse mode is by far the most widely used acquisition mode when it comes to applications that require the

detection of single neutron interactions, and therefore high sensitivity, that is typically the case for radiation protection devices as the ones described in the next paragraphs.

3.3.1.1 Active REM counters

The invention of the neutron REM[6] counter is to be attributed to Andersson and Braun in 1964 [52]. This detector type directly measures the neutron dose, as the name suggests, despite the fact that nowadays the dose is no longer measured in units of *rem* but instead in Sievert (Sv)[7]. The importance of this type of detector stems from the fact that it is routinely used when it comes to surveying the neutron ambient dose at accelerator facilities.

Active neutron REM counters are based on a thermal neutron detector (usually a proportional counter) placed at the center of a neutron-moderating material. In this way only those neutrons that reach thermal energies through scattering in the moderator have a probability high enough to get detected. The key feature of a REM counter, compared to other moderator-based neutron detectors, is that the moderator assembly is shaped (in terms of size and material composition) in a way that the response of the counter mimics the fluence-to-dose conversion curve for neutrons, allowing the detector to measure neutron dose regardless the energy spectrum of the neutron field.

Most of active conventional REM counters make use of a proportional counter, filled with either ^{3}He or BF_3 (with either natural boron or boron enriched in ^{10}B) as thermal neutron detector, and a moderator assembly made of polyethylene or paraffin wax. Such devices can measure the neutron dose in neutron fields with energy spectra ranging from thermal to 20 MeV.

To increase the response of neutron REM counters above 20 MeV, lead shells (or other high Z materials) are usually used. These, thanks to (n, xn) reactions, increase the detection probability of high energy-neutrons, which otherwise would not reach thermal energies by simply exploiting neutron scattering [53–55]. In this way, nowadays so-called extended-range neutron REM counters can easily measure the neutron dose in radiation fields characterized by neutrons up to hundreds of MeV. They are widely used in radiation protection at ion and electron accelerator facilities, as is the case, for instance, for the LINUS described by *Birattari et al.* [56].

The NM2B-495Pb and the NM2B-458

[6] REM = Röntgen Equivalent Man

[7] 1 Sv = 100 rem

The NM2B-458 and the NM2B-495Pb are both Andersson–Braun neutron REM counters, produced and commercialized by NE Technology Ltd. (bought by Thermo Electron Corporation in 2001, now part of Thermo Fischer Scientific). They both consists of a cylindrical BF_3 proportional counter with active volume 7.2 cm long and 3.1 cm in diameter, surrounded by an inner moderating polyethylene layer (1.7 cm thick), and a 0.6 cm thick boron-doped synthetic rubber absorber. In addition, the NM2B-495Pb has a 1 cm thick lead shell used to extend the detector response to high energy neutron fields [57]. The energy-dependent response function of these detectors was calculated by using various Monte Carlo codes [57], while neutron dose calibration was performed by using a neutron AmBe source.

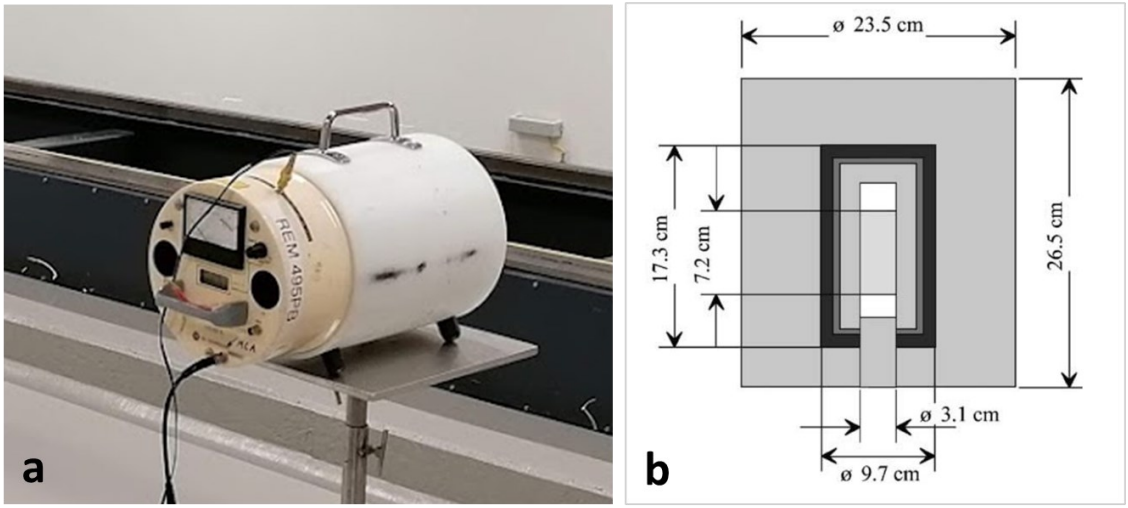

Figure 5: NM2B-495Pb neutron REM counter. **a**) REM counter during a test irradiation in the former SSDL of the Helmholtz Zentrum München. **b**) Schematic drawing of the REM counter (electronics excluded): in dark gray are the polyethylene elements, in black the lead shell while in light gray the active volume place ad the center of the moderator assembly (figure adapted from *Mares et al*. [57]).

Similarly to most of radiation detectors, the electronics of both NM2B devices is based on the aforementioned pulse mode acquisition chain. Using this acquisition mode, when a neutron interacts in the active medium, the charge produced by the single interaction creates a voltage drop whose height is measured. The height of the pulse is a measure of the charge liberated by the interaction. Consequently, since the Q-value of the $^{10}B(n,\alpha)^{7}Li$ reaction is known, it is possible to discriminate those pulses belonging to neutrons from those belonging to photons or other particles by applying a threshold on the pulse height.

Pulse mode acquisition has the great advantage of separately recording each single neutron interaction, but has the disadvantage that pulse shaping takes up to some µs. This is a time in which the electronics is not able to record any other possibly incoming pulse correctly. During this time, which is also known as *dead time*, τ, if a pulse arrives, its produced charge is either discarded or added on top of the already collected charge, creating the phenomenon of the *pile-up* of pulses. A piled-up pulse cannot be easily interpreted since the charge information of the initial pulse has been distorted. The direct consequence is that the dead time limits the number of true pulses that such a detector can correctly measure.

If one wants to use this device in a pulsed radiation environment, one needs to know the maximum D_{bunch} that the device is able to measure free from dead time losses. The initial length of the neutron bunch is of the order of ns. As mentioned above, it can be roughly estimated that the neutron thermalization and diffusion process in the moderator stretches the initial bunch length to about a few hundred microseconds [51]. To perform a measurement *free*[8] from dead time losses, the maximum interaction rate in the detector needs to be less than 1/10τ. The maximum number of detectable counts, C, in a single bunch of radiation can be then estimated by multiplying the stretched bunch length by the maximum interaction rate:

$$C = T_{TD} \cdot \frac{1}{10\tau} \tag{4}$$

Assuming, T_{TD} = 400 µs, and τ = 4 µs, one gets that the maximum number of counts per bunch is 10. If one then considers that this device has a sensitivity of 1 nSv/ct, one gets that the maximum detectable neutron dose per bunch free from dead time losses is about 10 nSv.

An experimental study published by *Caresana et al.* [58] showed that most conventional REM counters start showing dose underestimation effects at around 10-20 nSv/bunch, in accordance with the rough calculation showed above.

LUPIN 5401 BF3-NP PSI detector

The LUPIN 5401 BF3-NP PSI (in the following simply LUPIN-II) is a cylindrical neutron REM counter type instrument based on a BF_3 proportional tube produced and commercialized by ELSE Nuclear (Busto Arsizio, Italy). The first version of this detector was developed in 2011 and it was based on a ^{3}He spherical proportional counter [59]. An

[8] *Free* in the sense that only 10% of expected counts is affected by dead time losses

upgrade was made in 2014 from the ^{3}He spherical version to the current BF_3 cylindrical version, which took therefore the name of LUPIN-II [60]. Some additional minor modifications to the controlling electronics and interface were required by the Paul Scherrer Institute (PSI) in 2016 to use the LUPIN as part of a radiation protection system at the Swiss Free Electron Laser, SwissFEL. The version of the LUPIN used in this work is the one currently employed at PSI [61].

The Centronics BF_3 proportional counter used by the LUPIN is 15 cm long and has a diameter of 2.5 cm. It is filled with a pressure of 0.13 kPa and its operating high voltage is 1,180 kV. A polyethylene moderator assembly, with cadmium inserts and a lead layer surrounds the proportional counter and, similarly to other neutron REM counters, allows the detector to directly measure the neutron dose in terms of neutron H*(10).

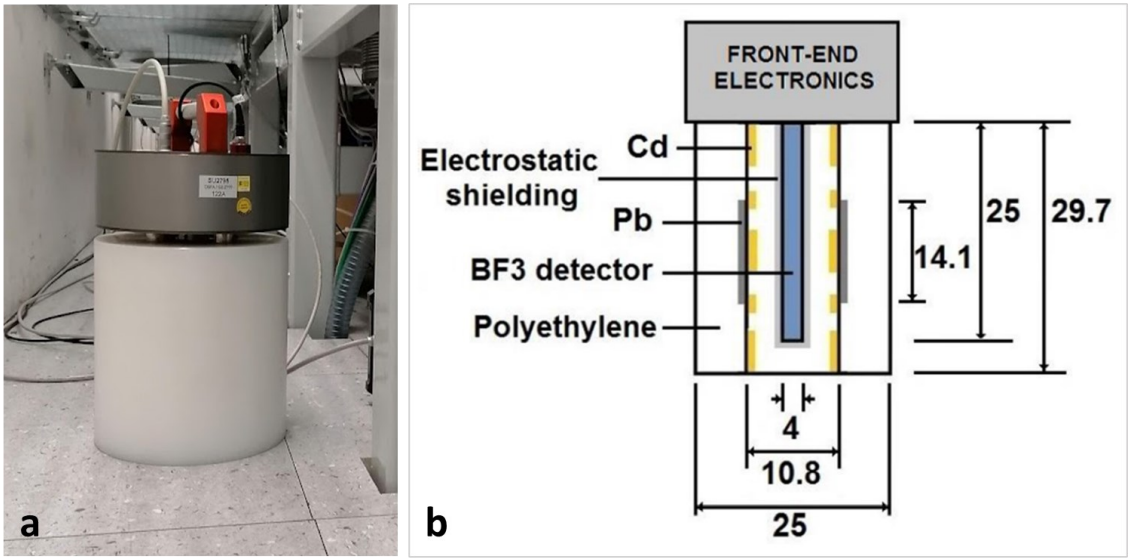

Figure 6: LUPIN-II neutron REM counter. **a**) Counter during a test measurement at the Electron Thomson Test Facility, ETTF (Garching near Munich). **b**) Schematic drawing of the detector with dimensions and description of the materials (picture adapted from *Caresana et al.* [60]).

The main feature of the LUPIN-II is its capability to measure in environments dominated by pulsed neutron radiation. Measurements performed in pulsed neutron fields showed that the detector can withstand doses per bunch up to 500 nSv with only 20% underestimation of the real delivered dose [60], a factor ~50 better response in pulsed neutron fields compared to other commercially available conventional REM counters. At the same time, the LUPIN-II has a sensitivity of about 2 counts/nSv, a value comparable to other similar ambient dose detectors used for radiation protection purposes.

Instead of using the pulse acquisition technique that suffers from dead time losses, the LUPIN is driven in *current mode*. The current produced in the proportional counter is integrated over a fixed amount of time and divided by the mean collected charge (MCC). The MCC corresponds to the charge produced by one single neutron interaction; its value is experimentally determined by irradiations at a very low neutron fluence and specified by the manufacturer. This results in a total number of neutron interactions in a given amount of time, free from dead time losses. Simply using the current acquisition mode would not be sufficient, however, because together with neutrons also secondary photons can interact and produce charges in the proportional counter. These charges would then be ascribed to neutron interactions and a wrong number of neutron interactions would then be calculated [60].

For this reason, the LUPIN-II uses the so-called *derivative technique*: the current signal produced in the proportional counter is derived and a threshold is applied to the derivative of the signal. The interaction of a neutron with ^{10}B releases a lot of energy compared to the energy deposited by a gamma photon in a gaseous medium. For this reason, the derivative of a neutron-induced signal is greater than the derivative of a photon-induced signal, even when more than one photon interacts at the same time. Based on this principle an efficient photon rejection can be achieved [60].

3.3.2 Passive techniques

Passive techniques offer a positive aspect when dealing with pulsed radiation: they are not affected by the bunch intensity. As it was seen in 3.3.1, the intensity of the neutron bunch is the main drawback for using active techniques at laser-driven particle accelerators. Passive techniques, as neutron activation techniques for instance, overcome this obstacle simply by not having any active signals to acquire. On the other hand, being passive detectors, they can only be read-out *after* being exposed, making their use for online assessment of neutron fluence or dose impossible.

3.3.2.1 Track-etched detectors

A widely used passive technique for the detection of neutrons makes use of so-called track-etched detectors. Their working principle relies on the production of tracks in a solid-state material (usually plastics) due to recoil protons or charged particles, resulting from neutron-induced reactions in converter materials. Specific converters are used to increase the probability of a given reaction to happen, such as ^{10}B or ^{6}Li. Once the de-

tector has been exposed to neutron radiation and tracks have been created in the detecting material, the detector undergoes a well-calibrated chemical etching process that, although attacking the entire surface of the material, enlarges the tracks produced by the charged particles and makes them easily visible (and countable) by an optical microscope [62]. Thanks to their low cost and small dimensions and to the well-established employment in the field, track-etched detectors are commonly used for personal dosimetry where neutron exposure is expected. One of the currently most-used plastics is the CR39 or Poly-Allyl Diglycol Carbonate (PADC) [63].

In the department of energy of Politecnico di Milano, Italy, a CR39-based neutron REM counter called Passive LINUS has been developed and characterized in order to serve as passive neutron REM counter for ambient dose measurements [64]. The thermal neutron detector is composed of a sandwich of two CR39 samples coupled with two Enriched Converter Screens BE10 (produced by Dosirad, Pierrelatte, France).

Such thermal detector is placed in a polyethylene detector holder located at the center of a moderator sphere mainly made of polyethylene, with cadmium inserts and with a 0.6 cm thick shell of lead, used to extend the detector response to high-energy neutrons by exploiting (n, xn) reactions [53]. As for other REM counters, the principle behind is that such moderator gives the detector an energy response function that mimics the fluence-to-H*(10) conversion curve.

After irradiation, the CR39 sample undergoes chemical etching through a 40-minute-long bath in a 6.25 N NaOH aqueous solution at 97.7 ± 0.1 °C. After this, the detectors are extracted from the chemical bath, rinsed, and immersed in a solution of acetic acid 2% in volume for about 45 minutes. This last step is performed to neutralize any possible basic residues. The parameters of the etching process are tuned by simultaneously treating some “feedback” detectors, previously irradiated at Politecnico di Milano with a Cf-252 reference source.

Once this is done, the samples are ready to be read by using a commercial reader developed at Politecnico di Milano in collaboration with Mi.am s.r.l (Piacenza, Italy), called *Politrack*® (see Figure 7a). The reader consists of an optical microscope coupled with a 1/3” CCD camera (pixel size corresponds to ~ 0.2 μm^2). The etched CR39 samples are placed on a motorized XY support, in order to preform automatic sample scanning. Data from the camera are sent to an acquisition PC unit by using USB3 interface and are analysed by a dedicated software.

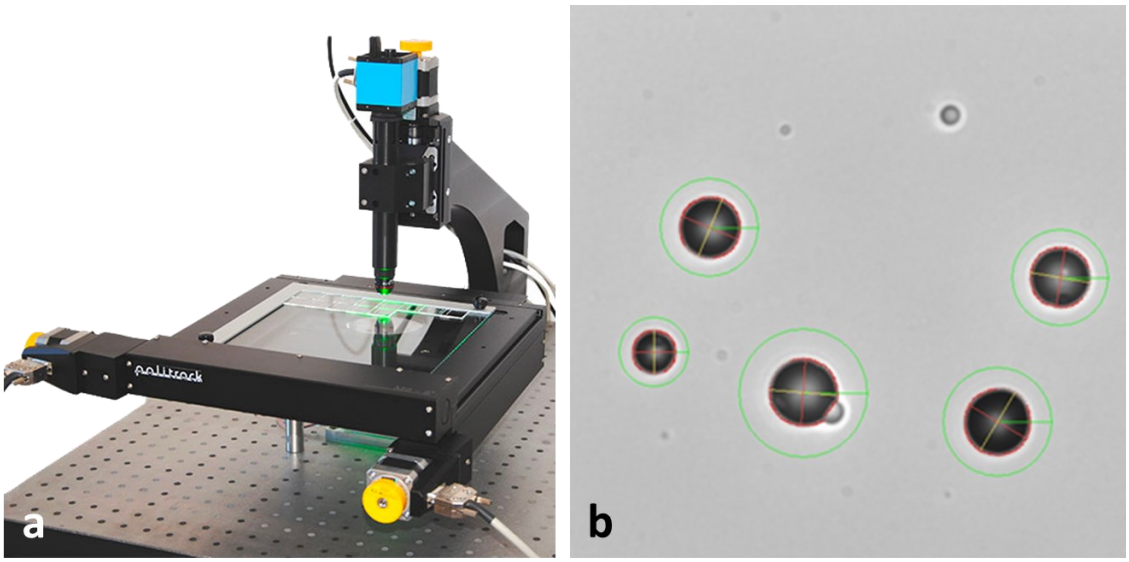

Figure 7: **a**) *Politrack*® system (from Mi.am s.r.l. website) and **b**) example of thermal neutron-induced tracks (from *Politrack*® manual).

When a measurement is performed, in order to derive a background estimation, a few unexposed test detectors are usually analyzed too. The average track density (tracks/cm^2) is then subtracted from the total (or gross) track density found on the exposed samples. This step is crucial when performing low dose measurements.

According to *Caresana et al.* [64], the Passive LINUS shows a sensitivity in the order of 5 tracks/cm^2/μSv and about 7 tracks/cm^2 of intrinsic noise, mainly due to surface imperfections.

For the measurements presented in this work, an innovative boron converter made of a metal support coated with boron carbide (99% enriched in ^{10}B) was used instead of the BE10, to increase the detector sensitivity (Figure 8a and b). For this reason, a specific calibration of this detector was performed in the calibration laboratory of the Paul Scherrer Institute, Switzerland, as a joint activity with Politecnico di Milano (description in Chapter 5.1).

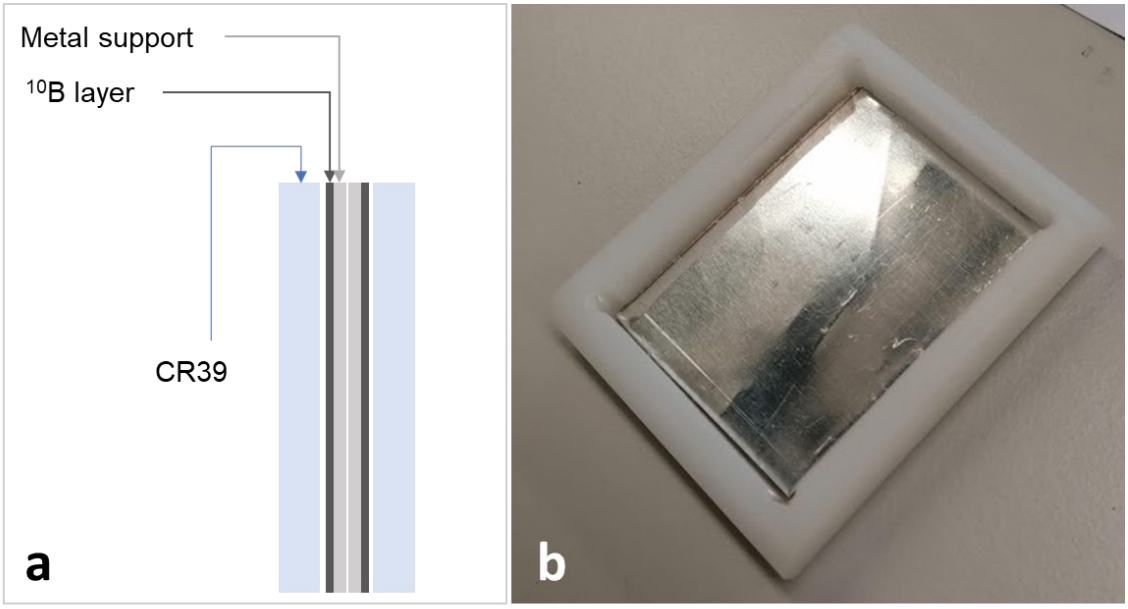

Figure 8: Passive LINUS thermal neutron detector. **a**) Drawing of the sandwich CR39-active layer-active layer-CR39. **b**) Thermal neutron detector hosted inside its polyethylene holder.

3.3.2.2 Au-foil-based Bonner Sphere Spectrometry

Bonner Sphere Spectrometer (BSS)

A Bonner Sphere Spectrometer (BSS) represents a neutron detection system that allows the measurement of the spectral information of a neutron field by using a set of neutron-moderating spheres of different diameters coupled with a thermal neutron detector placed at their center. Such neutron spectrometer was firstly reported in the literature by *Bramblett, Ewing and Bonner* back in 1960 [65] as a set of five polyethylene spheres of different diameters coupled with a ^{6}LiI(Eu) scintillator. As one can imagine, for a given sphere diameter, only neutrons with a given energy have a high probability to thermalize and reach the thermal neutron detector. Those with lower energy will probably undergo neutron capture in the moderator, while those with higher energy will most likely escape the moderator before thermalizing. Therefore, each moderating sphere has a different neutron-energy-dependent response, depending on its diameter.

Conventional BSSs use a set 10-15 spheres and cover a neutron energy spectrum that goes from thermal energies up to 20 MeV [66,67]. As it is done for neutron REM coun-

ters, in order to detect neutrons with higher energy up to several hundreds of MeV, materials composed by high Z elements are added and (n, xn) reactions are exploited. This is practically done by adding a few spheres with intermediate size with an additional lead or copper shell [68]. Given the larger energy range, this system is referred to as Extended Range Bonner Sphere Spectrometer, or ERBSS.

For a BSS or ERBSS composed by m spheres, if the i^{th} sphere is exposed to a given neutron field characterized by a neutron fluence, $\Phi(E)$, the number of counts, M_i, in the detector that will be measured will be:

$$M_i = \int R_i(E)\Phi(E)dE \tag{5}$$

Where $R_i(E)$ is the energy-dependent response function of the i^{th} sphere.

Equation (5) also takes the name of Fredholm integral. The mono-dimensional vector M (formed when all spheres are irradiated) is also commonly referred to as *measurement vector* and has, by definition, dimension m. Since usually the response of a Bonner sphere is a discrete function calculated by using Monte Carlo codes, Equation (5) should be rewritten in its discrete form:

$$M_i = \sum R_{ij}\Phi_j \tag{6}$$

Where R_{ij} is called *response matrix* and the subscript j runs from the lowest energy bin, 1, to the maximum energy bin, n, while i , as before, ranges from 1 to m, the total number of spheres.

Aim of the spectrometry is to extract from the vector M information on the neutron fluence, Φ, that produced it: this process takes the name of *unfolding*.

Equation (6) is unfortunately an ill-conditioned problem and has therefore infinite acceptable mathematical solutions which, however, not necessarily have also physical meaning. To restrict the results to only a physically meaningful solution, additional information is required, such as a *guess spectrum*, i.e., a spectrum that includes the physically expected shape as for example provided by Monte Carlo simulations or by physical considerations.

Several so-called unfolding codes have been developed using different mathematical approaches, such as, regularization [69], iterative procedures, entropy maximization [70] or artificial neural nets [71]. The unfolding code used in the Medical and Environmental Dosimetry group (MED) of the Institute of Radiation Medicine (IRM) of the Helmholtz-

Zentrum München is MSANDB [72]. MSANDB is based on iterative procedures and requires as input parameters a guess spectrum, the BSS system response matrix, R_{ij}, and the measurement vector, M. As first step, the guess spectrum is folded with the system response matrix and a calculated vector, C, is produced. Then the code compares the calculated vector with the measured one, M, through a χ^2-test. If the difference is below a predefined value the calculation is stopped, otherwise, the guess spectrum is slightly modified, and the comparison is repeated iteratively until the difference is less than the predefined value. The detailed procedure is described in Appendix B. 300 to 500 iterations are usually required to reach the convergence of the solution [73].

^{197}Au as thermal neutron detector

Passive Bonner Sphere Spectrometry is a technique that has already been applied in the MED group of the IRM. For this a gold-foil-based Bonner Sphere Spectrometer (Figure 9) was developed to perform high neutron fluence measurements at the MEDAPP facility (Garching near Munich, Germany) [74].

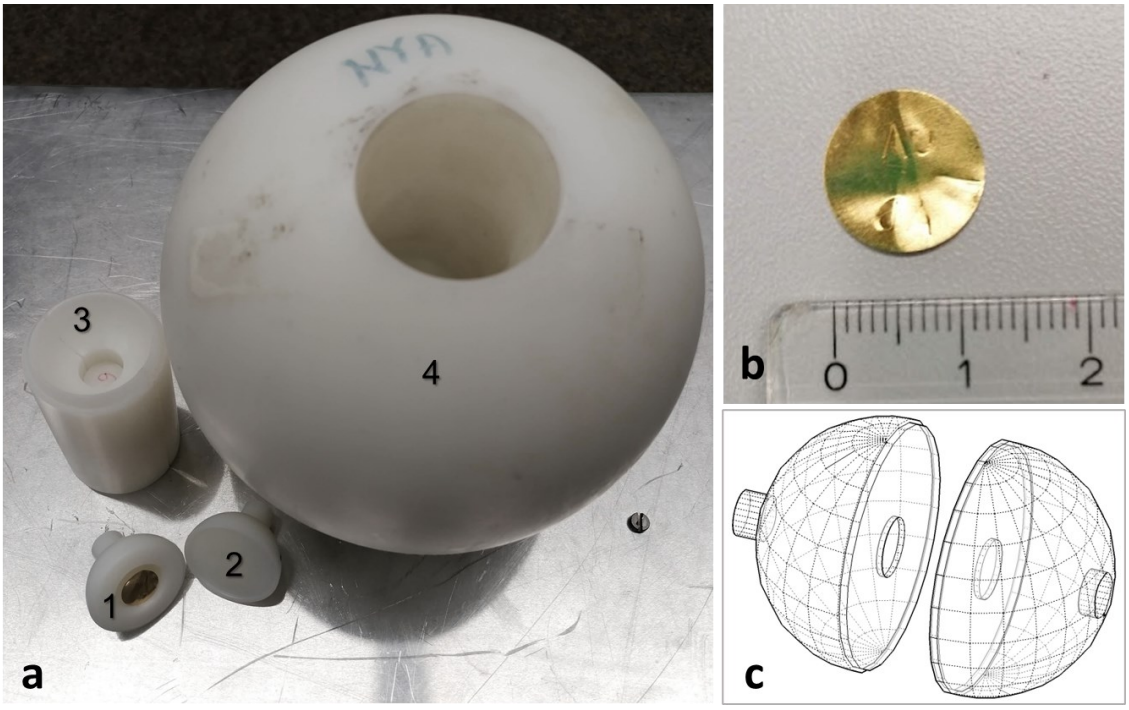

Figure 9: **a**) Au foil (1) placed inside its holder (2), holder adapter (3) and 6" sphere of the BSS (4). **b**) Au foil with ruler to help visualizing its dimensions. **c**) Sketch of the sample holder.

^{197}Au (the only stable isotope of gold), when exposed to neutrons, may undergo a neutron capture reaction (n,γ) transforming into ^{198}Au. With a half-life of 2.69 days, ^{198}Au

beta-decays to an excited state of ^{198}Hg (99.975%) which rapidly undergoes a gamma decay emitting a photon with the characteristic energy of 411.8 keV. The probability of this reaction to happen is well described by the energy-dependent reaction cross section, $\sigma_{n,\gamma}(E)$, shown in Figure 10. The cross section decreases with increasing energy following the typical $1/v$ behavior (v being the neutron velocity), except for a well-defined resonance at 4.9 eV energy and many additional minor resonances at higher energies.

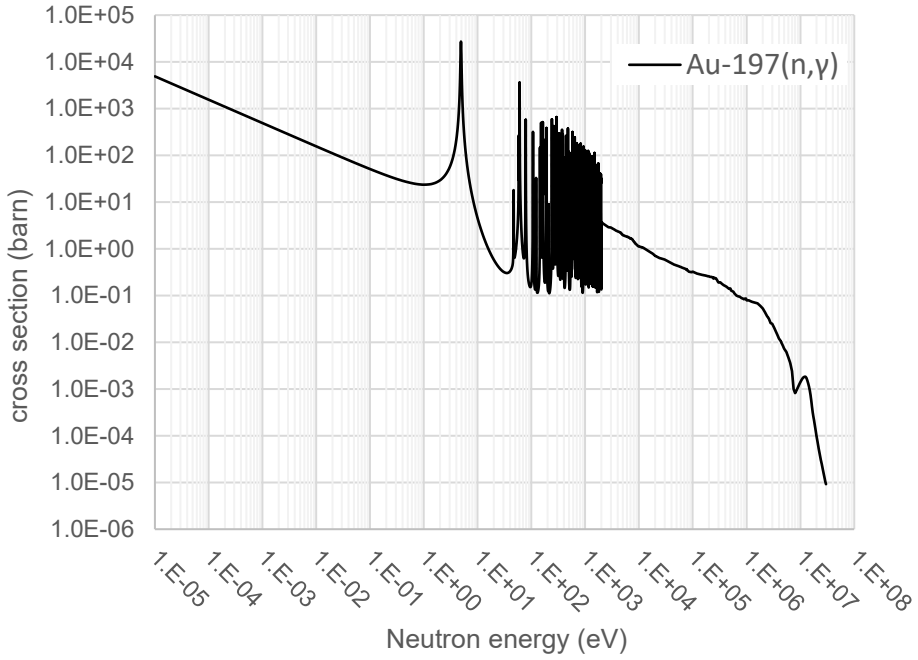

Figure 10: Energy dependent cross section of the (n,γ) reaction on ^{197}Au. Data taken from the ENDF/B-VIII.0 cross section library.

Given its high reaction cross section at thermal energies (and low cross section at epithermal and high energies), gold proves to be a good thermal neutron monitor, allowing its use as thermal neutron detector inside a moderated-type neutron detector (e.g., REM counter or Bonner Sphere Spectrometer). The only inconvenience is posed by the presence of the 4.9 eV resonance which favorites the interaction of gold with a neutron before this latter has reached thermal energies. This is usually bypassed by using a thin cadmium cladding. When the gold foil is enclosed into a cadmium cladding, due to the very high reaction cross section of cadmium for energies below the so-called cadmium edge ($E_{Cd-edge}$ ≈ 0.5 eV), almost no neutron with energy below $E_{Cd-edge}$ is able to interact (and therefore, activate) with the gold foil. Thus, if the same neutron field is measured once with cadmium cladding and then without, the activity resulting from the subtraction of the measurements with and without gives the activity due to thermal neutrons only.

In order to perform a complete gold activation measurement, first, the gold detector needs to be exposed to the neutron field of interest. Then the activated detector is transported to a gamma spectroscopy laboratory where its activity is measured with a gamma spectrometer. In this thesis different Ge detectors with different geometries and different MDA (Minimum Detectable Activity) were used. After calibrating three Ge spectrometers it was found that the best performance was reached by using a Ge bore-hole detector (MDA ≈ $5 \cdot 10^{-3}$ Bq). Details on MDA calculations are given in Appendix C.

For a full neutron spectrometry, all Bonner spheres (knowing the main features of the spectrum to be measured, even only 6-7 spheres could be enough) need to be used to measure the field once with Cd cladding, once without, resulting in a total of at least 12-14 measurements for each experimental position. The measured activity vector is then unfolded by using the dedicated unfolding code MSANDB and, in such way, the neutron spectrum is found.

The system described and employed by *Garny* [74] used, as thermal neutron detector, a gold foil that measured 1 cm in diameter and 23 μm in thickness for a total mass of about 30 mg. The gold foils used in the present thesis had slightly different dimensions, 1.25 cm in diameter and 50 μm thickness, for a mass of 125 mg, offering a factor 4.16 higher sensitivity due to the increased mass.

Given that the geometry of the spheres remained unchanged either by using the old or the new gold foil dimensions, it was assumed that the response functions of the BSS expressed in cm^2/mg shown in [74] were still valid (Figure 11). Of course, when calculating the expected activity due to a given neutron fluence, the mass of the new gold foils was considered, yielding to a factor 4.16 higher activity compared to using the old gold foils. Figure 9a shows the components of a Bonner sphere (6”) with a gold foil, sample holder and holder adapter. A close-up on the gold foil is given in Figure 9b while a sketch of the sample holder is shown in Figure 9c.

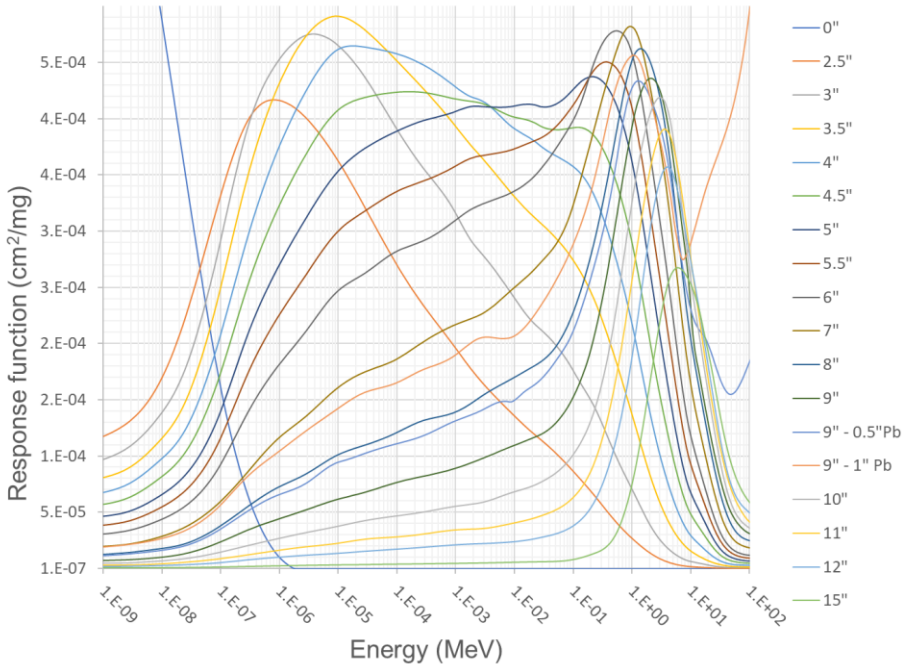

Figure 11: Response functions of the Au-ERBSS. Data points have been taken from [74] and spline interpolated.

4. Monte Carlo simulations

4.1 Basics

For the simulation of the production of secondary radiation at laser-driven particle sources, the Geant4 10.4 Monte Carlo simulation toolkit has been used [75,76]. Geant4 (short for GEometry ANd Tracking) is an opensource Monte Carlo toolkit written in C++ originally developed at CERN and nowadays worldwide used for applications involving the transport of particles through matter, going from high energy physics to medical applications.

Geant4 is an object-oriented toolkit where predefined classes allow the user to define geometries, materials, particle scorers and physics modules to be included in the simulation (discarding not relevant interaction mechanisms and speeding up the code). In addition, the user is free to define his/her own output modalities and external macro input files can be used to define complex source terms. The main motivation for choosing Geant4 over other well-known Monte Carlo codes in the course of this work stems, in fact, from the high flexibility and customizability that Geant4 offers.

4.2 Source terms

Geant4 allows the user to define particle source terms with arbitrary position, emission direction, energy spectrum, angular distribution and source shape, a helpful feature when it comes to modeling the complex particle “beams” emerging from a laser-target interaction. This was managed using the predefined general particle source (`/gps`) commands in an input macro file. In the example shown in Figure 12, the command `/gps/particle proton` is used to select protons as source particle. In addition, `gps/pos`, `gps/type` and `gps/ang` are used to set the position of the source, its type, and its angular distribution. The spectral properties of the source are managed by the commands `/gps/ene/type` and `/gps/hist/type`, while and the actual spectrum of the source is implemented by a list of `gps/hist/point` commands where the first value specifies the energy of the bin (in MeV) and the second value the probability of having a particle with that energy. The histogram is then linearly interpolated by the command `gps/hist/inter/Lin`. Lastly, the simulation is run over a total number of histories as specified by the command `/run/beamOn/`.

```
/gps/particle proton

/gps/pos/type Point
/gps/ang/type iso
/gps/pos/centre 65. 0 -137.75 cm
/gps/ang/rot1 1 0 1
/gps/ang/mintheta 0 deg
/gps/ang/maxtheta 20 deg
/gps/ang/minphi 0 deg
/gps/ang/maxphi 360 deg

/gps/ene/type Arb
/gps/hist/type arb

/gps/hist/point  1    1.04E-01
/gps/hist/point  2    9.31E-02
/gps/hist/point  3    8.34E-02
/gps/hist/point  4    7.48E-02
...
...

/gps/hist/inter Lin
/run/beamOn 500000000
```

Figure 12: Example of macro file used to start the Geant4 simulations, where particle, position, angular distribution, energy spectrum, and number of histories are defined.

4.3 Physics lists

In this work, it was necessary to evaluate the secondary neutron production of primary protons with energies up to several tens of MeV or primary electrons in the range of hundreds of MeV interacting with different materials. For this reason, the Bertini Intranuclear Cascade model (QGSP_BERT_HP) was chosen. This model takes into account electromagnetic showers, synchrotron radiation, and hadron physics, and it is recommended by the Geant4 developers when dealing with industrial and medical neutron applications and radiation shielding studies [77]. Additionally, the HP extension (i.e., NeutronHP, Neutron High Precision) was also included, in order to accurately simulate the transport of neutrons from 20 MeV down to thermal energies.

4.4 Scorers and output options

To detect the neutron and photon fluence in specific regions of interest, the G4PSCellFlux built-in scorer was used. This scorer class returns the user the total flux of particles that passed through a volume of interest in cm^{-2}. To get not only the total fluence in the scored region but also the fluence spectrum, the scorer was divided in 132 energy bins (10 bins per decade), logarithmically equispaced from $8.91 \cdot 10^{-10}$ to $1.12 \cdot 10^{4}$ MeV, and a particle filter was activated to allow the detection of neutrons and photons separately.

Whenever a neutron (or photon) of energy E_0 crosses the scored volume, its track length in the scorer is calculated and divided by the scored volume (resulting in the CellFlux value). At any detection in the given scorer, the involved particle type, energy bin, and CellFlux are printed in a three-column file. Once the simulation is over, a simple self-developed C++ routine summed up the CellFlux value for each energy bin and particle type (neutrons and photons), and created two fluence spectrum files, one for neutrons and one for photons.

Neutron and photon doses per primary particle were simply calculated by folding the neutron and photon spectra, simulated as described above, with the respective ambient dose equivalent (H*(10)) conversion coefficients' histogram. For neutrons this was created by spline interpolation on the data from ICRP74 [78] and from the extension proposed by *Pelliccioni et al.* [79], as described in [80]. Similarly, by folding the neutron spectrum with the response function of a detector, it was also possible to quantify the expected counts the detector would measure if it were positioned at the scorer position. This will be discussed into detail in Subchapter 5.3 when studying the feasibility of different neutron detection techniques.

Fluence maps for neutrons and photons could also be created, first by defining a physical mesh-grid of given x, y, z size, with a given number of bins and positioned at a fixed position (commands `/score/mesh/boxSize`, `/score/mesh/nBin` and `/score/mesh/translate/xyz`). Secondly, the command `/score/quantity/cellFlux` was used that allows the user to score the flux of a given particle for each volume of the mesh grid, as shown in Figure 13. The data were than saved in a dedicated file with the command `/score/quantity/dumpQuantityToFile`.

```
/score/create/boxMesh boxMesh_1

/score/mesh/boxSize 200. 10. 200. cm
/score/mesh/nBin 400 10 400
/score/mesh/translate/xyz 65. 0 -65 cm

/score/quantity/cellFlux cFlux_g
/score/filter/particle gammaFilter gamma
/score/quantity/cellFlux cFlux_n
/score/filter/particle gammaFilter neutron

/score/close

/score/dumpQuantityToFile boxMesh_1 cFlux_n cFlux_n.txt
/score/dumpQuantityToFile boxMesh_1 cFlux_g cFlux_g.txt
```

Figure 13: Example of a Geant4 mesh grid definition.

Further data handling for the creation of mesh-plots was performed by self-developed Python routines.

5. Preparatory studies

The preparatory study towards the application of specific neutron detection techniques in an experimental campaign at a laser-driven ion source have been initially carried out by performing Geant4 Monte Carlo simulations of the laser-driven LION facility, one of the experimental stations operated by the Centre for Advanced Laser Applications (CALA, Garching near Munich, Germany). LION is responsible for the production of laser-driven accelerated protons [81]. In a second step, feasibility studies have been conducted, based on the results of the Monte Carlo simulations, for the different selected measurement techniques. In this chapter, simulations and the feasibility study will be presented in Subchapters 5.2 and 5.3, respectively. In preparation for the actual experimental activity, complementary reference measurements have been also carried out at the calibration laboratory of the Paul Scherrer Institute, these are described in 5.1.

5.1 Irradiations at the PSI calibration laboratory

5.1.1 Reference measurement of active REM counters

As part of this thesis, preliminary reference measurements were performed in the calibration facility of the Paul Scherrer Institut, Switzerland, using the LUPIN-II and both NM2B detectors (all described in Chapter 3). There, measurements were performed with a calibrated AmBe neutron source, delivering a dose rate of 57.3 uSv/h ± 7.11% (2 σ) at 1.5 m distance. Being cylindrical, the LUPIN-II and the two NM2B were irradiated three times, from the front, from the side and from the back, for a total of about one hour irradiation time for each detector. The aim of these reference measurement was to have a comparison of the readings of different instruments, when exposed to the same irradiation conditions in a controlled and reproducible environment.

The results are shown in Figure 14. As it can be seen, all detectors show slightly different measured values depending on the orientation at which they were exposed. Both NM2B detectors measured values lower than the reference value of 57.3 uSv/h (± 7.11%) for all positions, and they are closest to the reference value for the lateral position. On the other hand, the LUPIN measures always more than the reference value except for front exposure, where its reading was slightly lower than the reference value.

Detector	Front (90º)	Lateral (0º)	Back (-90º)
LUPIN-II	57.1 (±0.5%)	64.7 (±0.5%)	56.0 (±0.5%)
NM2B-495Pb	42.3 (±0.8%)	53.7 (±0.4%)	39.4 (±0.9%)
NM2B-458	33.3 (±0.5%)	51.1 (±0.2%)	41.7 (±0.8%)

Table 1: Results of the reference measurements perfomed with the LUPIN-II, the NM2B-495Pb and the NM2B-458, in the calibration laboratory of PSI. In brackets relative statistical uncertainties are reported (1 σ).

All three REM counters displayed their maximum reading for the lateral position. The angular dependence of the LUPIN agreed with the ± 20% stated by the manufacturer in the technical specification note of the device [82]. For what concerns the two NM2B, angular dependences of more than 30% were observed. Although such information is not provided by the manufacturer, nor it is reported in the literature, this has been already observed in test measurements performed in the former Secondary Standard Dosimetry Laboratory of the Helmholtz Zentrum München.

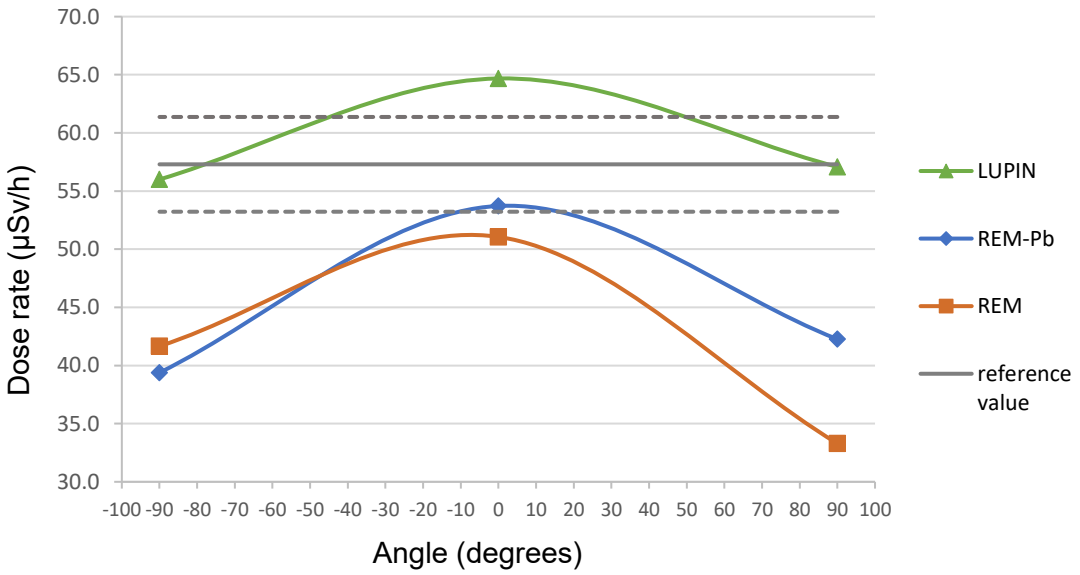

Figure 14: Neutron dose rates measured by the LUPIN-II, the NM2B-495Pb and the NM2B-458, in the calibration laboratory of PSI. Irradiations from the back (-90º), side (0º) and front (90º) are shown together with a spline interpolation to guide the eye (numerical data are given in Table 1).

5.1.2 Calibration of Passive LINUS

On the same occasion, in collaboration with Politecnico di Milano, the CR39-based Passive LINUS was calibrated by using the same irradiation conditions (see Figure 15). The only difference was the exposure time, set to four hours in order to reach an accumulated dose of more than 200 uSv.

Figure 15: Measurement setup for the calibration of the Passive LINUS.

Aim of this measurement was to define a calibration factor to convert the number of tracks detected on the CR39 surface to ambient neutron dose, for the Passive LINUS using the novel thermal neutron detector design (Figure 8). Additionally, three different plastics from two different vendors were used, in order to find out the best candidate in terms of sensitivity and signal to noise ratio. The used plastics were:

- Intercast (Intercast Europe s.r.l, Parma, Italy)
- RTP Batch 1 (RTP Company, Winona, MN, USA)
- RTP Batch 2 (RTP Company, Winona, MN, USA)

Two irradiations were performed for the Intercast CR39 (four samples in total) and one irradiation for both RTP Batch 1 and RTP Batch 2 (i.e., two samples for each batch). Two unirradiated samples of each CR39 plastics were analyzed to estimate the magnitude of the intrinsic noise due to plastic defects.

The results of these calibration measurements are summarized in Table 2, for each of the CR39 plastics used. The second column reports the average gross track density (cm^{-}

^{2}), the third column reports the average intrinsic noise detected on the unirradiated samples, while on the fourth column the average net track density derived by subtracting the background from the gross track density. The calibration factor or sensitivity, C_f, was found by dividing the calibration dose of 228.4 μSv by the average net track density. The last column shows the signal-to-noise ratio (S/N) calculated by dividing the gross track density by the background.

CR39 name	Gross track density (cm^{-2})	Intrinsic noise (cm^{-2})	Net track density (cm^{-2})	Sensitivity C_f ($\mu Sv^{-1}cm^{-2}$)	S/N
Intercast	4,313 (±2%)	28 (±25%)	4,285 (±2%)	18.70 (±7%)	154 (±25%)
RTP Batch 1	3,631 (±4%)	35 (±6%)	3,596 (±4%)	15.69 (±8%)	104 (±7%)
RTP Batch 2	4,652 (±1%)	183 (±48%)	4,469 (±2%)	19.50 (±7%)	25 (±48%)

Table 2: Results of the calibration of the Passive LINUS, for the three different CR39 plastics used. Uncertainties in brackets refer to one sigma statistical uncertainties.

All CR39 plastics show a higher sensitivity compared to the performance of the detector described by *Caresana et al.* [64] by more than a factor 4, but also a higher intrinsic noise.

Since the RTP Batch 1 shows the lowest sensitivity and not the best signal-to-noise ratio, this will not be considered in further experiments. The RTP Batch 2 shows the highest sensitivity of the three analyzed plastics, but also a rather poor signal-to-noise ratio compared to the other two plastics. Intercast, on the other hand, shows a sensitivity comparable to that of RTP Batch 2, the best of the three, but also factor 6 higher signal-to-noise ratio. Hence, as a result of the Passive LINUS calibration, Intercast CR39 plastics with their high sensitivity (18.70 $\mu Sv^{-1}cm^{-2}$) and highest signal-to-noise ratio were chosen for further experimental activities.

5.2 Monte Carlo simulations of the LION facility

As already mentioned, a Geant4 Monte Carlo study has been performed for the LION experiment. This experiment is driven by ATLAS3000, a Ti:Sapphire-based laser system that will be able, once at full power, to deliver to LION laser pulses with an energy of ≈ 60 J, a pulse duration ≈ 20 fs at a repetition frequency of 1 Hz [83]. LION's goal is to

study the TNSA and RPA acceleration regimes towards the creation of an ion source for radiation therapy research [83]. Currently (October 2021) ATLAS3000 is not yet fully operational. The maximum energy delivered to LION when this thesis was performed was about 10 J with a pulse duration of about 30 fs and reduced repetition frequency (shot on demand).

Geant4 Monte Carlo simulations including realistic dimensions and material compositions of most relevant components hosted inside the LION cave and LION vacuum chamber have been conducted in order to quantify the secondary neutron fields produced at this facility. For this, three scenarios were assumed where different proton and electron spectra (each representative of a different step of LION commissioning) were used as source terms. This work has been thoroughly described in a dedicated peer-reviewed publication [84] and will be summarized in the following.

Additionally, physics lists, geometry and materials used for the Geant4 LION simulations have been tested against FLUKA by performing dedicated test simulations. The result of this activity was that the average discrepancy in the neutron fluence calculated by the two different codes was less than 20% (see Appendix D for details).

5.2.1 Geometry and materials

The particle acceleration in the LION experiment takes place within a 2.5 cm thick aluminum vacuum chamber (having a modular structure and being 3.92 m long, 0.98 m wide and 1.21 m high) which is hosted inside an experimental cave 18 m long, 3 m wide and 4.25 m high. This latter is then surrounded by shielding walls whose thickness ranges from 1 to 1.2 m. These walls separate the LION cave from the surrounding areas for radiation protection purposes (Figure 16a). Also for radiation protection purposes a massive water-concrete composite beam dump was placed at about 50 cm from the front face of the LION vacuum chamber, as result of dedicated radiation protection simulations that had been performed with FLUKA during the construction of the facility [85]. The main purpose of the beam dump is to stop that fraction of accelerated particles that leaves the vacuum chamber.

Inside the LION vacuum chamber several components are required to produce and deliver laser-driven protons with desired features. It has been decided that it is sufficient to consider in the simulations only those elements that interact directly with the primary particles, reducing design and simulation times, yet deriving realistic results. As it is shown in Figure 16b, these elements include two quadrupole magnets (referred to as

QPs in the following) and a glass-made photon screen used for laser light diagnostics (blue).

The two QPs are made of a particular NdFeB alloy and were modeled as parallelepipeds 6.5 x 6.5 x 5 cm^3 with a circular opening 1 cm in diameter oriented along the z axis. The first QP is positioned at 4.7 cm from the laser-target (i.e., location of the proton source) and the second one at 7.9 cm. The photon screen consisted of two 1 cm thick glass slabs, separated by a few centimeters gap (Figure 16b) and positioned at about 67 cm from the location of the proton source.

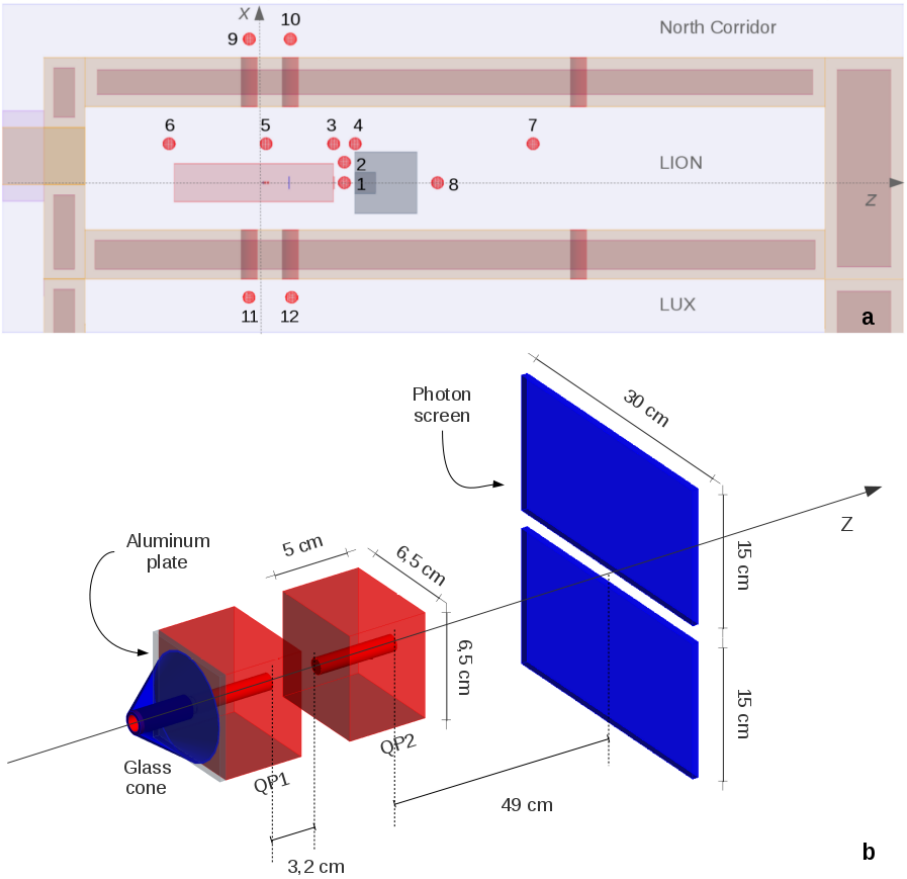

Figure 16: Geant4 geometry of the LION cave (**a**), and geometry of the most relevant components hosted inside the vacuum chamber (**b**). Red spheres in Subfigure **a** refer are neutron scorers (with their respective ID number), the light gray square is the concrete beam dump with its water insert (in dark gray), while the vacuum chamber is depicted as a light red rectangle. The two parallelepipeds in Subfigure b are the two qadrupoles (QPs) with the glass cone mounted on the fron face of the first QP (in blue). Behind the second quadrupole is the photon screen (blue rectangles).

The front face of the first QP is shielded by a 4 mm thick aluminum protection plate (density = 2.7 g/cm^3) to shield from potential radiation damage. A borosilicate glass-made hollow cone is additionally mounted on the front face of the aluminum protection plate. It serves the purpose of avoiding possible laser light back-reflections from the aluminum plate surface.

Eight spherical neutron and photon fluence scorers (1 – 8), defined as described in subchapter 4.4, have been placed throughout the LION experimental cave at y = 0, in order to derive a complete neutron fluence mapping inside the LION hall. In addition, four scorers were added for radiation protection considerations outside the shielding at specific weak spots of the shielding (9 – 12). All scorers are depicted in Figure 16a as red spheres with their respective ID number.

5.2.2 Primary particle energy spectrum and angular divergence

5.2.2.1 Protons

In order to simulate current and future radiation scenarios, three proton spectra taken from experimental data published in the literature (and representative of three specific commissioning phases of the LION experiment) were used as proton source terms:

- Zeil2010 [86]: Proton spectrum already available experimentally (commissioning phase 1, 300 TW)
- Ma2019 [87]: Proton spectrum reachable within a couple years (feasible with 1 PW)
- Wagner2016 [7]: Proton spectrum reachable within three to five years (feasible with 3 PW and loose focus, i.e., not optimized for highest maximum energy)

Numerical values of the proton spectra were taken from [88] where they are reported as number of protons per unit energy and unit solid angle. Each value represents the number of protons of energy E in a $1\%E$-wide energy bin centered around energy E, per millisteradian (msr).

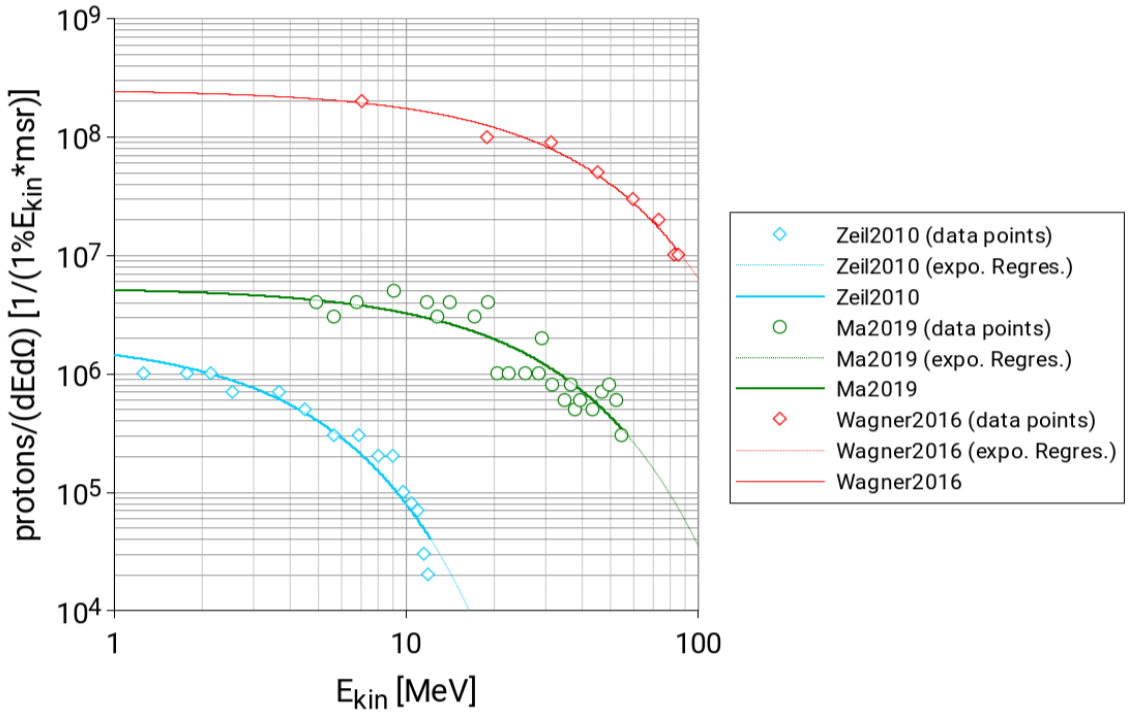

Figure 17: Primary proton spectrum data as reported by *J. Schreiber* in [88] with exponential regression applied (dashed lines). Solid curves show the proton spectra found truncating the exponential regression at the respective proton cutoff energy. Figure adapted from [84].

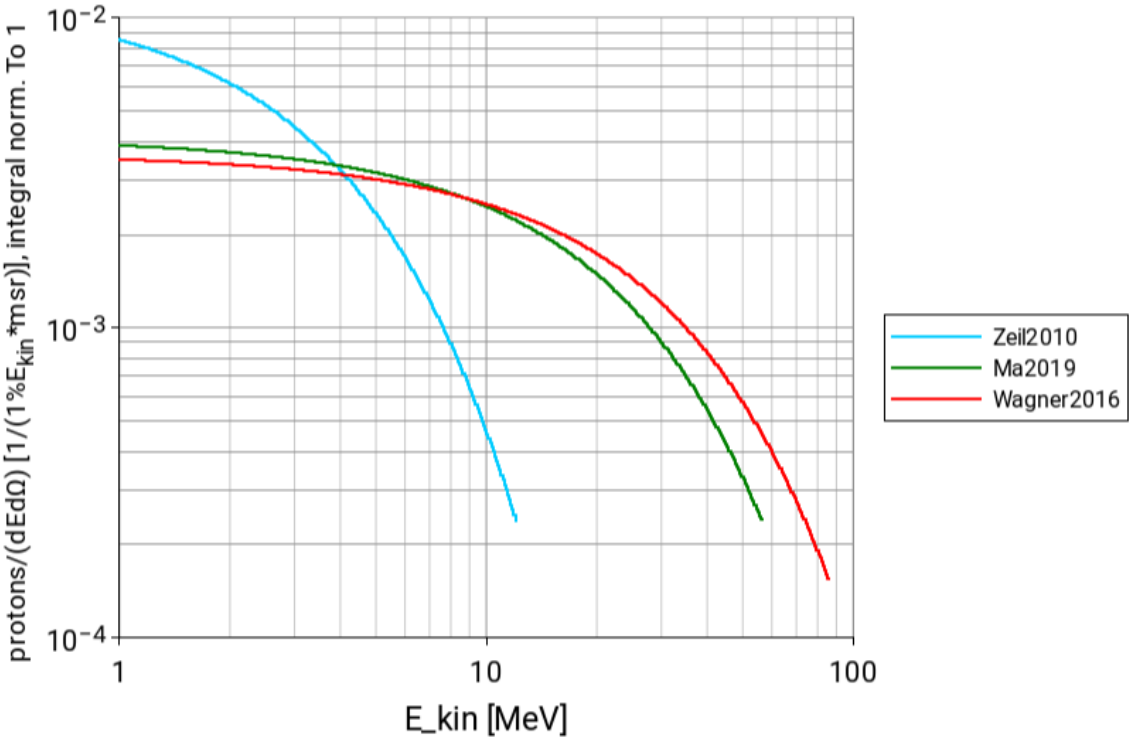

Figure 18: Proton spectra (normalized to integral = 1) used as input source terms for the simulations of the secondary neutron spectra at the LION experiment. Figure adapted from [84].

An exponential regression was applied to the experimental data. The resulting regression curves were then sampled to create a discrete spectrum that covers energies from 1MeV to the cut-off energy $E_{p.cutoff}$, for each dataset. Each bin i was centered at energy E_i and had a width of $1\%E_i$, for a total of 250 bins for *Zeil2010*, 404 bins for *Ma2019*, and 445 bins for *Wagner2016*.

The experimental proton spectra as given in [88] are plotted in Figure 17, together with their exponential regression. Figure 18 shows the relative primary proton spectra (the value of each bin i is the probability of having a proton with energy E_i). These were used in the following as input parameters.

5.2.2.2 Electrons

As mentioned earlier, together with protons also electrons are emitted through laser-target interaction. So far, no experimental results have been published reporting the spectrum or charge per bunch of electrons at laser-driven proton sources.

It has been therefore decided, within this work, to use an exponentially shaped electron source, as first order approximation. Equation (7) gives the number of electrons, N_{e-} , with energy E:

$$N_{e-}(E) = \frac{N_{e-,0}}{E_{e-,0}} e^{-E/E_{e-,0}} \quad (7)$$

Where $E_{e-,0}$, also referred to as *electron temperature*, can be derived from equation (8) [89]:

$$E_{p,cutoff} = (4.6E_{e-,0} \pm 287)\, keV \quad (8)$$

Where $E_{p,cutoff}$ is the measured cut off energy of the corresponding proton spectrum. Proton cut-off energies for each of the three investigated proton spectra and the corresponding electron temperatures are summarized in Table 3.

Proton Spectrum	$E_{p,cutoff}$	$E_{e-,0}$
Zeil2010	11.92 MeV	2.59 MeV
Ma2019	56.05 MeV	11.96 MeV
Wagner2016	85.93 MeV	18.68 MeV

Table 3: Proton cutoff energies, $E_{p,cutoff}$, and corresponding electron temperatures, $E_{e-,0}$, for the three spectra considered in this study.

The total number of electrons was assumed to equal the number of simulated protons, in order to reproduce the quasi-neutrality of the plasma condition.

$$N_{e-,tot} = N_{p,tot} \quad (9)$$

Electron distributions were implemented as probability step curves from 1 to 100 MeV, with 1 MeV wide bins (Figure 19).

5.2.2.3 Angular distribution

Particles produced via laser-target interaction are usually characterized by a large divergence angle whose value can range from a minimum of zero to a maximum of a few hundred mrad [90]. At a few centimeters distance from the laser-target position, two QPs were used to focus the diverging protons and form a proton bunch. Since the acceptance

angle of the QPs is lower than the initial divergence of the protons, it is taken as assumption that 90% of protons collide with the front face of the first QP and only 10% of protons pass through the QPs [91]. Although protons with low energy tend to be more divergent compared to protons with high energy (which in contrast are more forward peaked) [13], as a first order approximation this feature was neglected. Therefore, it was assumed that the spectrum of particles does not vary over the emission angle.

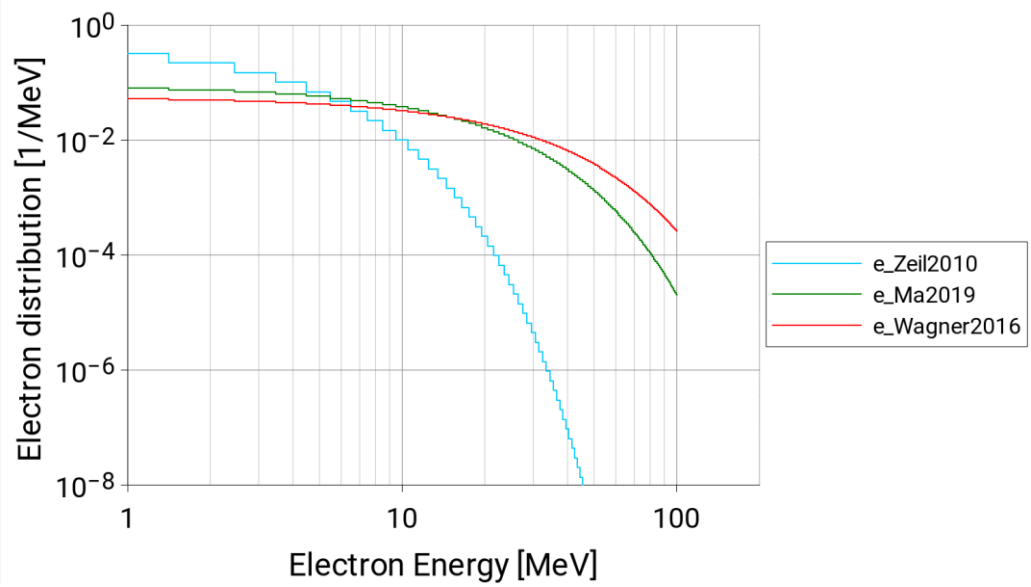

Figure 19: Histograms of the electron spectra derived by applying equation (7). Figure adapted from [84].

To account for the focusing action of the QPs, yet avoiding the simulation of magnetic fields, the proton source term was separated in two components: A focused fraction (F-fraction) and a divergent fraction (D-fraction). The F-Fraction, to which 10% of total simulated primary particles belong to, was assumed to be emitted as a pencil beam that passes through the two quadrupoles without any interaction. In contrast, the D-fraction represents all other emitted particles that interact with the front face of the first QP (90% of the total). Its diverging angle goes from θ_{min} and θ_{max} where, θ_{min} is the smallest angle at which protons still interact with the front face of the first QP and θ_{max} equals 180 mrad (Figure 20).

Monte Carlo simulations were run for the two components separately, afterwards the results were linearly superimposed with the specified proportions (90% vs. 10%).

Together with protons, also electrons are accelerated, and part of them are accidentally focused by the focusing system. For this reason, a similar two-components source term was used to model electrons. Given the lack of knowledge on the electron source term,

it was assumed that 90% of electrons belong to the D-fraction and 10% belong to the F-fraction, and maximum electron divergence equals the maximum proton divergence of 180 mrad, in analogy with the assumed proton source term.

Finally, it should be added that also a minor fraction of protons is emitted in backward direction. This component shows typically lower cutoff energies (around a factor 2) and also a lower charge per bunch compared to forward-emitted protons [92]. Following these considerations, backward-emitted protons were excluded from the simulations.

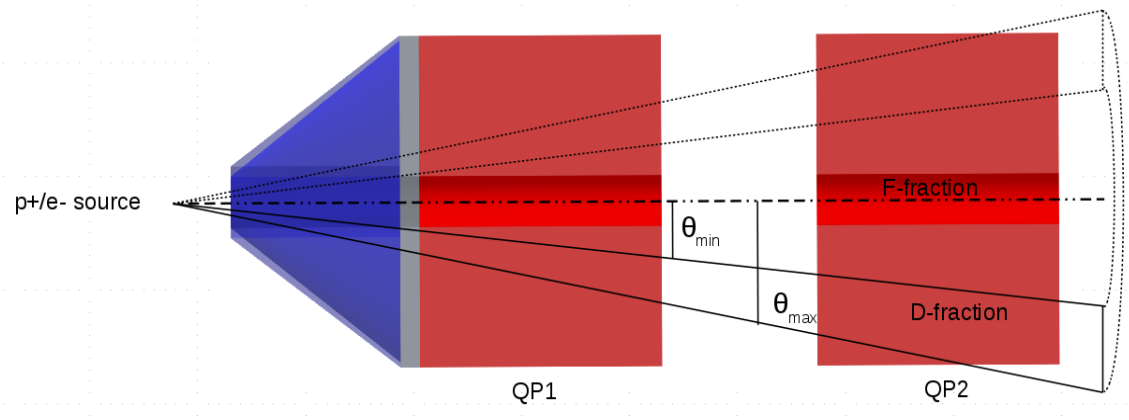

Figure 20: Lateral view of the two quadrupoles (QPs) with geometry of the particle source term. The F-fraction is emitted as a pencil beam while the D-fraction is emitted with a diverging angle ranging from θ_{min} to θ_{max}. Figure from [84].

5.2.3 Results

Simulation results are given as neutron spectra for each primary source term. Neutron spectra were normalized in terms of primaries per bunch, deriving the number of protons per bunch as described in Appendix E.

Common and already well-described features of the neutron spectra expected at LION can be derived by looking at secondary neutron spectra measured at proton and electron accelerator facilities. Generally, in the proximity of proton and electron accelerators one can identify some typical and distinctive neutron spectrum features [18,19]. These are, starting from low energies:

- a Maxwell-Boltzmann peak centered at thermal energies when plotted in the lethargy representation (thermal neutrons)
- a *plateau* in the epi-thermal region ($E_{th} < E_n < 100\ keV$) (epi-thermal neutrons)
- a peak around 1-2 MeV generated by nuclear evaporation processes of the nuclei involved in the reaction (evaporation neutrons).

- a high-energy neutron component whose energy is similar to the primary proton maximum energy, in case primary particles above 20 MeV are present (high-energy neutrons).

5.2.3.1 Zeil2010 p^+ and e^- sources

Among the primary source terms considered in this work, Zeil2010 proton and electron source terms were the ones with steepest energy-dependent particle spectrum and lowest cutoff energy, as visible in Figure 18 and Figure 19.

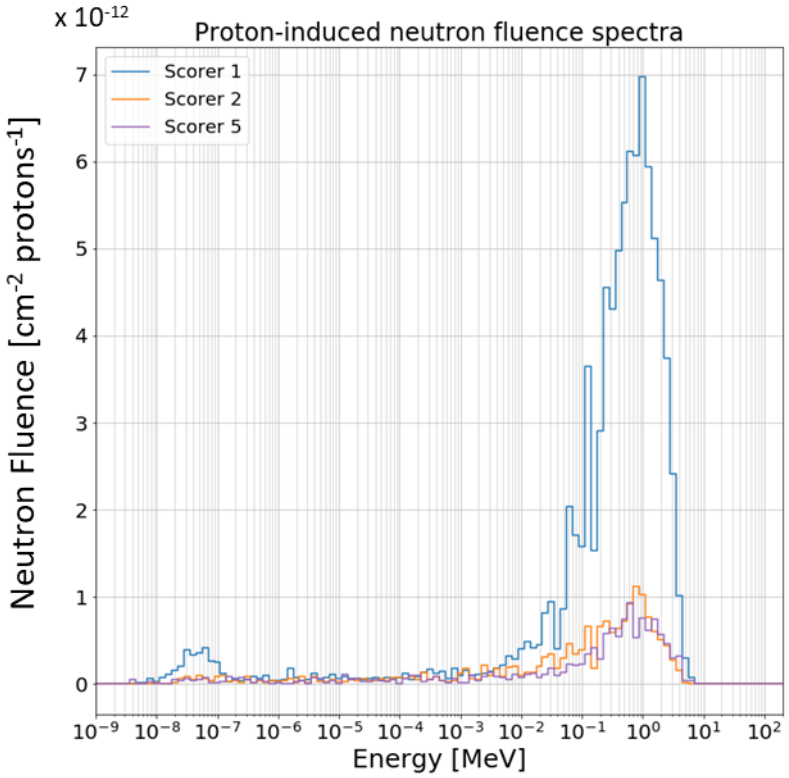

Figure 21: Proton-induced neutron fluence spectra for scorers 1, 2 and 5 (see Figure 16) using the Zeil2010 input spectrum. Values are normalized to one primary proton. Figure adapted from [84].

The total neutron fluence per bunch in all scorers inside the LION cave were below 10^{-10} and 10^{-11} $cm^{-2}protons^{-1}$ for primary protons and electrons, respectively. Because of statistical reasons, only the spectra of those scorers whose total fluence exceeded $5 \cdot 10^{-11}$ $cm^{-2}protons^{-1}$ have been plotted in Figure 21 (namely, scorers 1, 2 and 5 for the proton source case). The neutron evaporation peak is well-recognizable for all three scorers while the thermal neutron peak appears visible only for scorer 1. The thermal peak is missing for scorers 2 and 5, only due its low intensity.

5.2.3.2 Ma2019 p^+ and e^- sources

Figure 22 shows neutron spectra for all scorers inside the LION cave using the Ma2019 proton- and electron source terms. The main feature of all spectra is a well-defined evaporation peak (centered at around 1 MeV) visible for both for proton and electron source terms. Clearly visible on the left edge of the evaporation peak (from a few keV to hundreds of keV) is a pattern of spikes, whose presence is independent from whether neutrons are produced by proton- or electron-induced reactions. Their presence is attributed to the particular shape of the neutron absorption cross section of most materials that, in this specific energy region, shows resonances. Clearly visible are the 35, 90 and 140 keV neutron elastic resonances of ^{27}Al and the 430 keV elastic resonance of ^{16}O. Considering the proton-induced neutron spectra (Figure 22a), specially for scorer 1 (and partly also for scorers 2, 3 and 4) one can see a slightly visible high-energy neutron component, more in the form of a shoulder rather than a separate peak. This component is the result of the interaction of high energy protons with the QPs and the air.

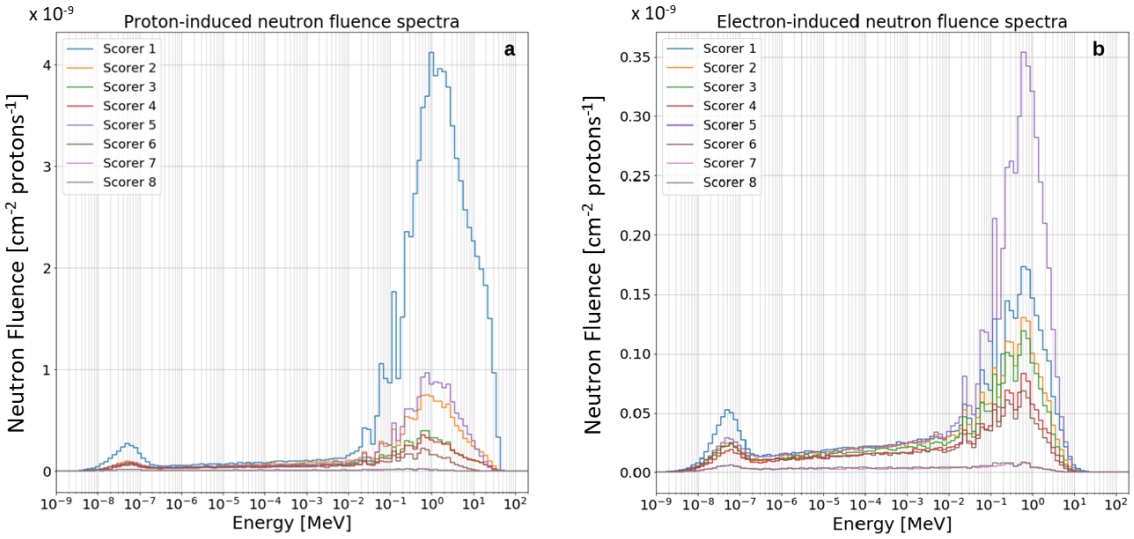

Figure 22: Proton- (**a**) and electron-induced (**b**) neutron fluence spectra for all scorers inside the LION cave (see Figure 16) using Ma2019 primary protons and electrons, respectively. Values are normalized to one primary particle. Figure adapted from [84].

Focusing on the electron-induced neutron spectra (Figure 22b), it is clearly visible that the highest neutron fluence is detected by scorer 5 rather than by scorer 1. This can be explained considering that in this case, neutrons are produced via photonuclear reactions of bremsstrahlung photons produced by the primary electrons, and, since the QPs are composed by elements with a higher Z number compared to the beam dump, more photo-neutrons are produced in the QPs, than in the beam dump. Due to its vicinity to

the QPs, scorer 5 then detects more neutrons than scorer 1, when using the electron source term.

5.2.3.3 Wagner2016 p^+ and e^- sources

Wagner2016 proton and electron source terms yield, as expected, the highest secondary neutron fluences per bunch compared Ma2019 and Zeil2010 primary spectra. Values up to $2.5 \cdot 10^{-7}$ $cm^{-2}protons^{-1}$ can be found in scorer 1 using the proton source term. Similar considerations as for Ma2019 can also be made for the secondary neutron spectra induced by the Wagner2016 source terms.

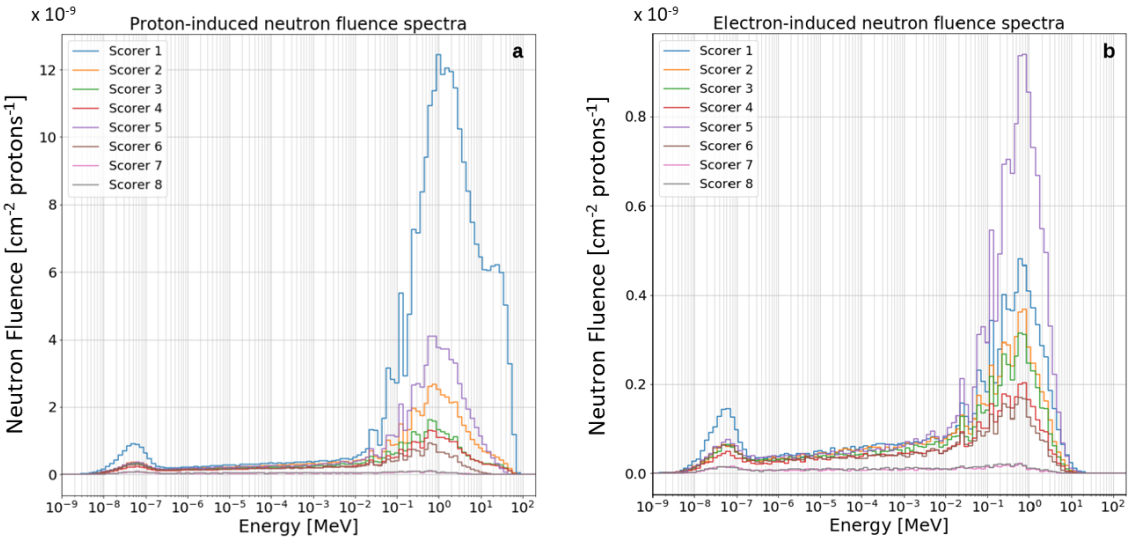

Figure 23: Proton- (**a**) and electron-induced (**b**) neutron fluence spectra for all scorers inside the LION cave (see Figure 16) using Wagner2016 primary protons and electrons, respectively. Values are normalized to one primary particle. Figure adapted from [84].

The most visible difference (apart from the absolute magnitude) is the presence, especially for scorer 1 of a pronounced high-energy neutron peak (see Figure 23). In additional simulations it was found that this peak can be attributed to high-energy protons interacting with air. The high-energy peak turns into a high-energy shoulder in other scored positions because of geometrical reasons. As already discussed with Ma2019, the highest neutron fluence produced by electrons is detected by scorer 5.

5.3 Feasibility study on the LION facility

This feasibility study aimed at evaluating the possibility of applying a specific detection technique to perform neutron measurements at the LION laser-driven accelerator facility,

at a given commissioning phase. Starting from the simulated neutron fluence spectra presented in the previous sub-chapter 5.2, neutron doses per primary particle were calculated by folding with the fluence-to-dose conversion curve. Total neutron doses per bunch were then derived for each primary source term by multiplying the neutron dose per primary proton by the expected number of primary protons per bunch, as calculated in Appendix E (Table 9). Analogously, the expected number of counts or activity per proton bunch was derived by folding each neutron spectrum with the energy-dependent response function of each detection technique. Constraints on the expected number of bunches per experimental campaign were also taken into account to evaluate the feasibility of integrated measurements over more than one laser shot at LION.

5.3.1 REM Counters

The key parameter to look at when deciding of employing a neutron REM counter to perform measurements in pulsed neutron fields is the expected D_{bunch} (see Figure 4). As discussed in Chapter 3, conventional neutron REM counters, as the NM2B-458 or the NM2B-495Pb used at the Institute of Radiation Medicine, show underestimation of the real dose per bunch at already a few nSv/bunch. *Caresana et al.* performed an intercomparison study in pulsed neutron fields at a proton facility hosted at the Helmholtz-Zentrum Berlin, Germany, where several neutron REM counters were exposed to different neutron doses per bunch in order to reconstruct their response curve in pulsed neutron fields [58]. This work shows that, on the average, most commercially available neutron REM counters start losing linearity in pulsed neutron fields at about 10 nSv/bunch. This value can be taken as indicative highest constraint on the maximum neutron dose per bunch for which a conventional REM counter (as the NM2B-458 and NM2B-495Pb) can still be safely used.

In the same study also the behavior of the LUPIN-II in pulsed neutron fields was investigated. This detector, developed for pulsed radiation fields, showed a linear behavior up to about 500 nSv/bunch, allowing measurements in more challenging radiation environments.

Figure 24 shows the total (proton- and electron-induced) neutron dose per bunch for all scorers inside the LION cave, derived by folding each simulated neutron spectrum with the fluence-to-dose conversion curve and by multiplying by the calculated total number of protons per bunch.

Figure 24 demonstrates that neutron doses per bunch vary by several orders of magnitude depending on the primary proton spectrum and position of the scorer: when using

Zeil2010 the simulated secondary neutron dose ranges from 0.01 to 1 nSv/bunch, when using Ma2019 it ranges from 10 nSv/bunch to 3 uSv/bunch, while for Wagner2016 the secondary neutron dose per bunch varies from 4 uSv/bunch to 1 mSv bunch.

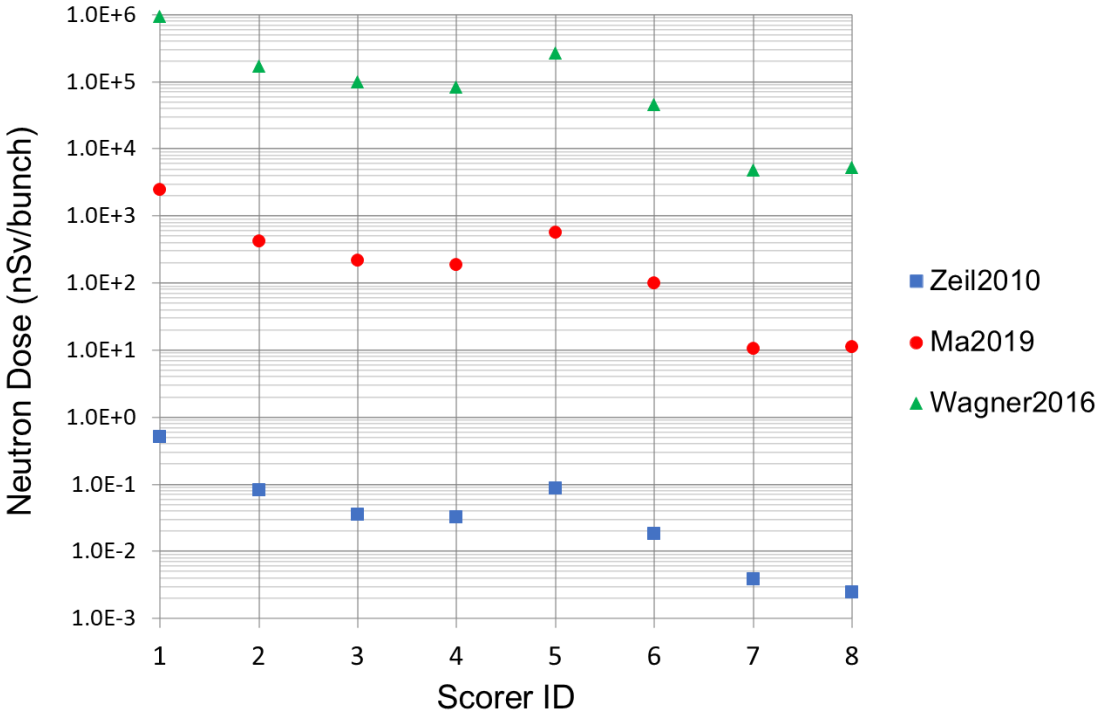

Figure 24: Simulated secondary neutron doses at the laser-driven ion source facility, LION. For scorer IDs see Figure 16.

Figure 24 clearly suggests that *any* active REM counter (both the NM2B series detectors and the LUPIN-II) could in principle be used to perform secondary neutron dose measurements when LION produces proton bunches with primary source spectra similar to Zeil2010, by considering that the expected maximum dose per bunch is below 1 nSv/bunch. In this condition, the neutron field, although pulsed, is not of concern for these devices due to the low dose delivered in one bunch. However, the problem is that, for such low doses per bunch, the probability of detecting neutrons on a single bunch level is very low and, consequently, the investigated active REM counters are not reliable for single bunch detection. This hinders the most attracting capability of active detectors, which is performing single-bunch measurements. In addition, if one considers scorer 5, a good candidate for an experimental analysis because it was on the side of the vacuum chamber and therefore not in the direction of the primary particles, one sees that only about 0.1 nSv/bunch are expected. If one multiplies this value by a realistic number of laser pulses per measurement day (about 100) one ends up with about 10 nSv total

neutron dose in a measurement day. Such a neutron dose is very low to be measured for REM counters (whose sensitivity, as mentioned, is in the order of 1 count/nSv), resulting in a statistical uncertainty of more than 30%, which, combined with the typical intrinsic uncertainty of the energy response of the detector (about 20%), would give a measured neutron dose with an uncertainty of about 40%. Such an uncertainty would make any reasonable conclusions on the actual total neutron dose produced difficult.

In contrast, the pulsed nature of the neutron field becomes relevant when looking at the results derived by using Ma2019 primary proton spectrum: except for scorers 7 and 8 (which were placed behind the beam dump and, therefore, were heavily shielded), the expected neutron dose per bunch is of the order of the several hundreds of nSv/bunch (up to more than about 1 µSv/bunch for scorer 1). In such an environment only the LUPIN-II will be able to correctly perform a neutron dose measurement, while conventional REM counters would heavily suffer of dose underestimations. In addition, if one considers that the LUPIN-II has a sensitivity of about 2.16 cts/nSv, one derives statistical uncertainties lower than 3% already at 50 nSv/bunch. This means that when spectra similar to Ma2019 will become available, even single-bunch measurements could be performed with the LUPIN-II with a rather low statistical uncertainty.

Considering the Wagner2016 proton spectrum, the most intense primary proton spectrum used in this study, the simulated neutron dose per bunch exceeds the limits of both types of active neutron REM counters considered in this work. In this case it will be thus necessary to rely on passive detection techniques for neutron dose measurements.

5.3.2 The Passive LINUS

The calibration experiment described in Subchapter 5.1 suggested that the Passive LINUS including a novel thermal neutron detector and Intercast CR39 has a sensitivity of 18.70 (±7%) $\mu Sv^{-1}cm^{-2}$ and an intrinsic noise due to plastic imperfections of 28 (25%) cm^{-2}. This means that the minimum detectable dose above the background is in the order of 1-2 µSv. A direct consequence of this is that for a Zeil2010-like source spectrum, secondary neutron dose measurements are practically impossible to be performed at LION at any of the simulated positions, even considering a measurement over the total dose integrated over one experimental day including 100 laser pulses. To give an idea, to get measurable values in the order of about 5 µSv for scorer 5, at least $6 \cdot 10^4$ bunches are needed when using Zeil2010-like spectra, a number of bunches way beyond the current LION capabilities and that would require almost 17 hours of continuous operation at the maximum design repetition frequency of 1 Hz.

On the other hand, if one looks at single-bunch doses in the proximity of the vacuum chamber (scorers 1 to 6) simulated using the Wagner2016 source then doses from 10 to 800 µSv/bunch are expected depending on scorer position. CR39-based passive REM counters coupled with ^{10}B-enriched converters typically exhibit linear responses for doses up to a few mSv, the exact value being dependent on both converter design and track analysis algorithm used. Concerning the instrument used along this thesis, this limit is estimated to be around 9 mSv, according to statistical considerations on the track density derived from [93,94].

Hence, in case Wagner2016 source spectra will become available, one can safely assume that the Passive LINUS would be able to measure single-bunch neutron doses.

A bit more complex is the situation in between these two cases, represented by the Ma2019 primary proton spectrum. Here, close to the vacuum chamber (scorers 1 to 6) neutron doses per bunch from 0.1 to 3 µSv/bunch are expected. Such values are close to the detection limit of the detector and, therefore, tracks produced by such low doses per bunch are either hidden in the background or difficult to be identified. However, if one assumes experimental campaigns including about 100 bunches with Ma2019-like spectra, total doses of about 10 to 300 µSv can be expected, depending on the experimental position. Therefore, when source spectra like Ma2019 are produced, the Passive LINUS cannot provide single-bunch measurements, as for the Wagner2016-like case, but it will allow surveying the total neutron dose produced over an experimental day including about 100 laser pulses.

5.3.3 Au-BSS

To study the feasibility of applying the Au-BSS to perform passive secondary neutron spectrometry, the response function of the Au-BSS was folded with the neutron fluence spectra simulated for each scored position and for each primary source term, and then multiplied by the total number of primaries per bunch. This resulted in the number of ^{198}Au atoms produced per bunch, N. The induced activity, A, was then simply calculated by multiplying the produced number of ^{198}Au atoms by the decay constant of ^{198}Au, λ:

$$A = \lambda N \tag{10}$$

A, therefore, represents the activity of the gold sample right after being exposed to a neutron bunch. The limiting factor of this technique, as previously mentioned, is the minimum detectable activity. For the bore hole Ge spectrometer used in this study the MDA

was $MDA_{BH} = 5 \cdot 10^{-3} Bq$ (as shown in Appendix A). Therefore, activity values below the MDA ($A < MDA_{BH}$) cannot be discriminated from the background noise.

5.3.3.1 Zeil2010 source term

Figure 25 shows the calculated activity for each sphere of the Au-BSS and scorer position when using the Zeil2010 primary source spectrum. Results for different scored position are plotted with different colors. The maximum induced activity per bunch was found to be about $2 \cdot 10^{-7}$ Bq/bunch, for scorer 1 and the 6" sphere. This value is about $2.5 \cdot 10^{4}$ times lower than the MDA. This result clearly shows that even accumulating the activity over a whole measurement day (assuming about 100 laser shots per day) would not induce enough activation reactions to get measurable activity. Similarly to the Passive LINUS, Au-BSS cannot be applied if Zeil2010-like spectra are produced, because of its poor sensitivity.

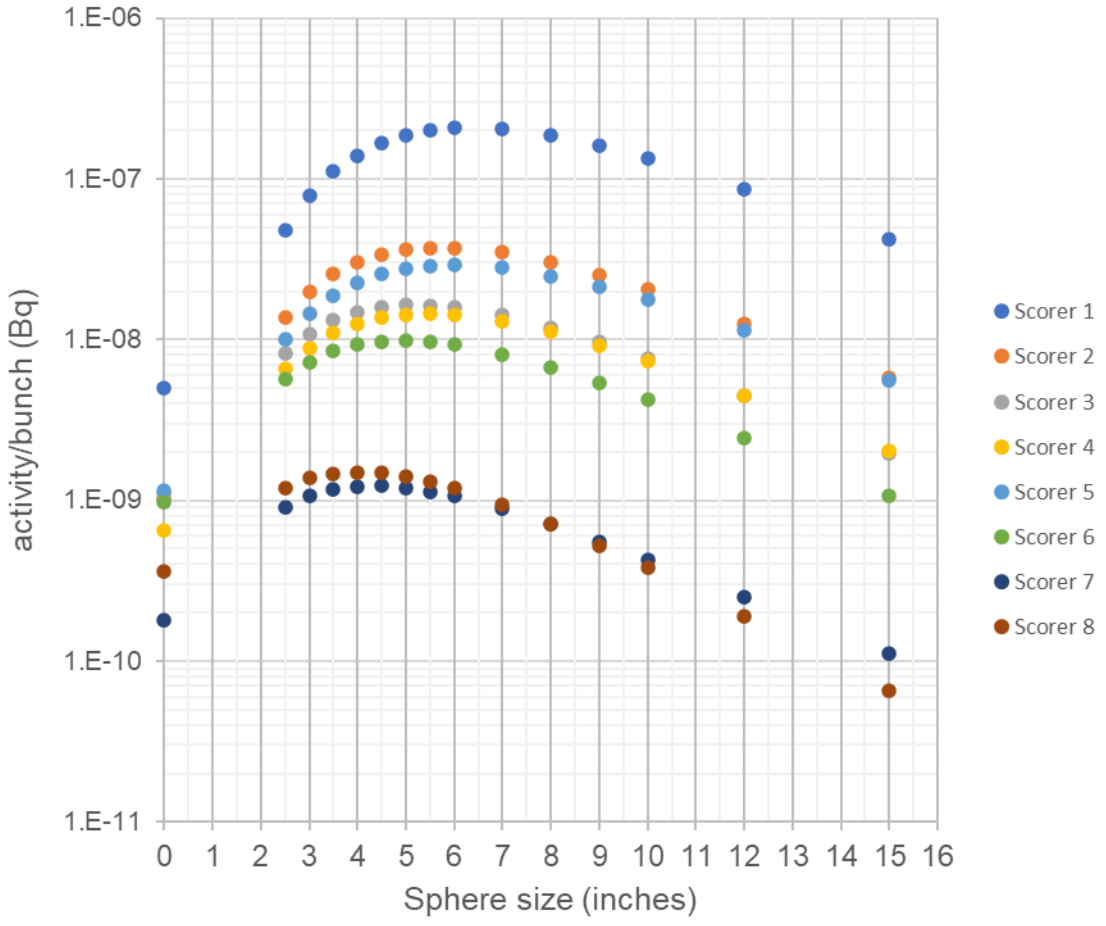

Figure 25: Calculated activity vectors for each neutron scorer (1-8) (see Figure 16) using the Zeil2010 primary spectrum. Results are given in Bq per bunch of primary particles.

5.3.3.2 Ma2019 source term

When spectra like Ma2019 are produced, higher activity per bunch is expected. Figure 26 shows the calculated activity for each sphere of the Au-BSS and scorer position when using the Ma2019 primary spectrum. As can be seen, single bunch activation measurements cannot be performed in any of the scored positions: maximum single bunch activity was found to be less than 10^{-3} Bq/bunch, for scorer 1 and the 7" sphere. Note that scorer 1 is directly in the way of the primary particles and it is therefore not a suitable experimental position. For scorer 5, (light blue data points in Figure 26), if one plans to do neutron spectrometry and if one knows the features of the expected neutron spectrum, one needs at least 6-7 spheres of different size, including the bare detector. For instance, one could think of using spheres 4" and 5" that have a rather flat spectrum from thermal energies to the MeV region to help the unfolding code to estimate the total fluence, spheres 5.5", 6" and 7" to well estimate the evaporation peak (main peak of the spectrum), sphere 12" to estimate the higher energy part of the spectrum and the bare detector to well characterize the thermal peak. Then the total required number of equal bunches needed to reach activity values above the MDA_{BH} in all mentioned spheres is of the order of 1,000. This is mainly due to the fact that the bare detector needs about 800 bunches to overcome the MDA_{BH}. This value needs to be doubled, considering that also a set of measurements with Cd cladding is needed as described in Subchapter 3.3.2.2.

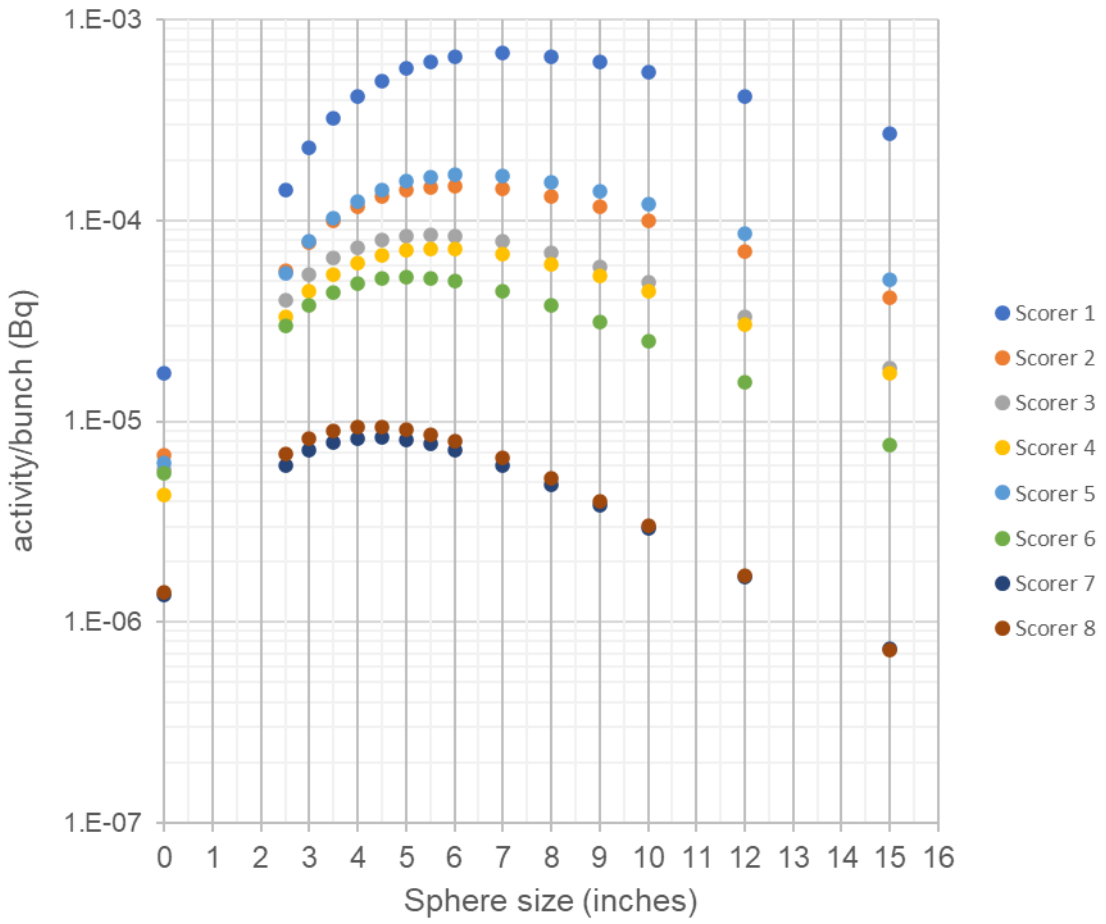

Figure 26: Calculated activity vectors for each neutron scorer (1-8) (see Figure 16) using the Ma2019 primary spectrum. Results are given in Bq per bunch of primary particles.

This hypothetical experiment demonstrates that if "only" Ma2019-like spectra are available, a few thousand equal bunches will be needed to perform neutron spectrometry with the Au-BSS at one experimental position. It needs also to be mentioned that no saturation was considered for this simple analysis, therefore assuming that the irradiation time is $\ll \tau_{1/2}$ ($\tau_{1/2}$ being the half-life of ^{198}Au, 2.697 days). A higher number of bunches would be necessarily required if this condition were not satisfied.

5.3.3.3 Wagner2016 source term

Similarly to what was done for the Zeil2010 and Ma2019 primary sources, Figure 27 shows the calculated activity vectors for all scorers when using the Wagner2016 primary source term.

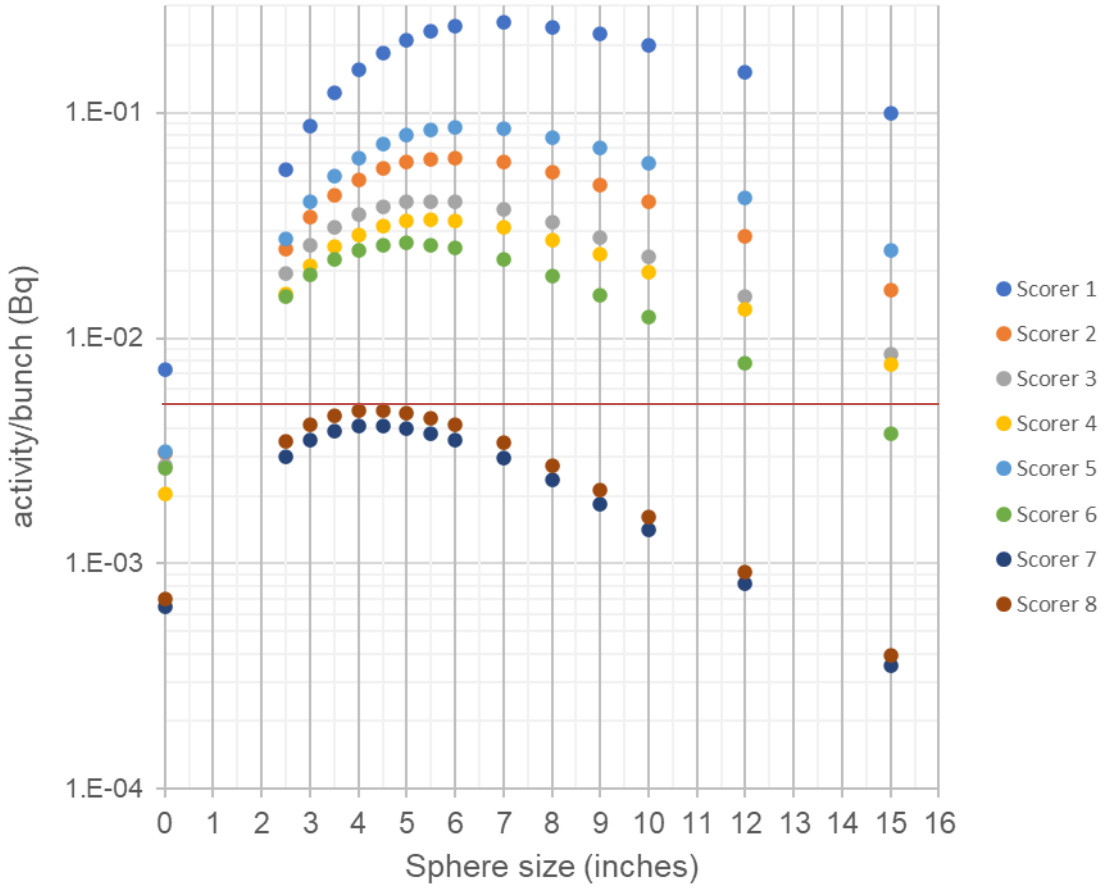

Figure 27: Calculated activity vectors for each neutron scorer (1-8) (see Figure 16) using Wagner2016 primary spectrum. Results are given in Bq per bunch of primary particles. Horizontal red line: minimum detectable activity. For details see text.

Due to the higher intensity and maximum proton energy of the Wagner2016 source term, higher activity values are expected, compared to the previous two cases. activity values above the MDA_{BH} (represented by a red line in Figure 27) is found for all spheres, including the bare detector in position 1 but excluding the bare detector for scorers 2 – 5 (for scorer 6 also the 15" sphere shows an activity lower than the MDA_{BH}). If one would repeat the hypothetical neutron spectrometry experiment proposed for the Ma2019 spectrum (using five spheres plus bare detector at position 5), in this case one bunch for each sphere would be enough to get a measurable activity in all spheres and two bunches for the bare detector. Considering also that a second set of measurements with Cd cladding is necessary, this results in a total of about 20 laser shots. In this case, when Wagner2016 spectra will be available, the Au-BSS appears as a viable option for neutron spectrometry measurements.

In addition, it should to be mentioned that for proton spectra like Wagner2016, an Extended Range Bonner Sphere Spectrometer (ERBSS) would be more suitable to perform measurements than a conventional BSS, given the presence of a non-negligible fraction of neutrons above 10 MeV. For instance, at positions 2, 3 and 4, 5-10% of the fluence is due to neutrons with an energy above 10 MeV. An extension of the current Au-BSS to an Au-ERBSS should therefore be taken into account when considering applications in such secondary neutron fields.

5.3.4 Conclusions from the feasibility analysis

The outcome of the feasibility study is that, for low intensity primary proton spectra (such as Zeil2010) the pulsed nature of the source is not a relevant concern even for conventional neutron REM counters. In this case, the real issue is the usually low repetition frequency of laser-driven proton sources or the total number of laser pulses realistically achievable in a measurement campaign. Thus, the first result is that none of the four different detection techniques considered in this work is suitable to perform measurements when Zeil2010-like spectra are produced.

In the intermediate regime (production of spectra like Ma2019), the LUPIN-II appears to be the best choice, providing, together with integrated doses over several bunches, also single bunch neutron doses with low uncertainty. In contrast, conventional REM counters are expected to saturate because of the intensity of the pulsed radiation. In this case, CR39-based REM counters, such as the Passive LINUS, should offer the possibility to perform integrated neutron dose measurements at specific positions, provided that at least a few dozens of bunches are produced.

For high-intensity primary proton spectra (Wagner2016) the field intensity is too high for any active neutron REM counter and, consequently only the Passive LINUS, of the REM counters considered in this study, can be employed to perform secondary neutron dose measurements. In this case also single bunch measurements can be performed.

Concerning neutron spectrometry measurements, the performance of a gold foil Bonner spheres spectrometer was studied. It was estimated that at least a couple of thousands equal bunches are needed to perform neutron spectrometry if Ma2019-like spectra are available. In contrast, if Wagner2016 spectra are available, only 20 equal bunches are needed for the same experiment. The outcome of these considerations is that neutron spectrometry with an Au-BSS can be performed only with the most intense available laser-driven proton sources.

During the time this study was carried out Zeil2010-like proton spectra with about 100-150 shots per measurement day were feasible at LION. In these conditions, the present study showed that measurements with the neutron detectors available could not be performed, due to the low total neutron fluence produced. Possible measurements could be performed, however, at facilities where either a much higher number of laser pulses (in the order of a few thousands) per measurement campaign are achievable, or where higher proton cut-off energies (Ma2019-like spectra) are available.

6. The DRACO experimental campaign

6.1 Introduction

DRACO (Dresden laser acceleration source) is a Ti:Sapphire PW-class laser system installed at the ELBE center for high power radiation sources of the Helmholtz-Zentrum Dresden-Rossendorf, Germany (Figure 28). Initially, a 150 TW laser system was installed, based on the Pulsar design of Amplitude Technologies (France). First proton acceleration experiments with this laser system were carried out in 2009 and published by *Zeil et al.* [86]. Less than a decade after the first experimental activities, this laser system was upgraded to the current DRACO PW laser that, thanks to a dual beam double chirped pulse amplification (CPA) system, is able to deliver either 150 TW (4.5 J in 30 fs) or full PW (30 J in 30 fs) to the target, with a maximum repetition frequency of 1 Hz [95]. The laser beam is currently guided from the laser room to a dedicated experimental cave, where laser-target interaction is studied, focusing on the optimization of ion acceleration and control, and on the development of real-time tools for plasma diagnostics.

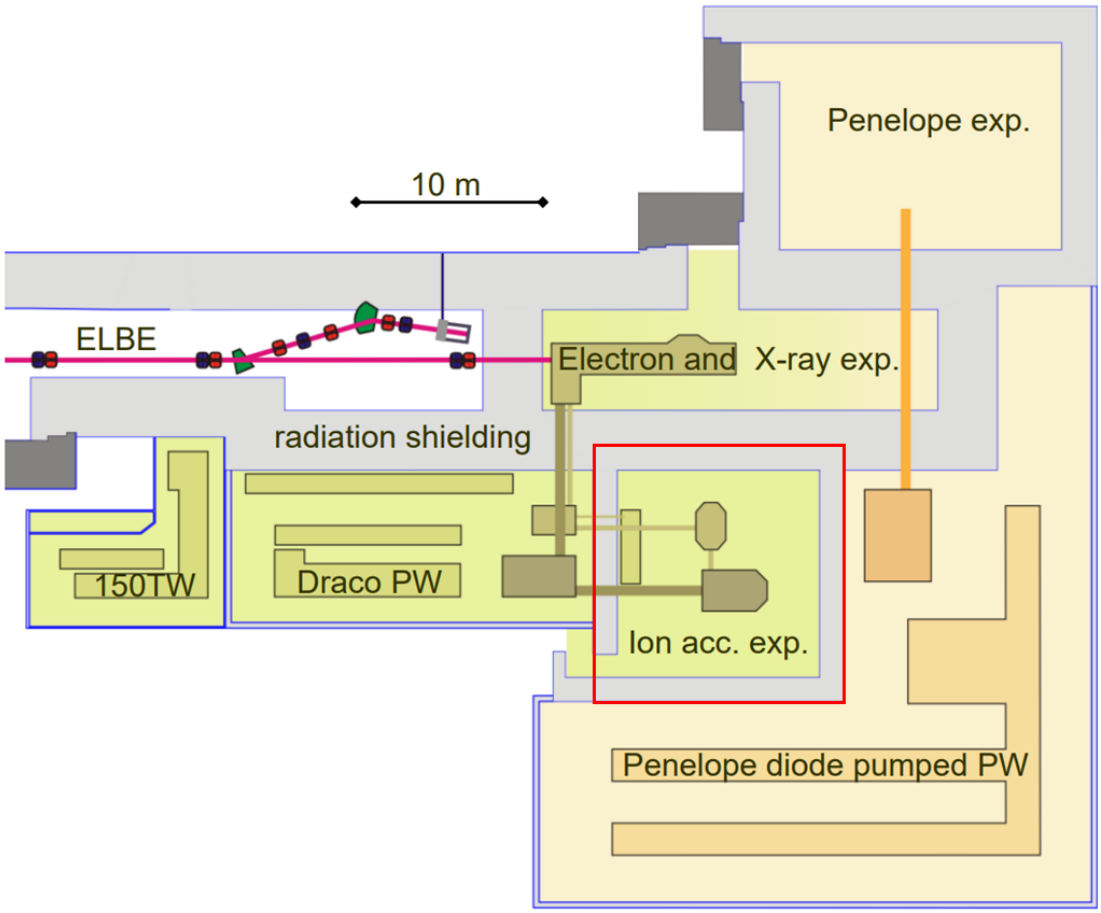

Figure 28. Plan of the HZDR ELBE center for high power radiation sources. The area in green shows the Dresden Laser Acceleration Source (DRACO). The DRACO ion acceleration experimental cave is enclosed in the red rectangle. Picture adapted from *Schramm et al.* [95].

The DRACO ion acceleration experimental cave (in the following simply *experimental cave*) is a 9 x 9 m^2 room surrounded by 1 to 3 m thick concrete shielding walls hosting the vacuum chamber where the laser-target interaction takes place. The vacuum chamber itself is a 2.5 cm thick aluminum structure, about 3 m long, 2 m wide and 2 m high, equipped with several laser and particle diagnostic tools used to best characterize the produced particles and monitor the laser quality. In addition to these, two bulky solenoid magnets are installed, one inside the vacuum chamber and one outside, to focus the produced bunches of protons and transport them outside of the vacuum chamber where they can be used for proton irradiation experiments [13]. The DRACO vacuum chamber can be seen in Figure 29 from the front (Figure 29a) and from the side (Figure 29b).

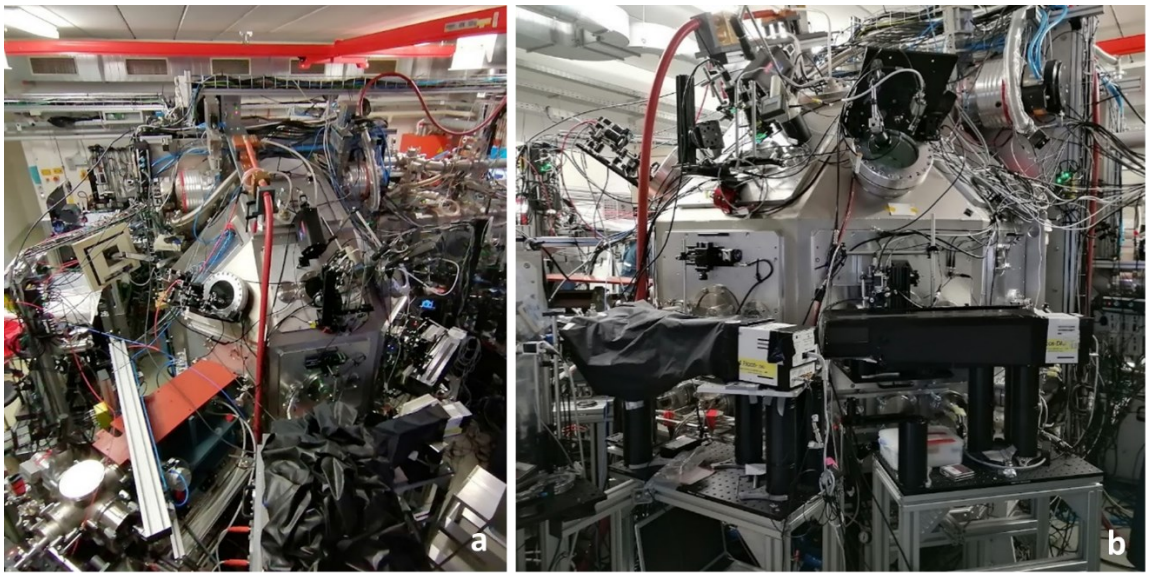

Figure 29: Photos of the vacuum chamber of the DRACO proton acceleration facility from the front (**a**) and from the side (**b**).

In August 2021, parasitic and dedicated measurements of the secondary neutron dose produced in proximity of the vacuum chamber were performed by using the LUPIN-II and the Passive-LINUS, for a variety of laser-target materials, laser energies on target (from 8 to 32 J), and proton cutoff energies (up to 60 MeV). Additionally, the photon dose was monitored by the NAUSICAA (IC-T-PF version) [96], an ion chamber developed for pulsed photon fields able to measure photon radiation in the energy rage from 30 keV to 10 MeV (ELSE Nuclear, Busto Arsizio, Italy). Preliminary Geant4 Monte Carlo simulations have been performed within the frame of this thesis, in order to characterize the radiation environment and guide the positioning of detectors. Further and more detailed simulations have been performed to benchmark the dedicated experiments.

In the next Subchapters, the source description, preliminary Monte Carlo simulations, experimental setup, and experimental results with simulation benchmark are presented.

6.2 The radiation sources

As described in Chapter 2, when using the TNSA acceleration mode, one expects that most of the most energetic ions and electrons are emitted in the direction normal to the rear surface of the laser-target. In addition, it is known that a fraction of particles is also emitted in backward direction, although with lesser number of particles per bunch (about 1 order of magnitude less) and lower cutoff energies (by about a factor 2) compared to

forward-emitted particles. Together with these two components, a third relevant component exists, i.e., electrons emitted along the so-called specular reflected direction. This can be explained by considering that part of the laser pulse that drives the proton acceleration in forward direction is reflected by the target front surface. While leaving the target, this reflected laser pulse drives a small fraction of electrons and accelerates them along this direction. The described source components are shown in Figure 30. In this figure, the laser pulse comes from the left and interacts with a target material tilted by 45º with respect to the impinging laser direction. The forward protons are emitted along the direction normal to the rear surface of the target (by definition at 0º), the specular reflected electrons along the 135º direction, and the backward particles along the 180º direction.

It should be mentioned that, although electrons contribute to a lesser extent to the production of secondary neutrons compared to protons, and might be neglected in a first order approximation, they are however the main responsible source of bremsstrahlung photons which can affect and disturb the correct reading of active neutron REM counters. It is therefore evident that the experimental environment is more complex than that of a typical proton accelerator because of the presence of both electrons and protons together, and because of different particle emission directions. This knowledge of the main features of the DRACO source was used to best prepare the experimental campaign, and the Geant4 Monte Carlo simulations.

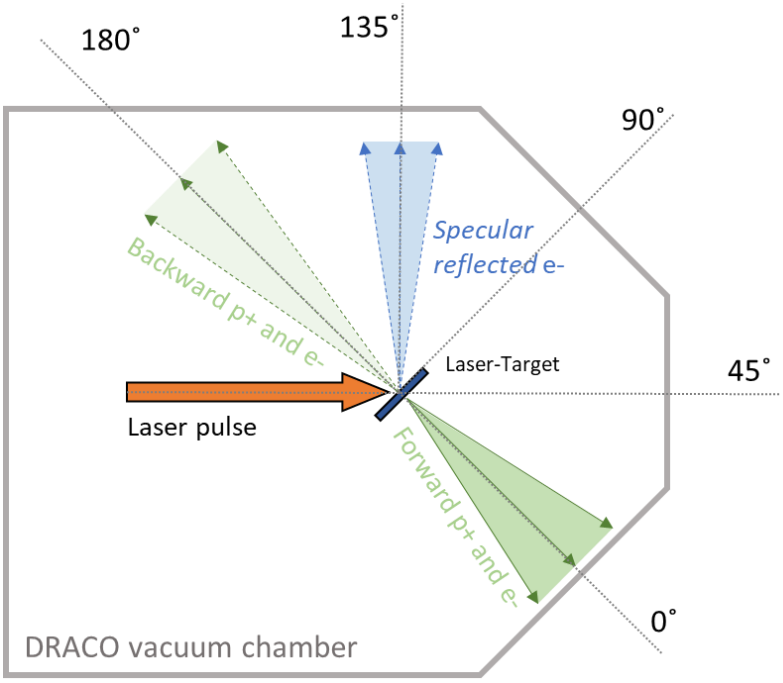

Figure 30: Drawing of the DRACO vacuum chamber with main directions of particle emission.

6.3 Preliminary Monte Carlo simulations

In preparation for the experimental campaign, DRACO-dedicated Geant4 Monte Carlo simulations were performed, to assess the magnitude and angular dependence of the expected neutron field. Figure 31a shows the overall geometry implemented in Geant4, while Figure 31b shows a close-up on the proton source. Although the DRACO experimental cave is filled with equipment, as clearly visible in Figure 29a and Figure 29b, for these simulations only the cave walls were implemented, as a first order approximation. The vacuum chamber was simulated with its real dimensions, thickness, and material composition. In addition, three components hosted inside the vacuum chamber were modeled, the solenoid S1, the backward Thomson Parabola Spectrometer (TPS), and the proton profiler. These three elements were included in the geometry because of their dimensions and vicinity to the radiation source, which make them best candidates for becoming a source of secondary radiation. With regards to the proton profiler, this is a solid slab with variable thickness that is occasionally placed between the laser-target and the forward Thomson Parabola Spectrometer (at 10 cm distance from the laser-target). The profiler is used to cut the lowest energetic protons, allowing in this way to study only protons with higher energies without the noise produced by lower energetic particles. From the point of view of the production of secondary radiation, the presence

of a relatively thick element directly in front of the source of protons, such as the proton profiler, allows for an ideal case study, because such an element is likely to be the most important source of secondary radiation, with the additional benefit of reducing the complexity of the simulation. Three scenarios were considered for the simulations:

- *Thick* aluminum proton profiler: 6.5 mm thick (used to cut protons below 40 MeV)
- *Thin* aluminum proton profiler: 1.5 mm thick (used to cut protons below 20 MeV)
- *Without* aluminum proton profiler.

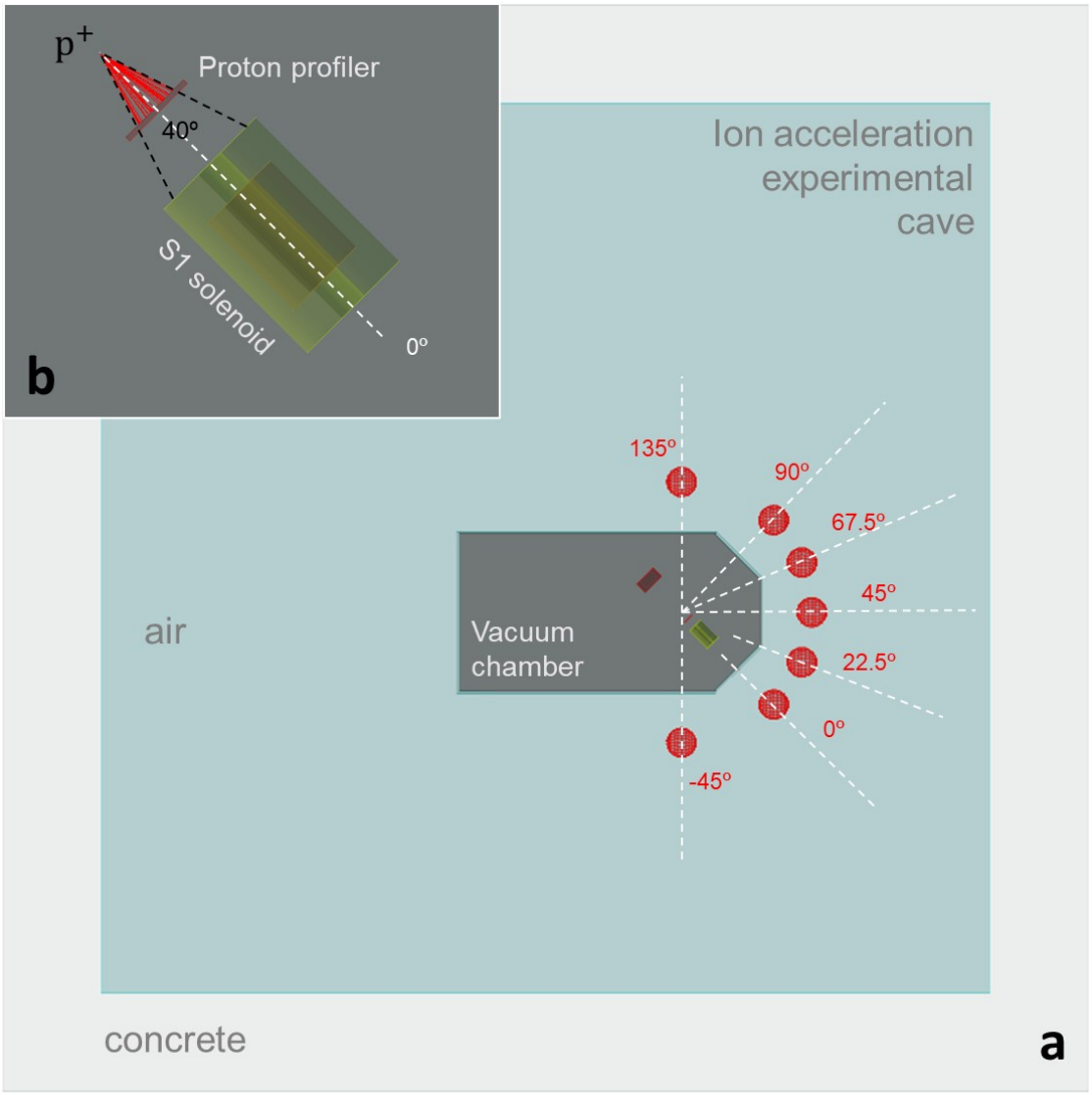

Figure 31: Geant4 simulation geometry of the DRACO experiment. **a**) DRACO cave **b**) close-up on the proton source. Red circles represent scorer positions.

Neutron scorers as described in Subchapter 4.4 (red spheres in Figure 31a) were implemented and positioned all around the vacuum chamber, at 50 cm distance from the vacuum chamber wall (130 cm from the laser-target position).

As a first order approximation, only the forward-emitted proton component was considered as source term in this preliminary study. Electrons were excluded from the simulations because of their rather marginal contribution to the production of neutrons, as shown in Chapter 5 and in [61]. The backward protons were excluded considering their low number per bunch and low cutoff energy.

To run the Geant4 simulations, two spectra that had been produced at DRACO in previous experiments were used, one published by *Brack et al.* in 2020 [13], that is it called for simplicity *Brack2020* in this thesis, and another one published F-E. Brack's PhD thesis [97], that is called here *Draco2021*, representative of the current optimized configuration [98,99]. For both spectra a histogram from 1 MeV to E_{cutoff} with 1 MeV wide energy bins was created and used as source term. Both histograms are shown in Figure 32. By integrating over the whole spectrum, the total number of protons per bunch, N, was derived for both source terms:

- $N_{Brack2020} = 1.6 \cdot 10^{11}$ protons/bunch
- $N_{Draco2021} = 8.9 \cdot 10^{11}$ protons/bunch

At this stage it is worth mentioning that these spectra include an experimental uncertainty of the order of a factor 1.5-2 in the number of particles (as visible in the box on the top-right corner of Figure 32) and, therefore, the total number of calculated protons per bunch, and afterwards used, is affected by the same degree of uncertainty.

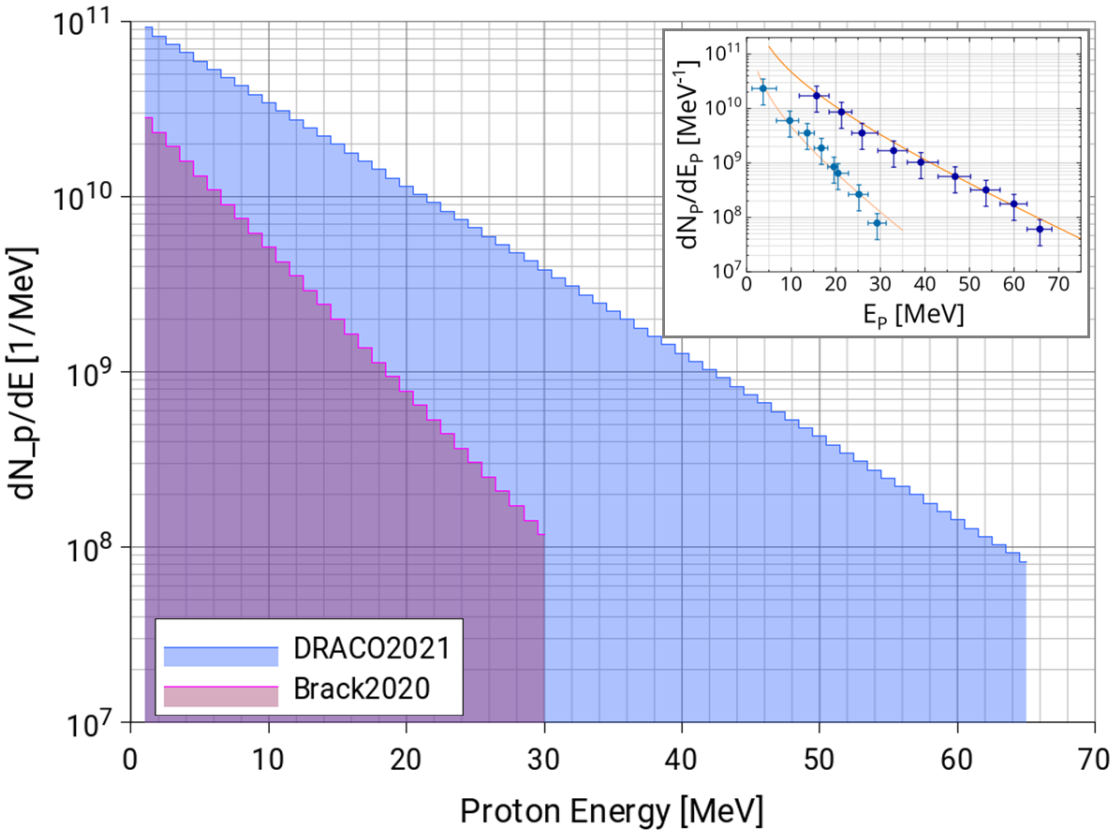

Figure 32: Input proton spectra used in the Geant4 simulations as source terms. Purple - Brack2020 based on [13]; Blue - Draco2021 based on [97]. The box in the top-right corner shows the experimental data as reported by [97].

Brack et al. [13] showed that the vast majority of forward-emitted protons is emitted within a divergence of about 20º half angle. They also showed that this angle tends to be smaller for higher-energetic particles and larger for lower-energetic ones. For simplicity, in this thesis, the initial maximum angular divergence of laser-emitted protons was set to 20º half angle, with uniform emission probability from 0º to 20º. Then, similarly to what was done for the LION-dedicated simulations, the neutron dose was simulated by folding the neutron spectra with the fluence-to-H*(10) conversion curve.

Simulation results are plotted in Figure 33, for Brack2020 on the left and for Draco2021 on the right, for all three considered scenarios (*without*, and with *thin* and *thick* proton profiler). Numerical values can be found in Table 4.

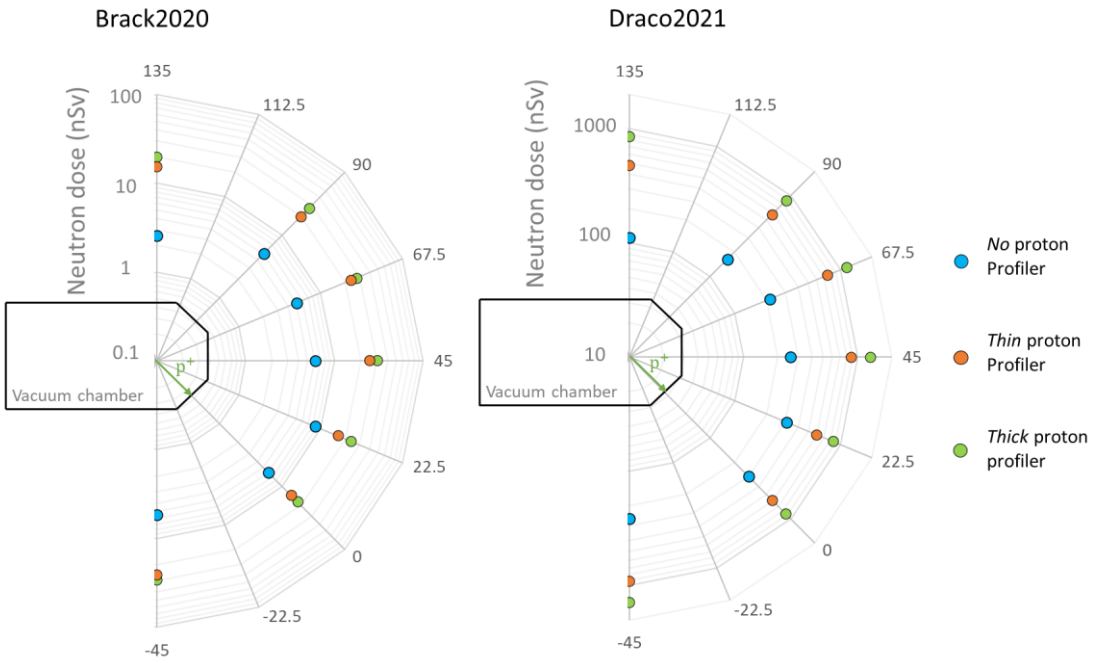

Figure 33: Neutron doses obtained in the preliminary Geant4 simulations, for the-Brack2020 (left) and Draco2021 (right) primary proton spectra.

	Brack2020 (nSv/bunch)			Draco2021 (nSv/bunch)		
Angle	**Thick**	**Thin**	**Without**	**Thick**	**Thin**	**Without**
-45º	29.44	25.92	5.42	1397.3	907.80	257.21
0º	17.44	13.87	6.01	867.75	591.85	299.04
22.5º	23.52	16.16	8.57	852.62	595.41	310.61
45º	30.56	24.8	6.13	1290.50	870.42	258.99
67.5º	23.20	23.2	5.06	1148.10	752.94	213.60
90º	26.88	19.84	5.06	870.42	582.06	163.76
135º	19.84	15.47	2.57	859.74	479.71	111.25
Avg	24.41 (18%)	19.89 (23%)	5.55 (24%)	1040.92 (21%)	682.88 (22%)	231 (29%)

Table 4: Neutron doses obtained in the preliminary Geant4 simulations performed as part of this thesis, for the DRACO experimental campaign (see also Figure 33).

The simulated neutron doses per bunch span three orders of magnitude, from about 3-30 nSv/bunch when using the Brack2020 primary proton spectrum, up to 0.1-1

µSv/bunch when using the Draco2021 primary spectrum. It is worth mentioning that lowest values were found for the geometry without proton profiler, while highest for the geometry employing the thicker profiler. This is a reasonable result because in the case where no profiler is used, almost all primary protons interact with the first solenoid, a cylindrical copper element fully enclosed in a 3 cm thick PEEK[9]-made structure that acts as a neutron shield. On the other hand, both proton profilers act as proton-neutron converters, while only attenuating but not shielding neutrons.

Because the neutron doses per bunch close to the vacuum chamber were expected to reach values in the order of 100-1000 nSv/bunch, it was decided to consider only the LUPIN-II to carry out single-bunch neutron dose measurements and to discard the conventional REM counters NM2B-458 and NM2B-495Pb, for which, as already discussed, already 10 nSv/bunch would be challenging to measure. In addition, if one considers that a few hundred laser pulses can be expected in a measurement campaign, total neutron doses in the order of a few dozens of µSv can be expected. Based on these considerations the Passive LINUS was considered as a good candidate for total integrated neutron dose measurements. Neutron spectrometry with the Au-BSS was discarded for this experimental campaign given the rather low total number of expected laser pulses and proton cutoff energies.

Another remarkable result derived from the simulations is that, for the considered configurations, the source of radiation seems to be rather isotropic: for all three geometries and both primary proton spectra, the standard deviation of the average value calculated on all scorers is less than 30%. The rather isotropic distribution of the neutron field can also be seen in Figure 33. This finding is of great importance because it shows that measurements performed simultaneously at different angles could still be directly comparable.

6.4 Experimental setup

6.4.1 Detector positions

As shown in Figure 34a, the experimental equipment was positioned 90º from the direction of emission of the primary protons (0º). The LUPIN and the NAUSICAA were placed

[9] PEEK stands for Polyether ether ketone, an organic thermoplastic polymer.

at about 200 cm from the laser-target, while the Passive LINUS at 220 cm[10]. As show in Figure 34b, the LUPIN-II was standing on a ladder at the height of 120 cm and the NAUSICAA was below it, on the floor. The Passive LINUS was also at the height of 120 cm placed on a separate stand at a distance of about 50 cm from the LUPIN-II.

The different distances from the source chosen was due to space constraints set by the presence of several other structures whose position in the experimental hall was fixed. Placing the detectors at these specific locations followed different considerations:

- The chosen positions were one of the few positions in the experimental hall where it was possible to place several devices with the size of a REM counter without blocking any passages or access to other experimental equipment,
- The chosen positions offered an almost clear view of the vacuum chamber, without any other bulky component being in the way,
- In these positions, the detectors were not directly in the direction of any of the most important components of the laser-emitted particles, as shown previously.

Because of the very low number of available laser pulses and the shot-to-shot variability, it was decided to keep the detectors in the above-described positions for the whole measurement campaign. In this way each single-bunch measurements of the LUPIN-II could be compared with each other, without any further consideration on the detector position. This in turns means that a direct comparison of the readings of the three different detectors was always affected by the fact that the different devices were not irradiated at the very same location.

[10] The distance was measured from the wall of the vacuum chamber, and the actual distance from the laser-target was derived by knowing that the vacuum chamber wall is 80 cm away from the laser-target.

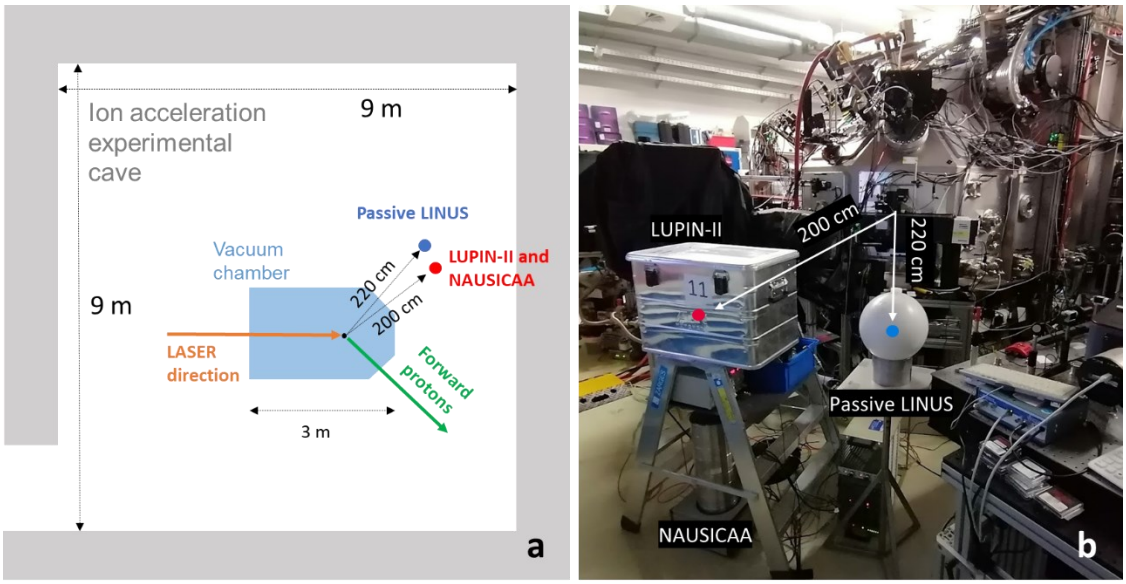

Figure 34: **a**) Drawing of the DRACO proton experimental area. The position of the detectors during the measurement campaign is marked by blue and red dots. **b**) Picture of the experimental setup used during the whole measurement campaign.

Because also electromagnetic fields were expected when the laser interacts with the target, whose intensity could in principle affect the reading of any active devices, the required electronic modules were placed in the control room, outside of the experimental cave. As additional precaution, the LUPIN-II was placed inside a Faraday cage prototype built out of an aluminum transport box (Figure 34b) and its signal and power cables were additionally shielded with a braided copper sleeve for their whole length.

6.4.2 Accelerator configurations

A total number of 320 laser pulses were shot with various laser energies (8, 14, 22, and 30 J) onto 12 different combinations of laser material and thickness. The parasitic measurements occupied most part of the measurement campaign with about 300 laser shots, while only 17 were dedicated to measurements of secondary neutrons. Below is a list containing all the laser-target materials employed during the described measurement campaign:

- Titanium (Ti): 2, 5, 10, and 25 μm thick
- Gold (Au): 2 μm thick
- Formvar[11] (FV): 250 nm thick

[11] Formvar is a polyvinyl formal (thermoplastic resin)

- PET[12]: 0.5, 1.5, 23, 100, and 250 µm thick
- PET + 200 nm of gold (Au): 0.5, 1.5, 23, 100 and 250 µm thick

Of all the targets used for the parasitic measurements, only the 250 nm thick FV was also used for the dedicated measurements. This was decided in agreement with the DRACO laser group by considering the fact that this is the laser-target for which higher proton cutoff energies can be usually reached, according to their experience.

During the parasitic measurements, the protons emitted in forward direction were monitored by a Thomson Parabola Spectrometer, positioned at 0º, which allowed monitoring the proton cutoff energy for each laser shot. Due to the very large divergence of particle emission, a large fraction of laser-emitted particles interacts with the various elements hosted inside the vacuum chamber, leading to the production of secondary neutron and photon radiation in these elements, and only a very small fraction of them is detected by the Thomson Parabola Spectrometer. Concerning secondary neutron measurements, the problem of this parasitic configuration was, hence, that the neutron source was not clearly identifiable with a specific component at a given position. This led to large uncertainties when simulating the neutron production. To overcome this problem, the dedicated laser shots were carried out with a proton profiler positioned close to the laser-target, in forward direction, as previously mentioned. In this way, the vast majority of laser-emitted particles was then stopped by the proton profiler producing secondary radiation from a well-defined location, as in a sort of pitcher-catcher non-optimized configuration.

6.5 Experimental results

6.5.1 Parasitic measurements – neutron single-bunch doses

The overall results of the parasitic measurements are summarized in Figure 35. Here the neutron dose per laser shot detected by the LUPIN-II is plotted against the proton cutoff energy of the respective laser pulse. Two features appear by looking at this plot:

- Overall, the measured neutron dose indicates an energy threshold at proton cutoff energy in the range from almost 7 to about 18 MeV. In general, below 6 MeV proton cutoff energy no neutron dose was measured (apart from random background radiation). This is generally in agreement with the fact that proton-induced

[12] PET: Polyethylene terephthalate

neutron production is a threshold phenomenon, whose value, although dependent on the involved element, is in the order of some MeV.

- Above 20 MeV proton cutoff energy, the neutron dose per bunch increases with increasing cutoff energy, roughly following a rather linear behavior.

It is worth mentioning that the measured neutron dose values fall within the region of linearity of the LUPIN-II detector in pulsed fields (up to about 500 nSv/bunch). Nevertheless, the neutron dose measured by each single bunch was corrected by applying the following empirical formula proposed by *Caresana et al.* [58] to correct the readings of REM counters when operated in pulsed neutron fields:

$$D_{ref} = \frac{D_{meas}}{1 - \left(\frac{D_{meas}}{D_{half}}\right)} \tag{11}$$

Where D_{ref} is the actual neutron dose per bunch, D_{meas} is the measured dose per bunch and D_{half} is the "half response dose", a value at which the detector underestimates the reference dose of a factor 2. This latter was experimentally derived by *Caresana et al.* for several neutron REM counters during a dedicated measurement campaign and its value for the LUPIN-II was 1,808 nSv/bunch [58].

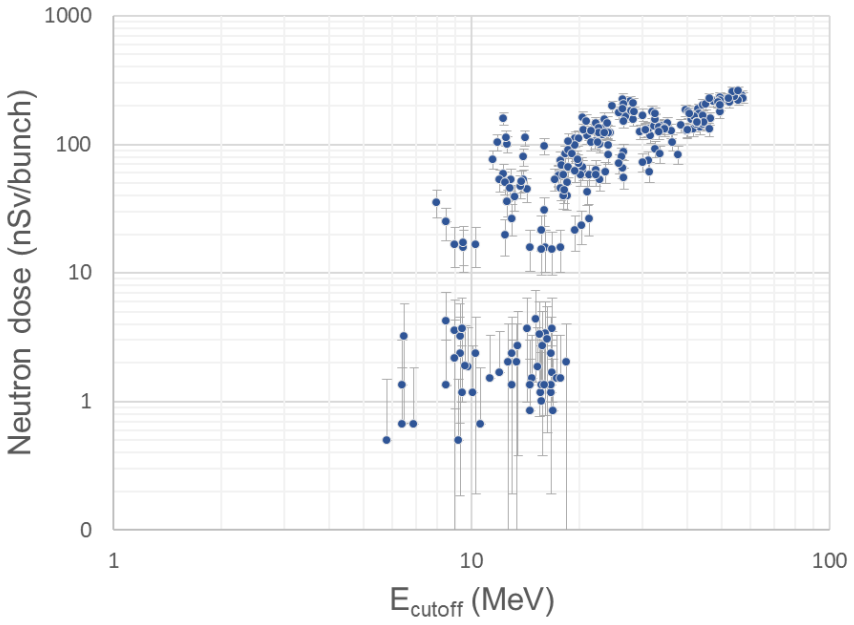

Figure 35: Neutron dose per bunch measured at DRACO by the LUPIN-II plotted against the proton cutoff energy. Each datapoint represents the neutron dose for a given proton bunch.

6.5.2 Parasitic measurements – integrated neutron doses

Integrated neutron dose measurements were performed by using the Passive LINUS, (intrinsically unaffected by the pulsed nature of the radiation and by the presence of the photon field), in order to benchmark the total neutron dose measured by the LUPIN-II.

Due to the rather low sensitivity of the Passive LINUS, it was decided to perform the passive measurement by integrating over a whole measurement day. Overall, the described measurement campaign was composed by two experimental days and, hence, two measured values, one representative of the first day and one of the second day, were acquired. For both measurement days, the data acquisition of the LUPIN-II was started when the Passive LINUS was set in position. In this way both devices measured for the same period of time. Since the two detectors were positioned at a different distance from the laser-target, a distance correction factor had to be applied to one of the two detectors, to allow for a direct comparison of the two measurements. By applying the inverse square law, and considering that the LUPIN-II was standing at 200 cm from the laser-target while the Passive LINUS was at 220 cm, the distance correction factor, c_{dist}, was found as follows:

$$c_{dist} = \left(\frac{200}{220}\right)^2 = 0.83 \tag{12}$$

Thus, the distance-corrected LUPIN-II dose measurement, D_{corr}, was simply found by multiplying the measured value, D_{meas}, by c_{dist}:

$$D_{corr} = c_{dist} \cdot D_{meas} \tag{13}$$

The application of the inverse square law is justified by considering that in this experimental position the simulations suggest that the neutron field was rather isotropic, and that the radiation source could be considered as a point source.

As described in Subchapter 3.3.2.1, the net track density measured by the Passive LINUS was derived by calculating the average of the track density found in the two CR39 simultaneously exposed and subtracting the resulting value by the average track density found on the unirradiated CR39 samples (used to estimate the intrinsic noise of the CR39). The remaining net track density was then multiplied by the calibration factor of 18.70 $\mu Sv^{-1}cm^{-2}$ (derived in Subchapter 5.1.2) to get the neutron dose expressed in μSv.

Experimental results are given in Table 5 and plotted in Figure 36.

	LUPIN-II (μSv)		Passive LINUS (μSv)	Background (μSv)
	D_{meas}	D_{corr}		
Day1	11.12 (± 17%)	9.21 (± 17%)	4.8 (± 62%)	0.28 (22%)
Day2	14.20 (± 17%)	11.76 (± 17%)	9.56 (± 21%)	0.26 (22%)

Table 5: Integrated neutron values measured with the LUPIN-II and the Passive LINUS.

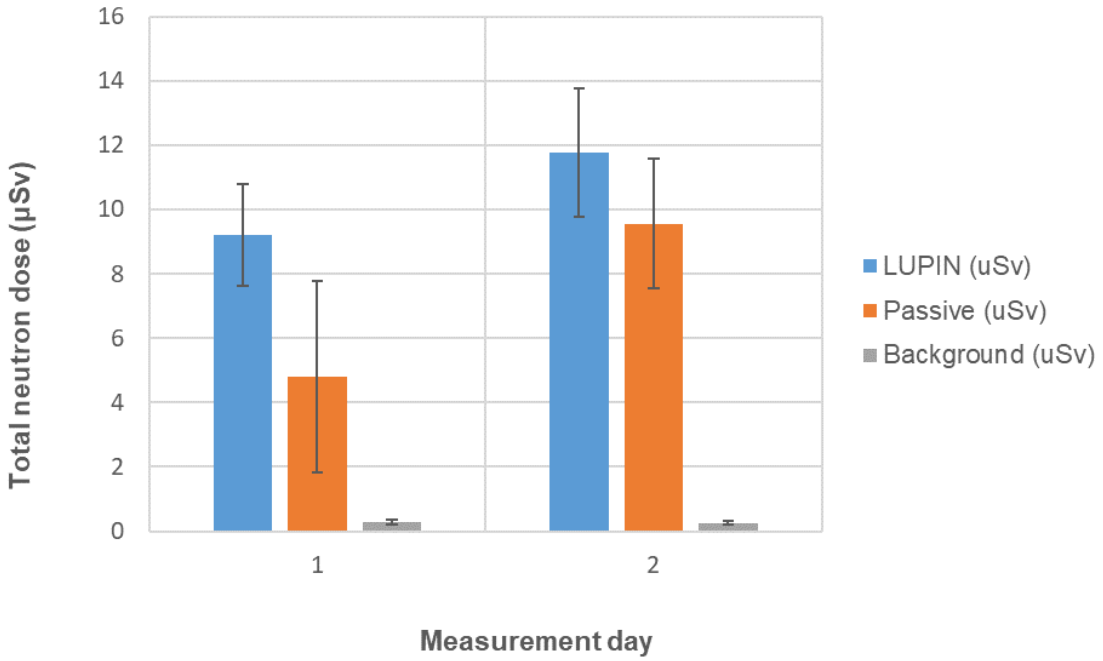

Figure 36: Comparison of the integrated neutron dose obtained with the LUPIN-II and the Passive LINUS for both measurement days.

Before the beginning of the actual irradiations, a background measurement was performed with the LUPIN-II resulting in an average dose rate of 22.5 nSv/h (±22%). Considering that the first measurement lasted 12.5 hours and the second one 11.5 hours, 281 nSv (±22%) and 259 nSv (±22%) were the contribution of the background to the measured doses on first and the second day of measurements, respectively. As it can be seen in Figure 36, as expected both devices measured neutron doses well above the neutron background in both experimental days, also considering the associated uncertainties.

On both measurement days the LUPIN-II measured more than the Passive LINUS, on the first day by a factor 1.9 while on the second day by a factor 1.2. This discrepancy in the measurement of the two devices is higher than what is usually found for this type of instruments, especially that on the first measurement day. This fact can be explained by

considering that the Passive LINUS has a rather low neutron sensitivity and rather high intrinsic noise (~37 cm^{-2}) and therefore, at these low neutron doses, its uncertainty is very high. On the second day of measurements, due to the production of higher secondary neutron doses, the measurement uncertainty of the passive LINUS was much lower (21%) and, consequently, the measured values of the two REM counters show better agreement.

The fact that the LUPIN-II detector seems to systematically measure more than the Passive LINUS could be also attributed to two possible causes:

- a partial contamination of the measured value by pulsed photons, whose interaction in the LUPIN-II proportional counter could in principle generate enough charge per unit time to overcome the detection threshold set on the derivative of the signal and, consequently, be accumulated as neutron-induced charge,
- because the LUPIN-II was positioned at a smaller angle (~15º) compared to the Passive LINUS, this could lead, although preliminary simulations show that the field is rather isotropic, to partially higher neutron fluxes, given the fact that the production of neutrons is mostly driven by protons emitted in forward direction, especially when no proton profiler is used (which was the case for almost all shots).

One can therefore conclude that, although high uncertainties affected the reading of the Passive LINUS, and although a slight overestimation was found on the readings of the LUPIN-II detector, the measured values of the two devices showed a rather good agreement. This confirmed that the LUPIN-II can be used to perform measurements in the radiation environment of a laser-driven proton accelerator.

6.5.3 Dedicated measurements and Monte Carlo simulations

Aim of the dedicated experiments was to experimentally recreate an as much as possible simple configuration (*pitcher-catcher*-like) to test the simulation settings, and, where needed, suggest targeted improvements to guide future, more detailed simulation studies.

As briefly mentioned in the Subchapter 6.4, during the dedicated measurements a 10 x 10 x 1.6 cm^3 aluminum proton profiler was positioned at 6 cm distance from the proton source, in forward direction (see Figure 37). Since the aim of this component is to stop the vast majority of laser-emitted particles and ideally be the only source of secondary neutron radiation, its thickness, surface and distance from the source were chosen in a

way that even the most energetic (~65 MeV) and divergent (~30˚ half angle) particles could be stopped. In addition, a 0.35 cm thick ceramic layer was added on the front face of the proton profiler to avoid the production of aluminum debris, as a result of the direct interaction of protons with the aluminum slab surface. The overall thickness of the composite proton profiler was then 1.95 cm.

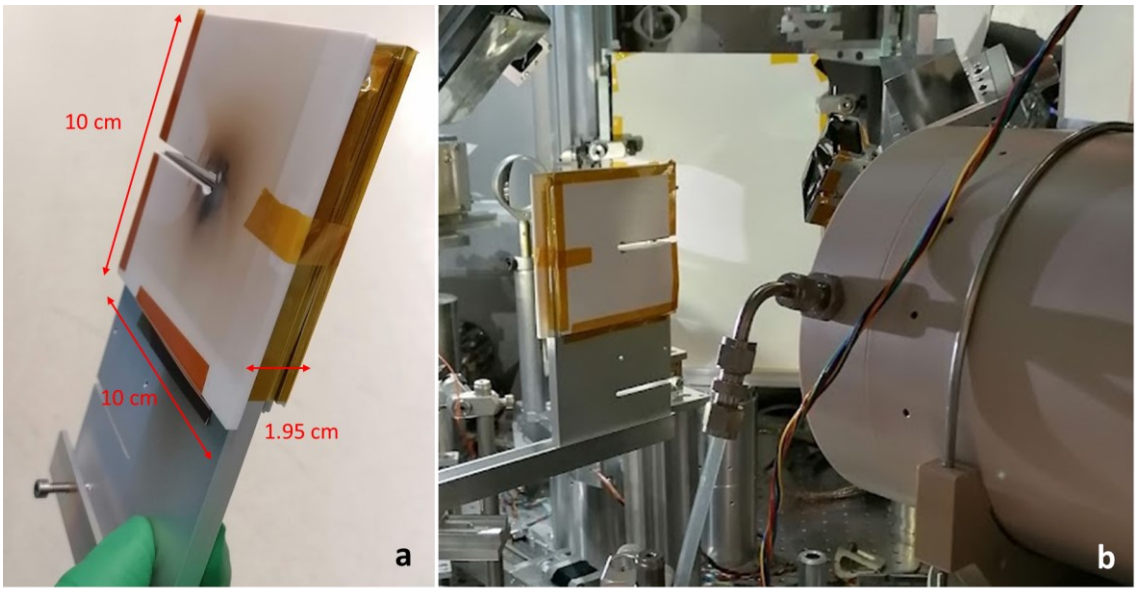

Figure 37: **a**) Ceramic-aluminum composite proton profiler used during the dedicated measurements, with dimensions in red. **b**) Proton profiler in its experimental position inside the vacuum chamber.

In order to perform proton spectrometry also during the dedicated shots, a slit in the proton profiler was left open to allow a certain fraction of protons to pass through undisturbed and get afterwards measured by the Thomson Parabola Spectrometer (TPS). The downside of this configuration is that necessarily not all protons are stopped at a single position as desired in the design of this experiment.

The total number of dedicated laser shots was 17, two with lowest laser energy (8 J), and five with 14.4 J, 22 J, and 31.8 J.

In this case, the preliminary Monte Carlo simulation geometry described in Subchapter 6.3 was adapted to the configuration used. A composite proton profiler was introduced with similar dimension and material composition as the one used in reality (ceramic-aluminum), and neutron scorers were positioned at the actual distance occupied by the LUPIN-II during the experimental campaign (200 cm from the laser-target position). For simplicity, no aperture in the proton profiler was simulated. Simulations with both

Brack2020 and Draco2021 proton spectra were performed, the first one being representative of proton bunches of about 30 MeV cutoff energy, and the second one of shots with about 65 MeV cutoff energy (see Figure 32).

The results of the dedicated measurements are plotted in Figure 38 as red data points, while in blue the values derived by using the Geant4 Monte Carlo simulations for scorer 3, the one that most closely approximated the LUPIN-II experimental position.

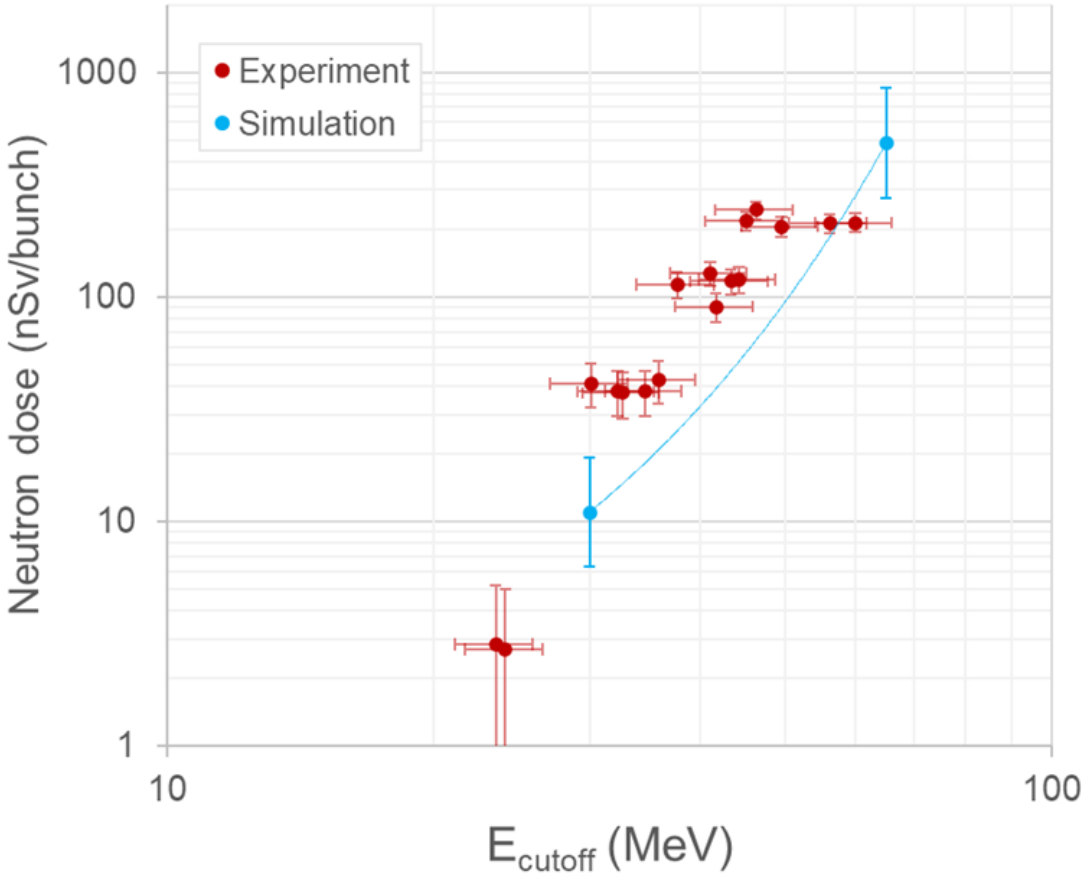

Figure 38: In red, neutron doses per bunch measured during the dedicated measurement session. In blue neutron doses per bunch calculated by Geant4 Monte Carlo simulations using the proton spectra shown in Figure 32.

As it can be seen from Figure 38, neutron doses per bunch generally increase by increasing cutoff energy of laser-driven protons, appearing consistent with the threshold-like behavior observed in the parasitic measurements.

The simulated neutron dose at 30 MeV proton cutoff energy (Brack2020) underestimates the measured neutron doses of about a factor four, while the neutron dose simulated with the highest proton cutoff energy (Draco2021) shows a factor 2.5 higher neutron

dose per bunch compared to the highest measured result. It needs to be mentioned that Draco2021 has a cutoff energy of 65 MeV while the maximum experimental cutoff energy was 60 MeV and therefore a slight overestimation was expected, and as it can be seen the interpolation curve is well in agreement with the measured data at about 60 MeV. Regarding the results at 30 MeV, even considering the large uncertainties bars, there is only partial agreement with the measurements. It is concluded that the approximation in geometry and source terms (only forward protons were considered) proved to be a reasonable first order approximation to simulate the magnitude of the secondary neutron fields expected at laser-driven ion sources, although improvements will be necessary to get better agreement with the experimental results.

To refine the simulation environment, actual proton spectra acquired during the measurement campaign would be needed, preferably with an estimate on the total number of protons per bunch with lower uncertainty, to be used as input parameters. In addition to this, information on the backward-emitted fraction of protons and on the electron component should be also added to the simulation to increase the accuracy of the simulation (see Figure 30). For example, it has to be considered that, although forward-emitted electrons should contribute to the production of neutrons only marginally compared to protons [84], the specular-emitted fraction of electrons interacts with components rather close to the detector position (represented by scorer 3). Hence, the secondary neutrons produced from this location can in principle more easily drift towards the position of scorer 3 and get detected.

Additionally, although the physics models used for the simulations were benchmarked with FLUKA in an early stage of the project (see Appendix B), tests of different physics models could help understanding the discrepancy between simulations and measurements.

6.5.4 Neutron yield calculation

By assuming an isotropic neutron emission, as suggested by the simulations, it is possible to roughly calculate the neutron yield of this experiment, Y_n, for the considered range of energies according to equation (14) and compare it with results from laser-driven *neutron* source experiments:

$$Y_n = \Phi_{n,r} \cdot 4\pi r^2 \tag{14}$$

Where $\Phi_{n,r}$ is the neutron fluence at distance r, 200 cm in the present case. Table 6 reports the calculated neutron yields (n/bunch and n/p) for all primary proton cutoff energies.

E_{cutoff}	$Y_n\left(\frac{n}{bunch}\right)$	$y_n\left(\frac{n}{p}\right)$
30 MeV	$1.78 \cdot 10^8$	$1.09 \cdot 10^{-3}$
65 MeV	$2.01 \cdot 10^9$	$2.26 \cdot 10^{-3}$

Table 6: Calculated neutron yields expressed in terms of number of neutrons per bunch, Y_n, and neutrons per primary proton, y_n.

The neutron yield Y_n calculated by Geant4 Monte Carlo simulations ranged from 10^8 to 10^9 neutrons per bunch. This is a factor 100 to a factor 10 less than maximum neutron yields currently achievable at laser-driven *neutron* sources, as mentioned in Subchapter 2.2.

The calculated neutron yield per primary proton is of the order of 10^{-3} neutrons per primary proton (doubling from 30 to 65 MeV cutoff energy). *Anderson et al.* [101] reported neutron yields at about 30 MeV proton cutoff energy to be higher by a factor 10-20, using beryllium as converter material, in agreement with the fact that beryllium is one of the elements most widely used as catcher material, due to its high neutron yield and low neutron self-absorption.

6.5.5 Photon dose measurements

Although the whole experimental activity was focused on neutron dose measurements, the photon dose was also monitored to estimate the total delivered dose and to better understand the features of the secondary radiation field, as a whole. The ion chamber NAUSICAA (IC-T-PF version) was used because it withstands photon fields of up to several µSv/bunch. The total measured photon dose was about 128.3 µSv, a factor 5 higher than the total neutron dose measured by the LUPIN-II (about 25 µSv). In Figure 39 neutron and photon dose per bunch are plotted, target by target, against the proton cutoff energy. For statistical reasons this was done only for those laser-target materials irradiated with more than five laser shots and with neutron dose values also above the threshold energy. Clearly, the photon signal, compared to the neutron signal, doesn't show any threshold behavior. This is reasonable considering that photons are mostly produced by electron bremsstrahlung, a process that does not have a threshold energy.

The fact that the neutron signal shows a threshold behavior while the photons signal doesn't, also confirms that, if the LUPIN-II neutron signal was indeed affected by pulsed photons, it could only have been in a mild way, otherwise this threshold behavior of neutron production would have been washed out. This finding strengthens the evidence that the LUPIN-II signal acquired at DRACO is trustable.

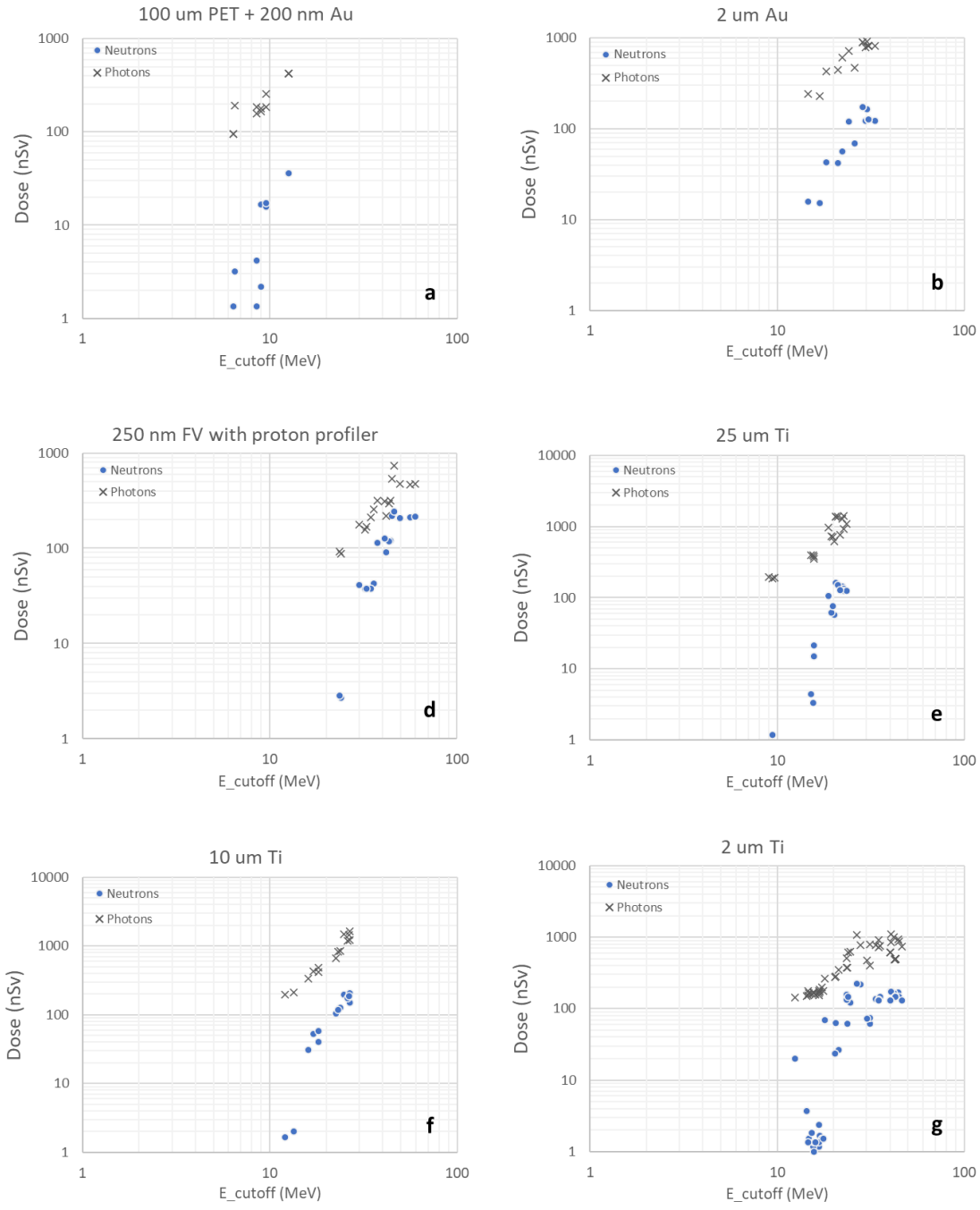

Figure 39: Comparison of measured photon (black crosses) and neutron (blue dots) doses per bunch plotted against the proton cutoff energy, for six target materials. As

clearly visible, the neutron signal shows, in most of cases, a clear threshold behavior while the photon signal does not.

7. Discussion

As mentioned in Subchapter 2.2, *Sakaki et al.* [34] measured a few µSv/bunch total dose (ranging from 0.9 to 3.67 µSv depending angle) on the surface of the vacuum chamber (~50 cm from the source of radiation) by using passive glass dosimeters and averaging over several shots with mean proton cutoff energy of about 7 MeV. As a comparison, the total (neutron plus photon) dose measured during the DRACO measurement campaign by the LUPIN-II and NAUSICAA detectors for shots with proton cutoff energy from 6 to 7 MeV was of the order of 120 (± 35%) nSv/bunch. Considering the four times larger distance employed during the DRACO measurements one can conclude that the two results are in a rather good agreement, despite the different facilities and irradiation conditions.

In the following, the simulation results (in terms of neutron dose per bunch) derived for LION are discussed in comparison with the experimental results acquired during the measurement campaign at DRACO, in order to validate, or at least compare, the simulation work performed on the LION facility with experimental data that could not be directly acquired at the LION facility. This comparison is of particular relevance considering that the total number of protons per bunch described in Appendix C and used to derive total neutron doses per bunch in Subchapter 5.3 is based only on energetic considerations and, consequently, large uncertainties are associated to it. In addition, it must be pointed out from the beginning that the two facilities are different in geometry and materials, and therefore any conclusions should be drawn with care. Since all data acquired in the DRACO parasitic measurement campaigns lie within 6 and 60 MeV proton cutoff energy, only the simulation results derived by using the Zeil2010 (E_{cutoff} ~12 MeV) and Ma2019 (E_{cutoff} ~56 MeV) proton spectra are considered here for the comparison.

The LUPIN-II position during the DRACO measurement was at about 90º from the direction normal to the target and at about 200 cm distance. In the LION simulations, there is one scorer whose position is analogous to that of the LUPIN-II detector during the measurements at DRACO (scorer number 5; see Figure 16). This scorer was placed at 90 degrees from the direction normal to the target at about 100 cm distance. To perform a reasonable comparison, the inverse square law was applied to the results of the LION simulations, to derive an estimate at 200 cm distance. Figure 40 shows the neutron dose per bunch measured during the parasitic measurements (in blue, as already shown in Figure 35) together with neutron dose resulting from the LION simulations for scorer 5 in orange (considering only the Zeil2010 and Ma2019 primary proton spectra).

Figure 40 demonstrates that at about 56 MeV cutoff energy the results derived by the Monte Carlo simulations on LION are in the same order of magnitude of the experimental data acquired at DRACO, while, at 12 MeV, the simulations show neutron doses per bunch at least one order of magnitude lower. The reason for this could lie in the fact that in the LION simulations a large fraction of primary protons interacts with the glass-made cone placed in front of the first QP and that ^{28}Si (one of the most abundant elements of the borosilicate glass used) has a threshold energy for neutron production of about 9 MeV (for comparison, ^{27}Al has the corresponding threshold at 6 MeV). Therefore, most protons belonging to the Zeil2010 proton spectrum, when interacting with the glass-made cone, simply lose their energy via scattering events without inducing proto-neutron reactions and get stopped without reaching the aluminum slab beneath. In contrast, a large fraction of protons produced experimentally at DRACO interacts with the elements hosted inside the vacuum chamber which are mostly made of aluminum and other metals. It is worth mentioning additionally that the experimental data acquired at these low proton cutoff energies (from 6 to 17 MeV) are rather inhomogeneous and neutron dose per bunch values span several orders of magnitude making this low-energy part of the results rather uncertain.

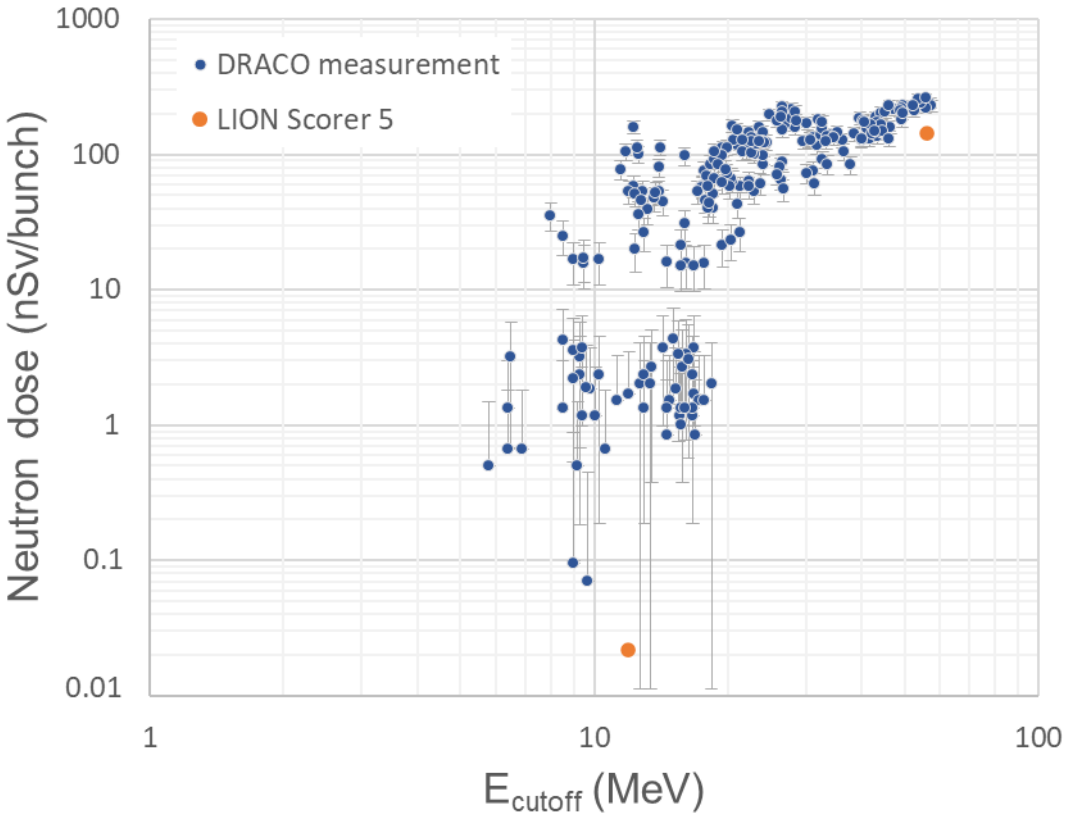

Figure 40: Comparison between the scaled LION simulation for scorer 5 (orange dots) and the neutron dose measured during the DRACO measurement campaign (blue dots). For details see text.

In general, this comparison shows that at high proton cutoff energy (~56 MeV) a relatively good agreement between the simulations at LION and the measurement at DRACO was found, suggesting that the approach followed to derive the total number of particles per bunch was appropriate, at least for the Ma2019 spectrum. Of course, for a clear validation, measurements at LION with Ma2019-like spectra are needed. At low proton cutoff energy, the results of the comparison are less clear, given the uncertainty in the measured data, on one hand, and the impact that the neutron production threshold of different elements has on the production of neutrons, especially when low energy proton spectra are considered, on the other. However, the fact that all measured neutron doses per bunch in the range 6 – 17 MeV (threshold region of the measured data) lie above the simulated neutron dose found for LION Figure 40) suggests that probably the LION simulation using the Zeil2010 proton spectrum tends to underestimate the produced neutron dose. Experimental verification, in principle compatible with the current status of the accelerator commissioning, would be required to confirm this finding.

A further comparison with the LION Geant4 simulations can be done on the neutron-to-photon dose ratio: the total measured dose by the LUPIN-II and by the NAUSICAA during the measurement campaign at the DRACO laser-driven proton source at 2-meter distance from the source was about 154 uSv, calculated by summing over all shots (~320). Of these, about 130 µSv were due to photons (~85%) and about 25 µSv due to neutrons (15%), resulting in a neutron-to-photon ratio of ~ 0.2. This reflects the findings reported in [84] on the LION facility where it was pointed out that in the surrounding of laser-driven ion sources the environment is dominated by photon radiation, and only with very intense proton spectra (in this publication represented by the Wagner2016 spectrum with cutoff energy of about 86 MeV) neutron radiation was predominant over photon radiation. In addition to this, the neutron-to-photon dose ratio derived for each laser shot during the measurements at DRACO was plotted against the proton cutoff energy (green dots in Figure 41). As can be seen, the range of values goes from $4 \cdot 10^{-3}$ to 0.8 with a distinct continuous increase from low proton cutoff values to high proton cutoff values. On the same plot the calculated neutron-to-photon dose ratio for the LION facility is plotted as well (orange dots). As already mentioned, only the results for scorer 5 were used because this scorer was placed at 90º from the source of radiation, similarly to the experimental position at DRACO. The simulations show a surprisingly good agreement with the experimental data acquired at DRACO, despite the different facility and the approximations in the proton and electron source terms definition described in 5.2.2. This finding suggests that the definition of the electron source term (mainly responsible for the production of photons) based on empirical formulas represents fairly well the reality and should be used whenever electron spectral information coming from measurements is missing.

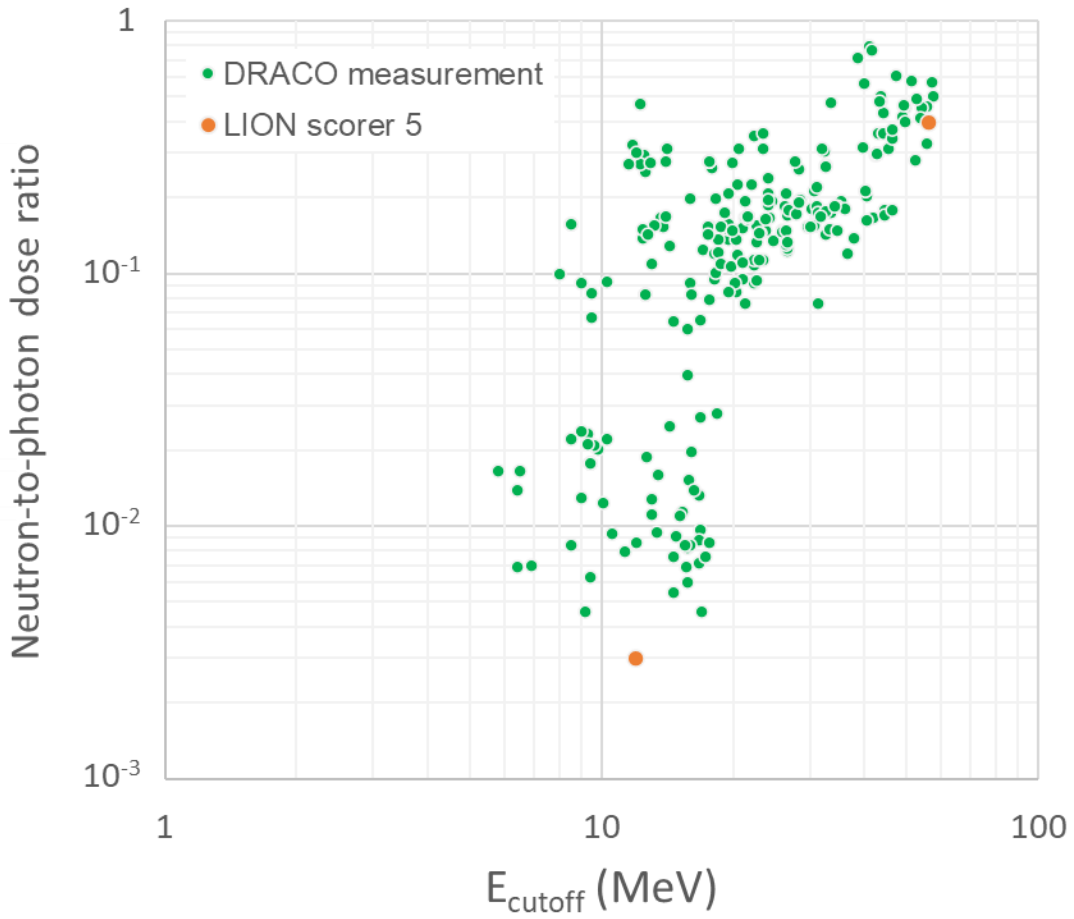

Figure 41: Neutron-to-photon dose ratio versus proton cutoff energy. Green symbols - results measured at the DRACO facility; orange symbols - GEANT4 simulations for the LION facility as presented in [84].

8. Conclusions and Outlook

The aim of the present work was to investigate the production of secondary radiation, with focus on neutrons, during the operation of laser-driven ion accelerators. The present study was motivated by the envisioned future employment of laser-driven accelerators in the medical field, specially by their use in cancer therapy with hadrons. Given the relatively young field of study and the respective lack of literature on the topic, this work included, as a first step, a systematic investigation of the expected secondary neutron fields close to the laser-driven ion source LION by using the Geant4 Monte Carlo simulation toolkit. This was done by employing, as primary proton source terms, realistic and published primary proton spectra representative of present and future commissioning steps of the LION experiment.

As second step, based on the results of the Geant4 simulations, the feasibility of applying different available neutron detectors (such as conventional active and passive REM counters, the LUPIN-II, and a gold foil-based Bonner Spheres Spectrometer) was studied, for several irradiation scenarios. Surprisingly, although the most distinctive feature of the secondary neutron fields expected at laser-driven facilities is the pulsed time structure (as a result of the pulsed nature of the primary ion source), the Geant4 Monte Carlo simulations underlined that for low-intensity primary sources (as represented in this study by the Zeil2010 proton spectrum) the neutron dose per bunch is not an issue even for conventional neutron REM counters, devices routinely employed in most of radiation protection departments where neutron doses are of interest. Measurements in this condition could then, in principle, be performed by using conventional devices, but are compromised by the usually low repetition frequency of the primary source. As shown, about a thousand bunches are at least required when using Zeil2010-like spectra, to produce a total neutron dose measurable with statistical confidence by conventional REM counters (about a hundred of nSv). At the current status of most of laser-driven ion sources, similar to the LION facility, this is currently hardly achievable, considering that on average the number of proton bunches per measurement day is around hundred. In addition, due to the current lack of bunch-to-bunch stability a measurement over a large number of bunches could only give an indicative estimate of the total produced neutron dose and, consequently, not much information on the dose produced by a single bunch. The present feasibility study also showed that, by increasing the intensity of the source term (i.e., by using Ma2019 and Wagner2016 proton spectra), the pulsed nature of the field becomes the major issue and, as a result, that conventional neutron radiation protection devices are no longer suitable.

In conclusion, the feasibility study clearly showed that performing measurements at LION during the time of this work with the selected detectors was not feasible. Nevertheless, it guided the decision of employing the LUPIN-II and the Passive LINUS as measurement devices for experiments at a different facility, the DRACO laser-driven ion source, as described in Chapter 6.

The experimental results derived from the measurement campaign at DRACO produced the most relevant conclusion of this thesis: they confirmed that the LUPIN-II is an excellent candidate for online single-bunch measurements of the secondary neutron dose inside the experimental hall that hosted the laser-driven ion source for primary protons with cutoff energies up to about 60 MeV (maximum cutoff energy reached during the measurement campaign previously described), providing trustable results independently from the presence of pulsed photons. Maximum neutron doses per bunch at about two meters from the laser-target were of the order of about 300 nSv/bunch. This experimental campaign also showed that integrated measurements of the neutron dose over a few hundred laser-shots can be successfully performed with CR39-based REM counters, such as the Passive LINUS used within this study.

In addition, the relatively good agreement between the experimental results derived at DRACO and the dedicated Monte Carlo simulations performed as part of this thesis for the DRACO facility, in terms of secondary neutron dose per bunch, demonstrate that the approximations used in the source term definition (in terms of energy spectrum, number of protons per bunch, and divergence) and in the geometries modeled were adequate, at least for order-of-magnitude calculations of the secondary neutron dose. Similar approximations could be then used to run simulations with proton spectra with higher cutoff energies than the ones used in this study, to derive reasonable estimates of the secondary neutron dose per bunch expected at even higher intensities. However, it must be pointed out that to derive more accurate simulation results, the described approximations must be overcome, especially in the source term definition. For example, all the various source components should be included in the geometry definition, such as backward-emitted protons, forward- and backward emitted electrons and specular-reflected electrons. Furthermore, a more detailed geometry of the components hosted inside the vacuum chamber is needed, because their role as neutron sources or neutron shields should not be neglected anymore when trying to get more realistic results.

Through this study, the question whether the secondary neutron fields are a relevant issue for the future employment of laser-driven ion sources in the medical field, although crucial, cannot be answered, simply because clinical-like conditions such as a tumor

treatment plan, would be needed to answer such a question with experimental data. Instead, the results of the present study are important because they provide a first experimental proof that suitable tools to measure secondary neutron dose on a single-bunch basis without being affected by the other components of the radiation field, are nowadays available.

Following this last conclusion, the natural and attractive next step would be the organization of a measurement campaign, whose goal is to measure the secondary neutron dose produced during a radiobiological experiment, as the one described by *Brack et al.* [13] where a mouse tumor model was successfully irradiated by using laser-driven protons, by using one or more LUPIN-II units, as single-bunch neutron dose monitors. Such experimental activity would bring us a step further towards answering the question on the actual magnitude of the secondary neutron radiation in a clinical application of laser-driven ion accelerators.

Additionally, because a large fraction of primary particles is lost on the elements hosted in the vacuum chamber (and is consequently impossible to be directly measured), a possible field of further research following this work is to investigate the relation between single-bunch neutron dose and total number of protons per bunch, in order to develop a non-invasive complementary tool based on neutron detection (more specifically neutron *dose*) that could help estimating the total number of protons per bunch produced on the single-bunch level, similarly, for instance, to what was suggested in [84].

Further studies could also involve laser-driven *electron* accelerators. As already mentioned in the introduction, research on laser-driven particle acceleration is, of course, not restricted to only proton or ion acceleration, but instead a whole distinct branch of research teams and facilities are focused on improving laser-driven *electron* acceleration and its related applications, as the ETTF (Electron and Thomson Test Facility) experimental station hosted at CALA, Garching near Munich, Germany. Pulsed secondary radiation is expected at such acceleration facilities as well, with similar difficulties in the detection of neutrons as described in this thesis for laser-driven *ion* sources. First test measurements performed at the ETTF facility gave already promising results suggesting that the LUPIN-II could probably also find useful application in the determination of the single-bunch secondary neutron dose produced at laser-driven electron sources.

9. Bibliography

1. Macchi, A. A Review of Laser-Plasma Ion Acceleration. *arXiv:1712.06443 [physics.plasm-ph]* 1–24 (2017).
2. Bolton, P. R., Parodi, K and Schreiber, J. *Applications of Laser-Driven Particle Acceleration*. (CRC Press, 2018). doi:10.1201/9780429445101.
3. Sakaki, H. *et al. Designing integrated laser-driven ion accelerator systems for hadron therapy at PMRC (Photo Medical Research Center)*. (2009).
4. Schippers, J. M., Lomax, A., Garonna, A. & Parodi, K. Can Technological Improvements Reduce the Cost of Proton Radiation Therapy? *Semin. Radiat. Oncol.* **28**, 150–159 (2018).
5. Peeters, A. *et al.* How costly is particle therapy? Cost analysis of external beam radiotherapy with carbon-ions, protons and photons. *Radiother. Oncol.* **95**, 45–53 (2010).
6. Daido, H., Nishiuchi, M. & Pirozhkov, A. S. Review of laser-driven ion sources and their applications. *Reports Prog. Phys.* **75**, (2012).
7. Wagner, F. *et al.* Maximum Proton Energy above 85 MeV from the Relativistic Interaction of Laser Pulses with Micrometer Thick CH2 Targets. *Phys. Rev. Lett.* **116**, (2016).
8. Linz, U. & Alonso, J. What will it take for laser driven proton accelerators to be applied to tumor therapy? *Phys. Rev. Spec. Top. - Accel. Beams* **10**, 1–8 (2007).
9. Zeil, K. *et al.* Dose-controlled irradiation of cancer cells with laser-accelerated proton pulses. *Appl. Phys. B Lasers Opt.* **110**, 437–444 (2013).
10. Yogo, A. *et al.* Measurement of relative biological effectiveness of protons in human cancer cells using a laser-driven quasimonoenergetic proton beamline. *Appl. Phys. Lett.* **98**, 053701 (2011).
11. Doria, D. *et al.* Biological effectiveness on live cells of laser driven protons at dose rates exceeding 109 Gy/s. *AIP Adv.* **2**, (2012).
12. Rösch, T. F. *et al.* A feasibility study of zebrafish embryo irradiation with laser-accelerated protons. *Rev. Sci. Instrum.* **91**, (2020).
13. Brack, F. E. *et al.* Spectral and spatial shaping of laser-driven proton beams using a pulsed high-field magnet beamline. *Sci. Rep.* **10**, 1–12 (2020).
14. Chaudhary, P. *et al.* Radiobiology Experiments With Ultra-high Dose Rate Laser-Driven Protons: Methodology and State-of-the-Art. *Front. Phys.* **9**, 1–12 (2021).
15. International Commission on Radiological Protection. *Relative Biological Effectiveness (RBE), QualityFactor (Q), and Radiation Weighting Factor (wR)*. *Annals of the ICRP* (2003).
16. Stolarczyk, L. *et al.* Dose distribution of secondary radiation in a water phantom for a proton pencil beam—EURADOS WG9 intercomparison exercise. *Phys. Med. Biol.* **63**, 085017 (2018).
17. Farah, J. *et al.* Measurement of stray radiation within a scanning proton therapy facility: EURADOS WG9 intercomparison exercise of active dosimetry systems. *Med. Phys.* **42**, 2572–2584 (2015).
18. Trinkl, S. *et al.* Systematic out-of-field secondary neutron spectrometry and dosimetry in pencil beam scanning proton therapy. *Med. Phys.* **44**, 1912–1920

(2017).

19. Howell, R. M. & Burgett, E. A. Secondary neutron spectrum from 250-MeV passively scattered proton therapy: Measurement with an extended-range Bonner sphere system. *Med. Phys.* **41**, 092104 (2014).

20. Wochnik, A. *et al.* Out-of-field doses for scanning proton radiotherapy of shallowly located paediatric tumours—a comparison of range shifter and 3D printed compensator. *Phys. Med. Biol.* **66**, (2021).

21. Zorloni, G. *et al.* Joint EURADOS WG9-WG11 rem-counter intercomparison in a Mevion S250i proton therapy facility with Hyperscan pulsed synchrocyclotron. *Phys. Med. Biol.* **67**, 075005 (2022).

22. McClung, F. J. & Hellwarth, R. W. Giant Optical Pulsations from Ruby. *J. Appl. Phys.* **33**, 828–829 (1962).

23. Di Domenico, M. Small-Signal Analysis of Internal (Coupling-Type) Modulation of Lasers. *J. Appl. Phys.* **35**, (1964).

24. Strickland, D. & Mourou, G. Compression of amplified chirped optical pulses. *Opt. Commun.* **56**, 219–221 (1985).

25. Wilks, S. C. *et al.* Energetic proton generation in ultra-intense laser-solid interactions. *Phys. Plasmas* **8**, 542–549 (2001).

26. Allen, M. *et al.* Proton spectra from ultraintense laser-plasma interaction with thin foils: Experiments, theory, and simulation. *Phys. Plasmas* **10**, 3283–3289 (2003).

27. Borghesi, M. *et al.* Laser-driven proton beams: Acceleration mechanism, beam optimization, and radiographic applications. *IEEE Trans. Plasma Sci.* **36**, 1833–1842 (2008).

28. Higginson, A. *et al.* Near-100 MeV protons via a laser-driven transparency-enhanced hybrid acceleration scheme. *Nat. Commun.* **9**, (2018).

29. Centre for Advanced Laser Application (CALA). Application of laser-driven particle acceleration. https://www.alpa.physik.uni-muenchen.de/protons.html. (2021).

30. Borghesi, M. Laser-driven ion acceleration: State of the art and emerging mechanisms. *Nucl. Instruments Methods Phys. Res. Sect. A Accel. Spectrometers, Detect. Assoc. Equip.* **740**, 6–9 (2014).

31. Esirkepov, T., Borghesi, M., Bulanov, S. V., Mourou, G. & Tajima, T. Highly Efficient Relativistic-Ion Generation in the Laser-Piston Regime. *Phys. Rev. Lett.* **92**, 175003 (2004).

32. Bulanov, S. S. *et al.* Radiation pressure acceleration: The factors limiting maximum attainable ion energy. *Phys. Plasmas* **23**, 1–17 (2016).

33. Lundh, O., Ranebo, Y. & Svendsen, K. *Dosimetry in environments surrounding a laser-plasma accelerator, Report number: 2019:04*. (2019).

34. Sakaki, H. *et al.* Calculation of radiation shielding for laser-driven hadron beams therapeutic instrument. in *IPAC 2010 - 1st International Particle Accelerator Conference* 94–96 (2010).

35. Olšovcová, V. *et al.* Radiation protection aspects in the vicinity of TW class laser systems. *Prog. Nucl. Sci. Technol.* **4**, 173–177 (2014).

36. Olšovcová, V., Haley, R., MacFarlene, L., Rus, B. & Griffiths, M. Bulk shielding for laser research centre ELI Beamlines. *Prog. Nucl. Sci. Technol.* **4**, 247–251 (2014).

37. Florescu, M. G. *et al.* Radiological safety assessment for the experimental area of

a hyper-intense laser with peak-power of 1pw-cetal. *Radiat. Prot. Dosimetry* **175**, 104–109 (2017).

38. Fan, J. *et al.* Shielding design for a laser-accelerated proton therapy system. *Phys. Med. Biol.* **52**, 3913–3930 (2007).

39. Faby, S. & Wilkens, J. J. Assessment of secondary radiation and radiation protection in laser-driven proton therapy. *Z. Med. Phys.* **25**, 112–122 (2015).

40. Borne, F., Delacroix, D., Gele, J. M., Masse, D. & Amiranoff, F. Radiation protection for an ultra-high intensity laser. *Radiat. Prot. Dosimetry* **102**, 61–70 (2002).

41. Liang, T. *et al.* Radiation dose measurements for high-intensity laser interactions with solid targets at SLAC. *Radiat. Prot. Dosimetry* **172**, 346–355 (2016).

42. Alvarez, J. *et al.* Laser Driven Neutron Sources: Characteristics, Applications and Prospects. *Phys. Procedia* **60**, 29–38 (2014).

43. Lan, Z. & Yogo, A. Exploring nuclear photonics with a laser driven neutron source. *Plasma Phys. Control. Fusion* **64**, 024001 (2022).

44. Zulick, C. *et al.* Energetic neutron beams generated from femtosecond laser plasma interactions. *Appl. Phys. Lett.* **102**, (2013).

45. Lancaster, K. L. *et al.* Characterization of 7Li(p, n) 7Be neutron yields from laser produced ion beams for fast neutron radiography. *Phys. Plasmas* **11**, 3404–3408 (2004).

46. Yang, J. M. *et al.* Neutron production by fast protons from ultraintense laser-plasma interactions. *J. Appl. Phys.* **96**, 6912–6918 (2004).

47. Roth, M. *et al.* Bright Laser-Driven Neutron Source Based on the Relativistic Transparency of Solids. *Phys. Rev. Lett.* **110**, 044802 (2013).

48. Yogo, A. *et al.* Single shot radiography by a bright source of laser-driven thermal neutrons and x-rays. *Appl. Phys. Express* **14**, (2021).

49. Knoll, G. F. *Radiation Detection and Measurement*. vol. 69 (2010).

50. Eijk, C. W. E. Van. Inorganic scintillators for thermal neutron detection. **38**, 337–342 (2004).

51. Justus, A. L. Count rate limitations for pulse-counting instrumentation in pulsed accelerator fields. *Health Phys.* **102**, 8–24 (2012).

52. Andersson, I. Ö. & Braun, J. A neutron rem counter. (1964).

53. Birattari, C., Ferrari, A., Nuccetelli, C., Pelliccioni, M. & Silari, M. An extended range neutron rem counter. *Nucl. Instruments Methods Phys. Res. Sect. A Accel. Spectrometers, Detect. Assoc. Equip.* **297**, 250–257 (1990).

54. H.H. Hsu, K.R. Alvar, and D. G. V. A new Bonner-sphere set for high energy neutron measurements: monte carlo simulation. *IEEE Trans. Nucl. Sci.* **41**, 938–940 (1994).

55. Klett, A., Mayer, S., Theis, C. & Vincke, H. A neutron dose rate monitor for high energies. *Radiat. Meas.* **41**, 3–6 (2006).

56. Birattari, C. *et al.* The Extended Range Neutron REM Counter 'LINUS': Overview and Latest Developments. **76**, 135–148 (1998).

57. Mares, V., Sannikov, A. V. & Schraube, H. Response functions of the Andersson-Braun and extended range rem counters for neutron energies from thermal to 10

GeV. *Nucl. Instruments Methods Phys. Res. Sect. A Accel. Spectrometers, Detect. Assoc. Equip.* **476**, 341–346 (2002).

58. Caresana, M. *et al.* Intercomparison of radiation protection instrumentation in a pulsed neutron field. *Nucl. Instruments Methods Phys. Res. Sect. A Accel. Spectrometers, Detect. Assoc. Equip.* **737**, 203–213 (2014).

59. Caresana, M., Ferrarini, M., Manessi, G. P., Silari, M. & Varoli, V. LUPIN, a new instrument for pulsed neutron fields. *Nucl. Instruments Methods Phys. Res. Sect. A Accel. Spectrometers, Detect. Assoc. Equip.* **712**, 15–26 (2013).

60. Caresana, M. *et al.* A new version of the LUPIN detector: Improvements and latest experimental verification. *Rev. Sci. Instrum.* **85**, (2014).

61. Tisi, M. Initial measurements and studies for the commissioning of an on-line dose monitoring system installed in the new Free Electron Laser facility SwissFEL. (Politecnico di Milano, 2017).

62. Cassou, R. M. & Benton, E. V. Properties and applications of CR-39 polymeric nuclear track detector. *Nucl. Track Detect.* **2**, 173–179 (1978).

63. Fantuzzi, E. *et al.* Inter-comparison among fast neutron dosimetric services using PADC material of different composition. *Radiat. Meas.* **36**, 487–492 (2003).

64. Caresana, M., Ferrarini, M., Parravicini, A. & Sashala Naik, A. Calibration of a passive rem counter with monoenergetic neutrons. *Radiat. Meas.* **71**, 498–501 (2014).

65. Bramblett, R. L., Ewing, R. I. & Bonner, T. W. A new type of neutron spectrometer. *Nucl. Instruments Methods* **9**, 1–12 (1960).

66. Hertel, N. E. & Davidson, J. W. The response of bonner spheres to neutrons from thermal energies to 17.3 MeV. *Nucl. Instruments Methods Phys. Res. Sect. A Accel. Spectrometers, Detect. Assoc. Equip.* **238**, 509–516 (1985).

67. Mares, V., Schraube, G. & Schraube, H. Calculated neutron response of a Bonner sphere spectrometer with 3He counter. *Nucl. Instruments Methods Phys. Res. Sect. A Accel. Spectrometers, Detect. Assoc. Equip.* **307**, 398–412 (1991).

68. Wiegel, B. & Alevra, A. V. NEMUS-The PTB Neutron Multisphere Spectrometer: Bonner spheres and more. *Nucl. Instruments Methods Phys. Res. A* **476**, 36–41 (2002).

69. Routti, J. T. & Sandberg, J. V. General purpose unfolding program LOUHI78 with linear and nonlinear regularizations. *Comput. Phys. Commun.* **21**, 119–144 (1980).

70. Reginatto, M., Goldhagen, P. & Neumann, S. Spectrum unfolding, sensitivity analysis and propagation of uncertainties with the maximum entropy deconvolution code MAXED. *Nucl. Instruments Methods Phys. Res. Sect. A Accel. Spectrometers, Detect. Assoc. Equip.* **476**, 242–246 (2002).

71. Braga, C. C. & Dias, M. S. Application of Neural Networks for unfolding neutron spectra measured by means of Bonner Spheres. *Nucl. Instruments Methods Phys. Res. Sect. A Accel. Spectrometers, Detect. Assoc. Equip.* **476**, 252–255 (2002).

72. McElroy, W. N., Berg, S. & Crockett, T. *A computer-automated iterative method for neutron flux spectra determination by foil activation.* (1967).

73. Simmer, G., Mares, V., Weitzenegger, E. & Rühm, W. Iterative unfolding for Bonner sphere spectrometers using the MSANDB code - Sensitivity analysis and

dose calculation. *Radiat. Meas.* **45**, 1–9 (2010).

74. Garny, S. Development of a Biophysical Treatment Planning System for the FRM II Neutron Therapy Beamline. (TUM, 2009).

75. Agostinelli, S. *et al.* Geant4—a simulation toolkit. *Nucl. Instruments Methods Phys. Res. Sect. A Accel. Spectrometers, Detect. Assoc. Equip.* **506**, 250–303 (2003).

76. Allison, J. *et al.* Recent developments in Geant4. *Nucl. Instruments Methods Phys. Res. Sect. A Accel. Spectrometers, Detect. Assoc. Equip.* **835**, 186–225 (2016).

77. Geant4 A Simulation Toolkit, Use Cases - reference physics lists. https://geant4.web.cern.ch/node/302 (2021).

78. The International Commission on Radiological Protection (ICRP). ICRP Publication 74. Conversion Coefficients for use in Radiological Protection against External Radiation. *Ann. ICRP 26 (3-4).* (1996).

79. Pelliccioni, M. Overview of fluence-to-effective dose and fluence-to-ambient dose equivalent conversion coefficients for high energy radiation calculated using the fluka code. *Radiat. Prot. Dosimetry* **88**, 279–297 (2000).

80. Mares, V. *et al.* A comprehensive spectrometry study of a stray neutron radiation field in scanning proton therapy. *Phys. Med. Biol.* **61**, 4127–4140 (2016).

81. Rösch, T. F. *et al.* Laser-driven ION (LION) acceleration at the centre for advanced laser applications (CALA). in *2017 Conference on Lasers and Electro-Optics Europe & European Quantum Electronics Conference (CLEO/Europe-EQEC)* 1–1 (IEEE, 2017). doi:10.1109/CLEOE-EQEC.2017.8087795.

82. ELSE Nuclear. Rem counter per neutroni in campi pulsati LUPIN BF3-NP. (2019).

83. Centre for Advanced Laser Application (CALA). Experimental stations. https://www.cala-laser.de/en/instruments/experiments.html (2021).

84. Tisi, M., Mares, V., Schreiber, J., Englbrecht, F. S. & Rühm, W. Geant4 Monte Carlo simulation study of the secondary radiation fields at the laser-driven ion source LION. *Sci. Rep.* **11**, 24418 (2021).

85. Englbrecht, F. S. *et al.* Radiation protection modelling for 2.5 Petawatt-laser production of ultrashort X-ray, proton and ion bunches: Monte Carlo model of the Munich CALA facility. *J. Radiol. Prot.* **40**, 1048–1073 (2020).

86. Zeil, K. *et al.* The scaling of proton energies in ultrashort pulse laser plasma acceleration. *New J. Phys.* **12**, (2010).

87. Ma, W. J. *et al.* Laser Acceleration of Highly Energetic Carbon Ions Using a Double-Layer Target Composed of Slightly Underdense Plasma and Ultrathin Foil. *Phys. Rev. Lett.* **122**, 1–6 (2019).

88. Application of laser-driven particle acceleration. https://www.alpa.physik.uni-muenchen.de/protons.html (2021).

89. Gitomer, S. J. *et al.* Fast ions and hot electrons in the laser–plasma interaction. *Phys. Fluids* **29**, 2679 (1986).

90. Nürnberg, F. *et al.* Radiochromic film imaging spectroscopy of laser-accelerated proton beams. *Rev. Sci. Instrum.* **80**, (2009).

91. Private communication with J. Schreiber (2020).

92. Ter-Avetisyan, S. *et al.* Ultrashort PW laser pulse interaction with target and ion

acceleration. *Nucl. Instruments Methods Phys. Res. Sect. A Accel. Spectrometers, Detect. Assoc. Equip.* **909**, 156–159 (2018).

93. Ferrarini, M. Caratterizzazione di un Rem Counter e di un sistema di sfere di Bonner a sensibilità estesa basato sull'utilizzo di rivelatori di CR39 per il monitoraggio ambientale di acceleratori per uso medicale. (Politecnico di Milano, 2007).

94. Vittoria, F. A., Penzo, S., Leopizzi, G., Borsari, M. & Mariotti, F. New statistical model of track overlap in solid state nuclear track detectors. *Radiat. Meas.* **148**, 106664 (2021).

95. Schramm, U. *et al.* First results with the novel petawatt laser acceleration facility in Dresden. *J. Phys. Conf. Ser.* **874**, 48–52 (2017).

96. ELSE Nuclear. Unità di monitoraggio di radiazioni gamma con camera a ionizzazione. (2019).

97. Brack, F. E. PhD Thesis, Unpublished. (TU Dresden, 2022).

98. Ziegler, T. *et al.* Proton beam quality enhancement by spectral phase control of a PW-class laser system. *Sci. Rep.* **11**, 1–7 (2021).

99. Kroll, F. *et al.* Tumor irradiation in mice with a laser-accelerated proton beam. *Under Rev. Nat. Phys.* 13–16.

100. Tisi, M., Mares, V., Schreiber, J., Englbrecht, F. S. & Rühm, W. Geant4 Monte Carlo simulation study of the secondary radiation fields at the laser-driven ion source LION. *Sci. Rep.* **VOL**, PAGES (2022).

101. Anderson, I. S. *et al.* Research opportunities with compact accelerator-driven neutron sources. *Phys. Rep.* **654**, 1–58 (2016).

102. International Commission on Radiological Protection (ICRP). *1990 Recommendations of the International Commission on Radiological Protection*. *ICRP Publication 60* (Pergamon Press, 1990).

103. The International Commission on Radiation Units and Measurements (ICRU). Determination of Operational Dose Equivalent Quantities for Neutrons, ICRU Report 66. (2001).

104. Snavely, R. A. *et al.* Intense High-Energy Proton Beams from Petawatt-Laser Irradiation of Solids. *Phys. Rev. Lett.* **85**, 2945–2948 (2000).

105. Fuchs, J. *et al.* Laser-driven proton scaling laws and new paths towards energy increase. *Nat. Phys.* **2**, 48–54 (2006).

106. Currie, L. A. Limits for Qualitative Detection and Quantitative Determination: Application to Radiochemistry. *Anal. Chem.* **40**, 586–593 (1968).

107. Canberra Industries Inc. Genie ™ 2000 Spectroscopy Software.

108. Done, L. & Ioan, M. R. Minimum Detectable Activity in gamma spectrometry and its use in low level activity measurements. *Appl. Radiat. Isot.* **114**, 28–32 (2016).

109. Alevra, A. V. & Thomas, D. J. Neutron spectrometry in mixed fields: multisphere spectrometers. *Radiat. Prot. Dosimetry* **107**, 37–72 (2003).

110. Matzke, M. Unfolding procedures. *Radiat. Prot. Dosimetry* **107**, 155–174 (2003).

111. Fokas, E., Kraft, G., An, H. & Engenhart-Cabillic, R. Ion beam radiobiology and cancer: Time to update ourselves. *Biochim. Biophys. Acta - Rev. Cancer* **1796**, 216–229 (2009).

Appendix A: Radiation and dosimetric quantities

Radiation dosimetry mainly deals with the definition and the application of quantities to measure the dose from ionizing radiation received by objects, with special focus on the human body. Several quantities are used to properly describe the energy deposition of a given radiation field and its related biological damage; it is practical to separate them into three subgroups according to their nature:

- Physical quantities
- Protection quantities
- Operational quantities

A scheme of the most used quantities in dosimetry and of the relation that exists with each other is shown in Figure 42.

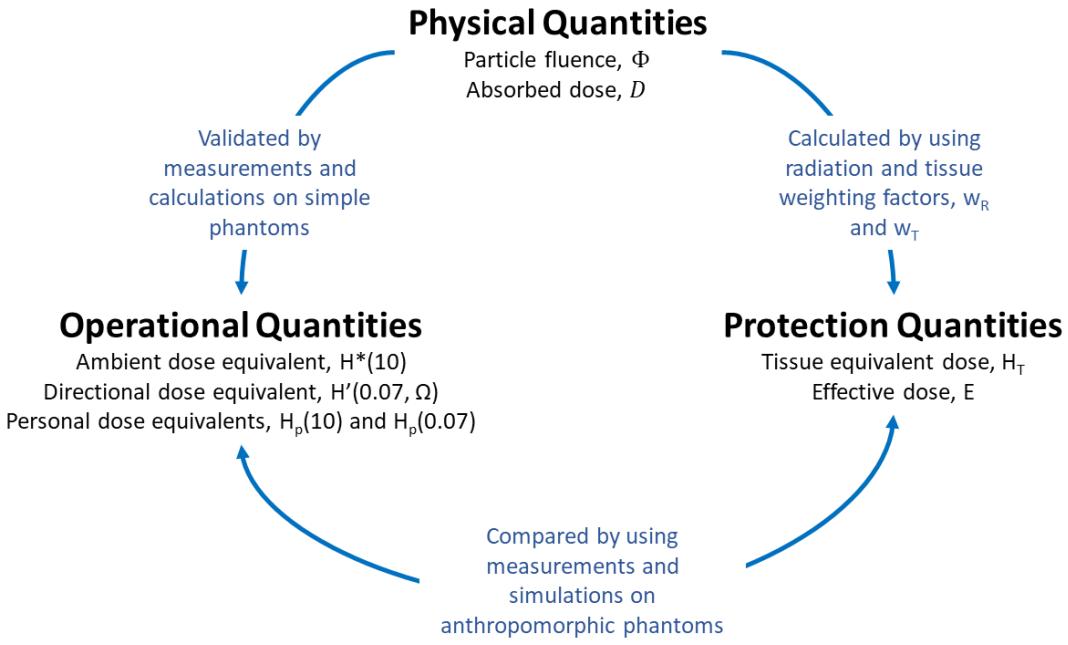

Figure 42: Most relevant quantities used in dosimetry and their respective relations.

9.1 Physical quantities

The properties of a radiation field can be described by quantities like its fluence (Φ), *absorbed* dose (D) and their derivatives. The fluence, Φ, is simply the number of particles of a radiation field crossing a given surface:

$$\Phi = \frac{\mathrm{dN}}{\mathrm{dA}} \tag{15}$$

Where dN is the number of particles crossing the unit area dA, and it is often given in terms m^{-2} or cm^{-2}.

The absorbed dose, D, is the physical quantity that describes the energy deposited by a radiation field per unit mass of the deposition site. It is defined as an average quantity over the deposition volume as follows:

$$\mathrm{D} = \frac{\mathrm{d}\bar{\varepsilon}}{\mathrm{dm}} \tag{16}$$

and it is given in units of Gy ($Gy = J/kg$). Being the deposition of energy due to radiation a stochastic process, Equation (16) cannot be intended as infinitesimal quantity.

9.2 Protection quantities

The ICRP Publication 60 [102] introduced the concept of *equivalent dose* as an average quantity over a whole organ or tissue (and not a point quantity as the *dose equivalent* described later in the Subchapter 9.3). The equivalent dose of a tissue T due to radiation R, $H_{T,R}$, is defined as the average absorbed dose of tissue T due to radiation R, $D_{T,R}$, multiplied by a radiation-depended weighting factor, w_R:

$$H_{T,R} = w_R \cdot D_{T,R} \tag{17}$$

In case of a mix of different radiation types, the total equivalent dose imparted to tissue T, H_T, is simply calculated by the sum over R in the following way:

$$H_T = \sum_R H_{T,R} = \sum_R w_R \cdot D_{T,R} \tag{18}$$

By considering that the radiosensitivity of a tissue differs from organ to organ, the concept of *effective dose*, E, was introduced and defined as the sum of the tissue dose equivalent, H_T, multiplied by a tissue weighting factor, w_T, over T:

$$E = \sum_T w_T \cdot H_T \tag{19}$$

The effective dose E is the protection quantity upon which limitations and regulations are built. However, this quantity can only be calculated and not directly measured, that is why the ICRU introduced operational quantities [103].

9.3 Operational quantities

It is known that the same absorbed dose, D, may have a different biological impact if it is delivered by a different radiation type (e.g., γ-photon, α-particle, neutron etc.) or to a different tissue. The local rate of energy deposition along the particle track or LET (Linear Energy Transfer) of a particle, strongly influences the severity of a biological damage imparted by it, when passing through a tissue. Generally, the higher the LET of a particle the higher the biological damage, although the same absorbed dose, D, is delivered. To take this effect into account, the concept of *dose equivalent*, H, was introduced as the product of the absorbed dose in a given tissue position and a quality factor, Q, that is a function of the particle LET.

$$H = Q \cdot D \tag{20}$$

To clearly mark a *qualitative* difference in the meaning of dose equivalent from that of absorbed dose, the conventionally used unit for dose equivalent is the Sievert, (Sv) instead of Gy, although the quality factor, Q, is a dimensionless quantity.

Several operational quantities were defined separately for weakly and strongly penetrating radiation types, because weakly penetrating radiations are regulated by limits on the skin dose, while strongly penetrating radiations by limits on effective dose. As an example, photons with energy ≤ 15 KeV or electrons with energy ≤ 2 MeV are to be considered as weakly penetrating radiations, while neutrons or higher energy photons are to be considered as highly penetrating.

An acceptable estimate of the effective dose is done by determining the dose equivalent in a phantom of soft tissue material[13] at a depth of 10 mm, while for an estimate of the skin dose the same quantity is calculated at a depth of 0.07 mm. One of the most widely operational quantity used in radiation protection is the *ambient* dose equivalent H*(10), whose aim is the area monitoring of strongly penetrating radiation. For weakly penetrating radiation the directional dose equivalent is used H'(007,Ω). For individual monitoring, instead, $H_p(10)$ and $H_p(0.07)$ are used, that are the *personal* dose equivalent for strongly and weakly radiations, respectively.

[13] The elemental composition of the tissue is defined by the ICRU [103]

Appendix B: MSANDB Unfolding procedure applied to the Au-BSS

In the following, the unfolding procedure followed to reconstruct the neutron spectrum from a measurement of the Au-BSS is shown [74]:

1. By using physical considerations or Monte Carlo simulations a guess spectrum, Φ^0, is produced, having the same energy binning structure as that of the Au-BSS response matrix, R_{ij}, where i runs from 1 to the maximum number of spheres of the BSS, n, while j runs from 0 to the highest bin, m. A good guess spectrum is recommended for a fast convergence of the iterative unfolding procedure [109][110].
2. Second step is the calculation of the simulated activity for each sphere i:

$$A_i^0 = \sum_j R_{ij}\Phi_j^0 \tag{21}$$

   Where Φ_j^0 is the guess fluence spectrum value for the j^{th} bin.
3. A correction factor is then derived by comparing the calculated activity of each sphere with the respective measured activity, A_i^m:

$$\ln(M) = \frac{\sum_i ln\left(\frac{A_i^m}{A_i^0}\right)\cdot\left(\frac{A_i^m}{s_i^m}\right)^2}{\sum_i\left(\frac{A_i^m}{s_i^m}\right)^2} \tag{22}$$

   Where $s_i^m$is the variance of the measured count rate for the i^{th} sphere.
4. By using the correction M, the next spectrum, Φ^1, and calculated activity vector, A^1, can be derived:

$$\Phi_j^1 = M\cdot\Phi_j^0 \quad , \quad A_i^1 = M\cdot A_i^0 \tag{23}$$

5. The actual iteration process starts now with the help of a weighting factor, W_{ij}^k, that is dependent on the iteration number k.

$$W_{ij}^k = \frac{R_{ij}\Phi_j^k}{A_i^k} \tag{24}$$

6. At each k iteration the correction parameter, M_j^k, can be then calculated for each energy bin j as follows:

$$\ln\left(M_j^k\right) = \frac{\sum_i W_{ij}^k \cdot ln\left(\frac{A_i^m}{A_i^k}\right) \cdot \left(\frac{A_i^m}{s_i^m}\right)^2}{\sum_i W_{ij}^k \cdot \left(\frac{A_i^m}{s_i^m}\right)^2} \quad (25)$$

7. By applying the correction function both fluence and activity for the $k+1$ iteration can be calculated:

$$\Phi_j^{k+1} = M_j^k \cdot \Phi_j^k \quad , \quad A_i^{k+1} = M_j^k \cdot A_i^k \quad (26)$$

8. The best way to stop the iteration procedure is when the relative change of the calculated activity of iteration k+1 and iteration k (for all energy bins) is smaller than a predefined value ε, according to the following equation:

$$\frac{\chi^{k+1}}{\chi^k} - 1 \leq \varepsilon \text{ where } \chi^k = \sum_i \left(ln\frac{A_i^m}{A_i^k}\right)^2 \cdot \left(\frac{A_i^m}{s_i^m}\right)^2 \quad (27)$$

Appendix C: Minimum Detectable Activity for Au-foil activation technique

A key parameter that defines the final performance of the Au-foil activation technique is the Minimum Detectable Activity (MDA) that the Ge-spectrometers available for this study can measure. The MDA will directly translate into the minimum detectable neutron fluence achievable with this technique.

GENIE2000, the software used to run IRM's Canberra Ge spectrometers, calculates the minimum detectable activity following *Lloyd A. Currie's* principles of detection limit proposed in 1968 [106][107].

Considering a 5% probability of false negative and a 5% probability of false positive results, the MDA for a counting system can be written according to the following formula [108]:

$$MDA = \frac{2.71 + 3.29\sqrt{B + B\frac{N}{2m}}}{\varepsilon T I_\gamma} \tag{28}$$

Where B is the number of counts due to the background, N is the number of channels of the peak, m is the number of channels to the left and to the right of the peak (see Figure 43), ε is the detection efficiency, T is the counting time and I_γ is the branching ratio of the reaction leading to the gamma decay.

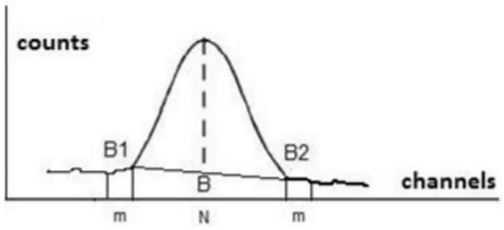

Figure 43: Representation of a peaked background with labels for the estimation of the minimum detectable activity (MDA). Figure adapted from *L. Done and M.-R. Ioan (2016)* [108].

Ge-spectrometer energy calibration

The spectrometry laboratory of the IRM owned 16 Canberra Ge-spectrometers (HP-Ge) with different features which were employed for sample analysis in the framework of

environmental studies. Given the field of application of IRM's lab, none of the spectrometers was already calibrated to measure the gold foil samples in the present project, as described at Subchapter 3.3.2.1.

It is common practice to employ a calibration sample with similar geometry as the samples to be measured (a gold foil in the present case), with a known activity, and perform a measurement with the spectrometer to be used. Given the known activity of the calibration sample, it is possible to re-calibrate the detector reading according to the real activity value.

Since the feasibility of the gold foil technique was to be evaluated in an early stage of the project, and no gold foil sample of known activity could be produced in the short term, it was necessary to perform an energy-dependent efficiency calibration of available Ge-spectrometers using point sources of known activity. For the present purpose, ^{241}Am, ^{152}Eu and ^{137}Cs sources were employed. These point sources were chosen because their gamma emission energies covered the whole spectrum of interest and allowed to derive an efficiency calibration from 40 keV to 1,200 keV.

The chosen detector was the ALM Ge spectrometer[14], whose cylindrical crystal measured 6 cm in diameter and 4.6 cm in length, positioned at the bottom of a lead-shielded cavity about 30 cm in diameter and 25 cm deep (Figure 44a).

[14] Detector model: GX3018

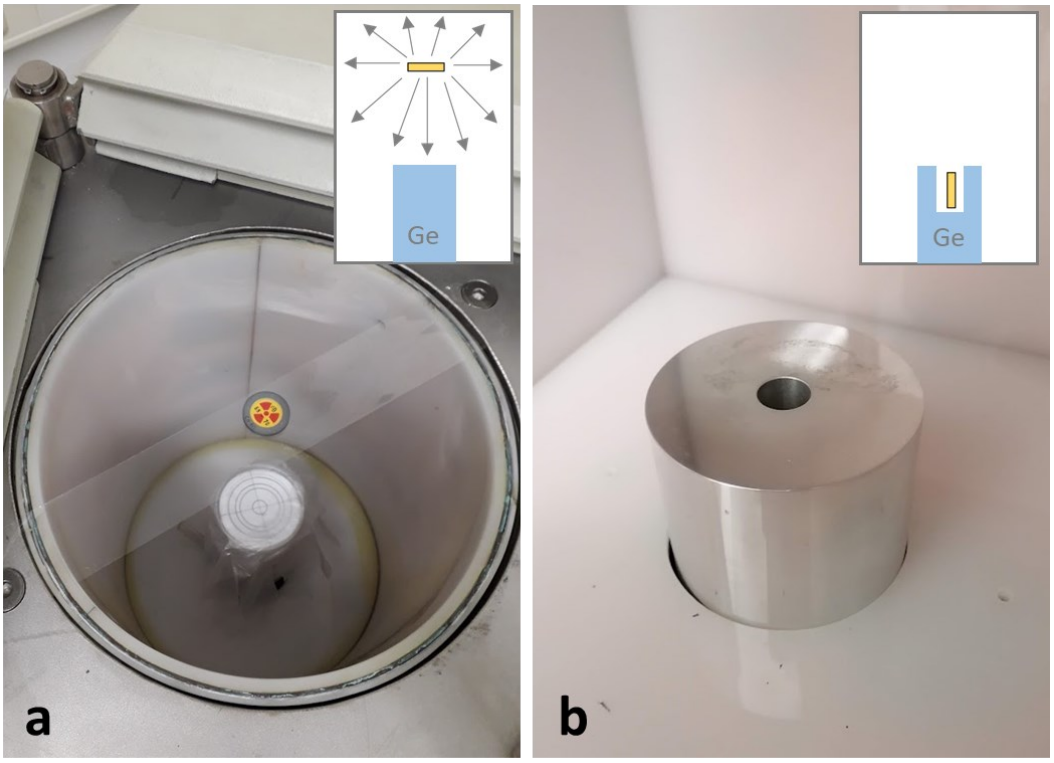

Figure 44: **a**) ALM detector during the calibration procedure with a point source, **b**) Bore hole detector used to reach higher detection efficiency.

It was decided to start with a sample-to-detector distance of 20 cm (to minimize the geometrical differences between point source and real gold foil dimensions), and then reduce this distance to 10 cm, to check the increase in efficiency given the reduced distance. The results of the calibration are summarized in Figure 45 where the efficiency of the specific configuration is plotted against the gamma photon energy. The efficiency of the detection of gold foil activity for the 20 cm geometry, ε_{20cm}, and for the 10 cm geometry, ε_{10cm}, were derived by looking at the efficiency value for an energy of 411 keV (emission energy of ^{198}Au), highlighted by the red line in Figure 45:

- $\varepsilon_{20cm} = 1.7 \cdot 10^{-3}$
- $\varepsilon_{10cm} = 5.5 \cdot 10^{-3}$

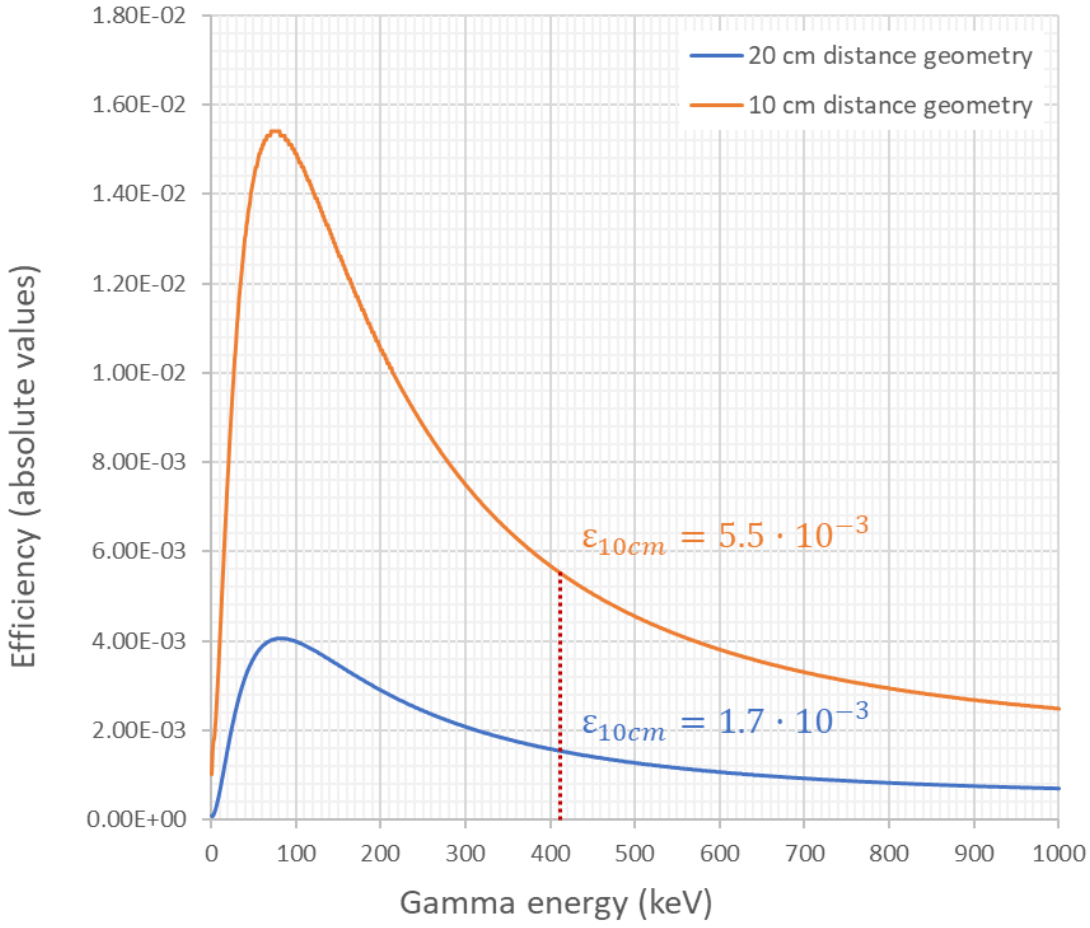

Figure 45: Efficiency calibration curve for ALM detector using 20 cm distance geometry and 10 cm distance geometry.

Neutron activation measurements were performed in the former Secondary Standard Dosimetry Laboratory (SSDL) of the HMGU, to produce activated gold foils to be analyzed with the described calibration geometries. The minimum detectable activity using the two different techniques after a 3-day long gamma spectrometry measurement resulted in:

- $MDA_{20cm} = 1.66\,Bq$
- $MDA_{10cm} = 0.46\,Bq$

To reduce the MDA further and get an estimate of the lowest measurable activity achievable at the Institute, it was decided to employ a bore hole Ge-detector[15] whose efficiency was expected to be higher due to geometrical reasons (Figure 44b). This detector used a cylindrical Ge crystal 6.3 cm in diameter and length that had a well-like shape, which

[15] Detector model: GCW3023

maximized the view angle (depth 3.5 cm, diameter 2.2 cm). It has to be mentioned that due to the small dimension of the well, it was not possible to perform a new calibration with the available point sources (which were bigger than the size of the well aperture). For this reason, an already implemented measurement geometry was employed that assumed a cylindrical emitting volume 1 cm in height. This was quite representative of the gold foil given that the gold foil could be rolled up in a cylinder-like shape and inserted into the detector aperture. The efficiency of this Ge spectrometer at 411 keV was $\varepsilon_{BH} = 0.26$. As expected, the bore-hole detector improved the minimum detectable activity of our technique for a 3-day long measurement significantly to:

- $MDA_{BH} = 5.0 \cdot 10^{-3}\ Bq$

In order to compare the three different techniques, measurements were performed in the former SSDL by positioning a gold foil sample inside the 6" Bonner sphere and irradiating it with an AmBe neutron source at the distance of 0.25 m for 3 days. The experiment was repeated three times and the gold foil activity was analyzed by using the three different detection techniques. The whole activity was benchmarked by Geant4 Monte Carlo simulations. Table 7 reports the results of the three measurements and of the simulation.

	Simulation	**Measurement** $\boldsymbol{\varepsilon_{20cm}}$	**Measurement** $\boldsymbol{\varepsilon_{10cm}}$	**Measurement** $\boldsymbol{\varepsilon_{BH}}$
Activity (Bq)	33.2	35.0 (± 2.4%)	36.0 (± 1.1%)	29.9 (± 3.1%)

Table 7: Comparison of detection geometries after 3-day exposure at 25 cm distance from an AmBe neutron source (calibration uncertainty excluded).

The experimental results acquired with the three different techniques and the result of the Geant4 Monte Carlo simulation lie within a maximum of 20% difference with each other. Although better agreement is needed for quantitative measurements, this result is considered enough as a proof that the efficiency calibrations and the respective minimum detectable activities (MDA) derived are roughly with reasonable level of precision needed to carry out a feasibility study. Therefore, the conclusion of this activity was that the lowest MDA achievable at the IRM's spectroscopy laboratory was provided by the bore hole detector ($MDA_{BH} = 5.0 \cdot 10^{-3}\ Bq$) and this value has to be taken as reasonable MDA for any further feasibility studies concerning gold foil activity measurements in the frame of this project. A refinement in the calibration of the bore hole detector will be needed if further activity measurements were to be carried out.

Appendix D: Code benchmark with FLUKA

As part of this thesis a dedicated benchmark was performed by comparing Geant4 with FLUKA Monte Carlo simulations on the Laser-driven ION facility (LION). FLUKA simulations with conservative primary beam parameters were performed in an early phase of the project, as part of the licensing of the LION facility. These simulations were recently summarized in a dedicated publication [85].

To perform the benchmark, the LION facility was modeled in Geant4 by using the same geometrical dimensions and materials as published by *Englbrecht et al.* [85]. It is therefore important to mention that the simulation geometry is totally similar to the one described in Chapter 5 apart for one detail: the 2.5 cm thick aluminum flange on the front face of the vacuum chamber was left open instead of closed. So it was simulated to exactly reproduce the geometry described by *Englbrecht et al.* in [85].

The source term used for the benchmark was a box-like proton energy spectrum[16] with energy from 10 to 75 MeV and total divergence of 180 mrad. Neutron fluence spectra were calculated in the same positions as described in Chapter 5.

Figure 46a to Figure 46h show the comparison of the neutron spectra for all scorers inside the LION cave (1 – 8). The Geant4-derived neutron spectra are reported with different colors for each scorer, while the FLUKA-derived neutron spectra are reported in gray.

[16] The probability to have a proton in an energy bin is constant over the entire energy range.

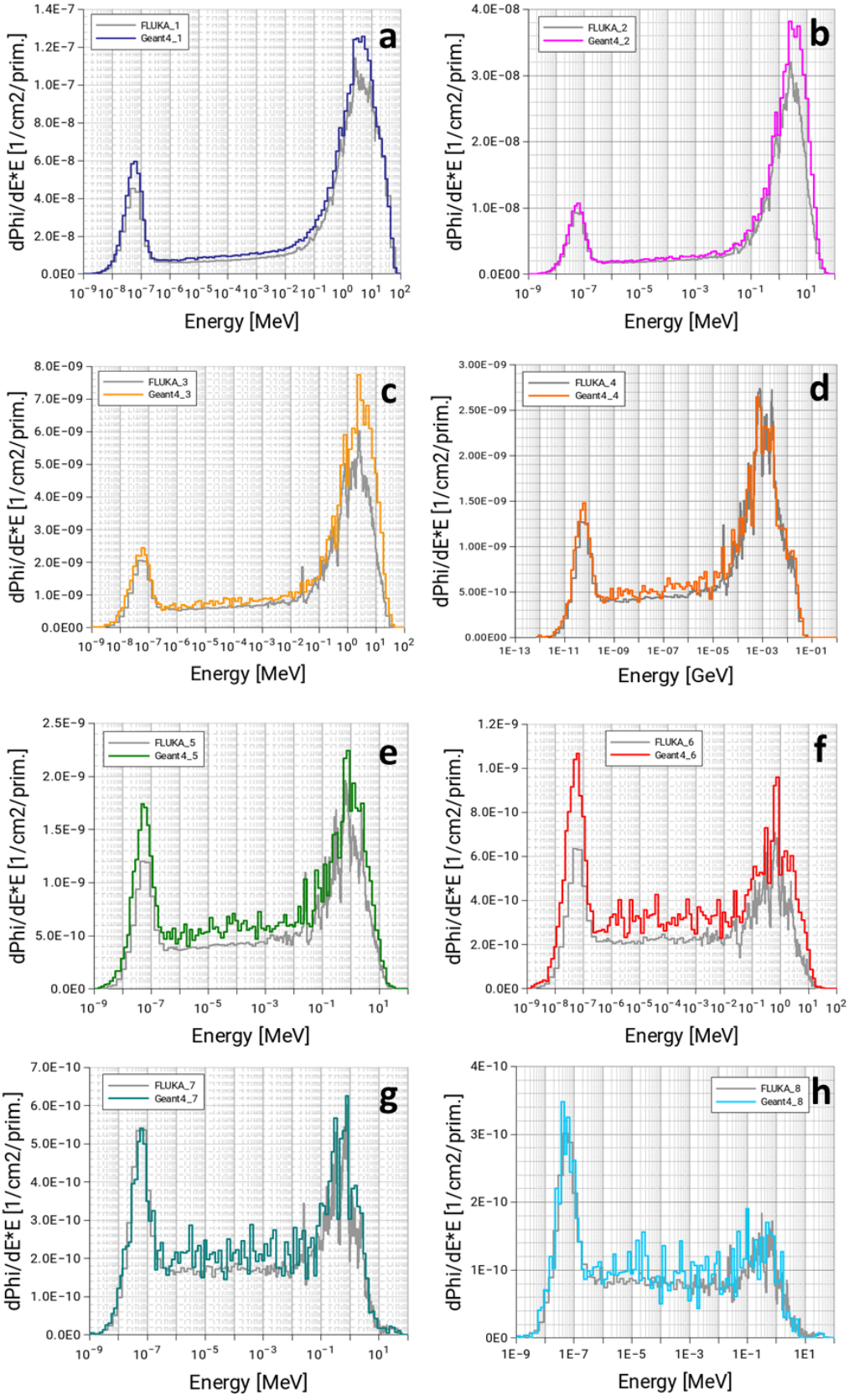
a
FLUKA_1
Geant4_1
dPhi/dE*E [1/cm2/prim.]
Energy [MeV]
b
FLUKA_2
Geant4_2
dPhi/dE*E [1/cm2/prim.]
Energy [MeV]
c
FLUKA_3
Geant4_3
dPhi/dE*E [1/cm2/prim.]
Energy [MeV]
d
FLUKA_4
Geant4_4
dPhi/dE*E [1/cm2/prim.]
Energy [GeV]
e
FLUKA_5
Geant4_5
dPhi/dE*E [1/cm2/prim.]
Energy [MeV]
f
FLUKA_6
Geant4_6
dPhi/dE*E [1/cm2/prim.]
Energy [MeV]
g
FLUKA_7
Geant4_7
dPhi/dE*E [1/cm2/prim.]
Energy [MeV]
h
FLUKA_8
Geant4_8
dPhi/dE*E [1/cm2/prim.]
Energy [MeV]

Figure 46: Subfigures from **a** to **h** report the comparison between FLUKA and Geant4 neutron fluence spectra, for all scorers from 1 to 8 (see Figure 16). FLUKA spectra are in gray while Geant4 ones are colored.

Table 8 shows the total neutron fluence for each scorer, for both FLUKA and Geant4. The average relative difference of the total neutron fluence was 21%, this allowed to conclude that the two simulation environments show a reasonable agreement.

	Neutron Fluence [$cm^{-2}protons^{-1}$]		
Scorer ID	**Geant4**	**FLUKA**	**Relative difference**
Scorer1	7.18×10^{-7}	6.05×10^{-7}	16%
Scorer2	1.79×10^{-7}	1.42×10^{-7}	21%
Scorer3	4.09×10^{-8}	3.11×10^{-8}	24%
Scorer4	1.93×10^{-8}	1.75×10^{-8}	9%
Scorer5	1.79×10^{-8}	1.34×10^{-8}	25%
Scorer6	8.93×10^{-9}	5.98×10^{-9}	33%
Scorer7	5.38×10^{-9}	4.67×10^{-9}	13%
Scorer8	2.33×10^{-9}	2.04×10^{-9}	12%
Average			19%

Table 8: Summary of the total fluences for all 8 scorers (see Figure 16) close to the vacuum LION chamber calculated by Geant4 and FLUKA.

Appendix E: Derivation of number of protons per bunch

In the present thesis, the derivation of the photon and neutron dose per bunch was simply done by multiplying the respective dose per primary by the total number of primaries per bunch, N. Given the usual lack of information regarding the total number of primary protons per bunch produced at laser-driven proton facilities, this calculation needed some preliminary considerations.

The usual quantitative information made available from measurements is the number of protons per unit energy and unit solid angle $dN/(dEd\Omega)$, typically measured over rather narrow angles. The total divergence is often not measured. Therefore, without other considerations, it is difficult to even guess the total number of protons produced in each single shot. To help calculating doses per bunch, a guidance to derive rough estimations on the total number of protons produced per bunch is provided here starting from energetic considerations.

The total kinetic energy carried by a single bunch of protons, E_{kin}, is only a fraction of the energy carried by the laser pulse, E_L, which means in short that $E_{kin} = \eta E_L$ where η is the energy conversion efficiency coefficient (by definition $0 \leq \eta \leq 1$).

From exemplary measurements performed on large laser systems (E_L greater than several tens of J, up to $100\,\mathrm{J}$), it could be estimated that the maximum conversion efficiency is of the order 0.1 [104]. This is in accordance to what was stated by *Wagner et al.* reporting an energy transfer efficiency of 7% for protons with energy greater than 4 MeV [7]. For smaller systems ($E_L \approx 10\,\mathrm{J}$), the efficiency was found to be in the order of 0.01 [105], while for even smaller systems ($E_L \approx 1\,\mathrm{J}$) the efficiency drops to 10^{-3} (both considering protons with energy from 4 MeV to E_{cutoff}) [105].

Considering the fact that in the present study spectra from 1 MeV are used, energy transfer efficiencies will be adapted to take into account that also particles with energies lower than 4 MeV are emitted. The second column of Table 9 reports the energy transfer efficiencies used for *Zeil2010*, *Ma2019* and *Wanger2016* spectra.

As an approximation, it is assumed here that the energy distribution does not depend on the angle. Then, E_{kin} can be expressed as in equation (29), where the average divergence angle Ω is multiplied outside of the integral sign and where the subscript i stands for Zeil2010, Ma2019, or Wagner2016:

$$E_{kin,i} = \eta_i E_L = \Omega_i \cdot \int_{E_0}^{E_{cutoff}} \frac{dN}{dEd\Omega} EdE \tag{29}$$

This equation can be re-written as in equation (30) in order to derive an estimation of maximum and minimum solid angle Ω:

$$\Omega_i = \frac{\eta_i E_L}{\int_{E_0}^{E_{cutoff}} \frac{dN}{dEd\Omega} EdE} \tag{30}$$

The total number of emitted particles is therefore:

$$N_i = \Omega_i \cdot \int_{E_0}^{E_{cutoff}} \frac{dN}{dEd\Omega} dE \tag{31}$$

Where the solid angle Ω is found applying equation (30). Table 9 summarizes energy transfer efficiency, η, kinetic energy of the proton bunch, E_{kin}, and number of protons per bunch, N, for each primary source term used.

Spectrum	$\boldsymbol{\eta}$	$\boldsymbol{E_{kin}}$ [J]	N [$\mathbf{p}^+$/bunch]
Zeil2010 ($\boldsymbol{E_L}$ = 3 J)	0.27%	0.008	1.98×10^{10}
Ma2019 ($\boldsymbol{E_L}$ = 9.2 J)	1.8%	0.16	9.10×10^{10}
Wagner2016 ($\boldsymbol{E_L}$ = 200 J)	7%	15.7	1.08×10^{13}

Table 9: Estimated total number of protons (and electrons) considering the respective energy conversion according to each laser system.

The total number of particles calculated above can be used to derive estimates on the total neutron fluence and dose per bunch, as it is done in Chapter 5. It needs to be underlined that the approximations used to derive these values include high uncertainties, and, therefore, these values should only be used to derive indicative estimates.

Acknowledgements

First, I would like to thank my supervisor, Prof. Dr. Werner Rühm, for accepting me as his PhD student more than three years ago. I mostly thank him for having the time to discuss my problems and help me shape my project the way I wanted, yet keeping me on track and not losing the focus on the goals we planned to achieve. My gratitude also goes to my co-supervisor, Vladimir Mares, for being always available for technical questions and for what I could learn from his experience on the field. A special thank goes to Prof. Marco Caresana and Prof. Jörg Schreiber whose suggestions have been crucial, and greatly improved the final quality of the final work. I ought to thank in addition Prof. Katia Parodi and Prof. Christian Thieke for guiding the Graduate School GRK2274 which I had the pleasure to be part of during my experience as PhD student. My gratitude goes also to Dr. Eike Hohmann, who, although not directly involved in this project, provided essential technical support and experimental collaboration.

I would like to also thank my office mate Thomas for his help with the setup of Geant4 and his help in understanding the code details, but mostly for sharing the pain that Geant4 Monte Carlo programming causes to those who deliberately decide deal with it! Thanks to Nancy and Ferran for creating a nice environment in the office and in the lab too!

Thanks to Alessia and Emilio, two great friends met along the way. Alessia, thanks for opening the way through the PhD submission process, I would have never made it through if I had to do it on my own! And, Emilio, thank you for your availability and precious help with the Faraday cage, I simply provided the box, you did the rest! (Plus, it has been real fun!). A special thank goes also to Noemi and Klemens for being part of this journey as good and precious friends!

Thanks to Kerstin and Reiner for your help with the calibration of the Ge-spectrometers and for the help you gave me exchanging my gold-foil samples in the initial months of my PhD. Thanks to Matteo for your detailed analysis of the CR-39 and the information you gave me on this detector, it was indeed a crucial step of this work.

In addition, I'd like to thank all people who I met during my stay at Helmholtz, Thomas, Monika, Maria, Nina, Tomek, and Florian.

To conclude, I want to thank my wife for always being there for me (wherever we may go), for helping me to find the good aspects during the difficult times of this PhD and for pushing me to celebrate the good results (as you know, celebrating is not my strong suit!).

Affidavit

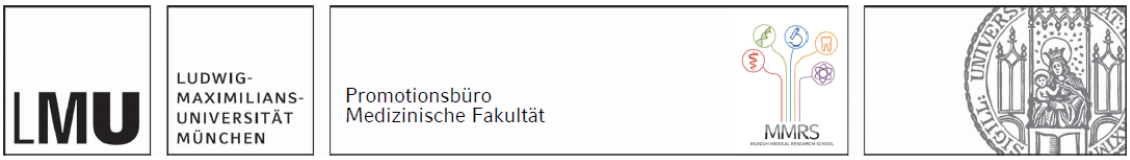

Eidesstattliche Versicherung

Tisi, Marco

Name, Vorname

Ich erkläre hiermit an Eides statt, dass ich die vorliegende Dissertation mit dem Titel:

Secondary neutrons at laser-driven ion sources

selbständig verfasst, mich außer der angegebenen keiner weiteren Hilfsmittel bedient und alle Erkenntnisse, die aus dem Schrifttum ganz oder annähernd übernommen sind, als solche kenntlich gemacht und nach ihrer Herkunft unter Bezeichnung der Fundstelle einzeln nachgewiesen habe.

Ich erkläre des Weiteren, dass die hier vorgelegte Dissertation nicht in gleicher oder in ähnlicher Form bei einer anderen Stelle zur Erlangung eines akademischen Grades eingereicht wurde.

München, 22/03/2022
Ort, Datum

Marco Tisi
Unterschrift Doktorandin bzw. Doktorand

List of Publications

M. Tisi, V. Mares, J. Schreiber, F. S. Englbrecht and W. Rühm. *Geant4 Monte Carlo simulation study of the secondary radiation fields at the laser-driven ion source LION. Sci. Rep.* **11** (2021) 24418.

A. Wochnik, L. Stolarczyk, I Ambrožovà, M. Davídkovà, M De Saint-Hubert, S. Domanski, C. Domingo, Ž. Kneževic, R. Kopec, M. Ku, M. Majer, N. Mojzeszek, V. Mares, I. Martínez-Rovira, M. A. Caballero-Pacheco, E. Pizza, J. Swakon, S. Trinkl, M. Tisi, R. Harrison and P. Olko. *Out-of-field doses for scanning proton radiotherapy of shallowly located paediatric tumours—a comparison of range shifter and 3D printed compensator. Phys. Med. Biol.* **66** (2021) 035012.

G. Zorloni, G. Bosmans, T. Brall, M. Caresana, M. De Saint-Hubert, C. Domingo, C. Ferrante, F. Ferrulli, R. Kopec, J. Leidner, V. Mares, R. Nabha, P. Olko, M. A. Caballero Pacheco, W. Rühm, M. Silari, L. Stolarczyk, J. Swakon, M. Tisi, S. Trinkl, O. Van Hoey, G. Vilches-Freixas. *Joint EURADOS WG9-WG11 rem-counter intercomparison in a Mevion S250i proton therapy facility with Hyperscan pulsed synchrocyclotron. Phys. Med. Biol.* **7** (2022) 075005.